

# Microfluidic Reactors for the Synthesis of Nanocrystals

by

**Brian K. H. Yen**

B. S. Chemistry  
University of North Carolina at Chapel Hill, 1999

Submitted to the Department of Chemistry  
in Partial Fulfillment of the Requirements for the Degree of

**DOCTOR OF PHILOSOPHY**

at the  
MASSACHUSETTS INSTITUTE OF TECHNOLOGY  
February 2007

© 2007 Massachusetts Institute of Technology  
All Rights Reserved

Signature of Author \_\_\_\_\_

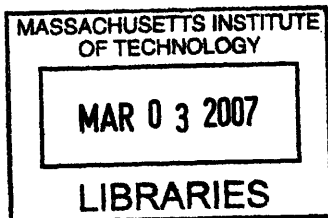
Department of Chemistry  
September 18, 2006

Certified by \_\_\_\_\_

Moungi Bawendi  
Professor of Chemistry  
Thesis Supervisor

Accepted by \_\_\_\_\_

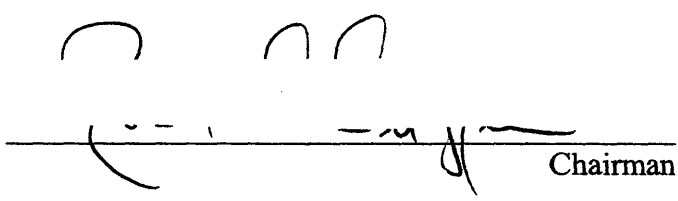
Robert W. Field  
Chairman, Department Committee on Graduate Students



ARCHIVES

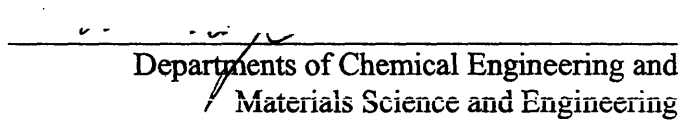


This doctoral thesis has been examined by a committee of the Department of Chemistry as follows:

Professor Robert G. Griffin  Chairman

Professor Mounji G. Bawendi  Thesis Supervisor

Professor Sylvia T. Ceyer  Department of Chemistry

Professor Klavs F. Jensen  Departments of Chemical Engineering and Materials Science and Engineering



# **Microfluidic Reactors for the Synthesis of Nanocrystals**

by

Brian K. H. Yen

Submitted to the Department of Chemistry on September 18, 2006 in partial fulfillment of the requirements for the degree of Doctor of Philosophy in Chemistry

## **ABSTRACT**

Several microfluidic reactors were designed and applied to the synthesis of colloidal semiconductor nanocrystals (NCs). Initially, a simple single-phase capillary reactor was used for the synthesis of CdSe NCs. Precursors were delivered into a section of the capillary maintained at high temperature where they decomposed and reacted to form NCs. Monodisperse, bright CdSe NC samples were prepared over a significant range of average sizes. The excellent stability and reproducibility of the continuous flow system was also demonstrated. However, a limitation of the single-phase flow approach was that slow mixing and large residence time distributions can be detrimental to the overall quality (eg. size distribution) of the NC samples produced. These limitations were overcome by designing and fabricating in silicon a gas-liquid segmented flow microreactor. In contrast to the single-phase flow, recirculation within the liquid segments provides a mechanism to exchange fluid elements located near the channel walls with those in the center. This recirculation has the dual effect of reducing axial dispersion and greatly improving the mixing efficiency – factors which have a strong influence on the ultimate size and size distribution of NCs produced. Compared to single-phase operation, preparation of CdSe NCs in segmented flow resulted in superior reactor throughput and narrower size distributions. Finally, the segmented flow method was extended in a microreactor designed for the synthesis of more complicated NC architectures. The design incorporated multiple inlet channels, which allowed for continuous injection of multiple precursor streams. This reactor was used to synthesize several core/shell NC structures – CdSe/ZnS, CdSe/ZnSe, and CdSe/Cd<sub>x</sub>Zn<sub>1-x</sub>Se.

Thesis Supervisor: Mounji G. Bawendi

Title: Professor of Chemistry



*For My Father*





# Table of Contents

Title page .....	1
Signature Page .....	3
Abstract .....	5
Dedication .....	7
Table of Contents .....	9
List of Figures .....	12

## Chapter 1: Introduction and Motivation

1.1 Quantum Confinement .....	15
1.2 Classical Nucleation and Growth .....	20
1.3 Synthesis of Colloidal Nanocrystals by Batch Methods .....	26
1.4 Continuous Flow Microfluidic Reactors .....	28
1.5 Thesis Overview .....	30
1.6 References .....	31

## Chapter 2: A Single-Phase Liquid Capillary Reactor for Nanocrystal Synthesis

2.1 Introduction .....	35
2.2 Experimental .....	36
2.2.1 Capillary Reactor Setup .....	36
2.2.2 Synthetic Methods and Optical Characterization .....	38
2.3 Results and Discussion .....	39
2.4 Conclusions .....	50
2.5 References .....	51

## Chapter 3: Analysis of Heat and Mass Transfer Effects

3.1 Heat Transfer .....	53
3.1.1 The Graetz-Nusselt Problem .....	53
3.1.2 Results for Capillary Reactor .....	58
3.2 Mass Transfer .....	60
3.2.1 Mixing Effects .....	60
3.2.2 Residence Time Distribution (RTD) Effects .....	62
3.2.3 Influence of RTD on Size Distribution .....	69
3.3 Single and Two Phase Flow .....	71
3.4 References .....	71

## Chapter 4: Design, Fabrication, and Packaging of a Gas-Liquid Segmented Flow Microreactor

4.1 Introduction to Segmented Flow .....	73
4.2 Reactor Design Considerations .....	81
4.3 Incorporating the Design Criteria .....	85
4.4 Wafer Fabrication .....	88
4.4.1 Process Summary .....	88
4.4.2 Detailed Process Flow .....	89

4.5 Packaging and Sealing.....	94
4.6 References .....	101

**Chapter 5: Application of the Segmented Flow Microreactor to the Preparation of CdSe Nanocrystals**

5.1 Introduction .....	103
5.2 Experimental Details .....	104
5.2.1 Segmented Flow Reactor Setup .....	104
5.2.2 Segment Measurement Method.....	106
5.2.3 Synthetic and Characterization Methods.....	106
5.3 Results .....	107
5.3.1 Reactor Performance .....	107
5.3.2 Segmentation Analysis .....	109
5.3.3 Results for CdSe NCs.....	112
5.3.4 Comparison with Single-Phase Flow .....	114
5.4 Conclusions .....	118
5.5 References .....	120

**Chapter 6: Extending the Gas-Liquid Segmented Flow Approach: Continuous Injection of Multiple Precursor Streams**

6.1 Introduction .....	121
6.2 Reactor Design .....	128
6.2.1 Analysis of Flow Uniformity in Feeder Channels.....	128
6.2.2 Reactor Characteristics.....	134
6.2.3 Design Validation: Measuring the Flow Distribution .....	136
6.3 Application of the Design.....	142
6.3.1 Synthesis of Core/Shell Nanocrystals .....	142
6.3.2 Experimental Details .....	142
6.3.3 Results .....	144
6.3.4 Comments on Segmentation Quality.....	153
6.4 Conclusions .....	153
6.5 References .....	154

**Chapter 7: Summary and Future Opportunities**

7.1 Summary .....	157
7.2 Microfluidic Synthesis of Nanocrystals Under High Pressure.....	157
7.3 Synthesis of New Materials and Mechanistic Studies.....	163
7.4 Multi-Stage Operation .....	164
7.5 References .....	165

**Appendix A: Deep Reactive Ion Etching Parameters**

A.1 Introduction.....	167
A.2 Formation of Silicon Grass .....	168
A.3 Removal of Photoresist.....	170
A.4 References.....	172

<b>Appendix B: Other Reactor Designs</b> .....	175
Curriculum Vitae .....	177
Acknowledgments.....	181

## List of Figures and Tables

Figure 1.1:	Cartoon of a nanocrystal .....	16
Figure 1.2:	Schematic depiction of quantum confinement.....	16
Figure 1.3:	Absorbance and PL spectra of 4.0 nm diameter CdSe NCs .....	18
Figure 1.4:	Absorbance spectra of a size series of CdSe NCs.....	18
Figure 1.5:	Sizing curve for CdSe NCs .....	19
Figure 1.6:	Monomer concentration during crystallization/precipitation.....	21
Figure 1.7:	Monomer concentration profile near the surface of a single NC.....	23
Figure 1.8:	Monomer concentration profile accounting for the Gibbs-Thomson effect .....	23
Figure 1.9:	Dependence of the growth rate of a single NC on particle radius .....	24
Figure 1.10:	Comparison of batch and continuous flow microfluidic methods .....	29
Figure 2.1:	Experimental setup for the capillary reactor system.....	37
Figure 2.2:	Stability of the capillary reactor over 8 hours of continuous operation.....	40
Figure 2.3:	Results summary for NCs prepared using a 1:1 Se:Cd precursor composition .....	41
Figure 2.4:	Spectra obtained at constant temperature or constant flow rate .....	43
Figure 2.5:	Dependence of the number of nuclei on the concentration of TOPSe.....	44
Figure 2.6:	Size series of CdSe NCs prepared in the capillary reactor .....	46
Figure 3.1:	Coordinate system and boundary conditions used for heat transfer analysis .....	54
Table 3.1:	Eigenvalues and constants for Graetz problem.....	57
Table 3.2:	Eigenfunctions for Graetz problem.....	57
Figure 3.2:	Temperature profile within the heated section of the capillary .....	59
Figure 3.3:	Temperature of fluid in the tube center as a function of time.....	59
Figure 3.4:	Schematic illustrating the source of the RTD in a cylindrical channel.....	63
Figure 3.5:	<i>E</i> -curves for open-open boundary conditions .....	66
Figure 3.6:	Regime diagram for RTD models.....	68
Figure 3.7:	Method of estimating the RTD contribution to the overall size distribution.....	70
Figure 4.1:	Strategies for improving mixing in single-phase flow in microchannels .....	74
Figure 4.2:	Liquid velocity vectors and streamlines in gas-liquid segmented flow .....	76
Figure 4.3:	Fluorescence images of segmented flow mixing in a silicon microchannel.....	76
Figure 4.4:	Comparison of efficiencies of various mixing strategies.....	78
Figure 4.5:	Measured <i>E</i> -curves for single-phase and gas-liquid segmented flow.....	80
Figure 4.6:	Schematic showing effect of mixing and axial dispersion on size distribution.....	80
Figure 4.7:	Calculated temperature profile for silicon-glass slab.....	83
Figure 4.8:	Calculated stress field in for region separating the two temperature zones.....	84
Figure 4.9:	Gas-liquid segmented flow microreactor design .....	87
Figure 4.10:	Wafer process flow .....	90-91
Figure 4.11:	Photograph of wafer and 3D drawing of reactor .....	93
Figure 4.12:	Glass brazing process for making fluidic seals.....	96
Figure 4.13:	Photo of drilled Pyrex piece anodically bonded to a silicon reactor.....	96
Figure 4.14:	Thermal expansion curves used to estimate stress in glass-metal seal .....	98
Table 4.1:	Thermal expansion coefficients of joint materials.....	99
Figure 4.15:	Photographs of brazed fluidic connections .....	100
Figure 5.1:	Photos of segmented flow reactor and experimental setup.....	105
Figure 5.2:	Images of reactor during synthesis of CdSe NCs .....	108

Figure 5.3:	Liquid volume fraction for various flow conditions at 260°C .....	110
Figure 5.4:	Liquid slug lengths at various flow conditions .....	111
Figure 5.5:	NC spectra obtained by varying the precursor feed ratio .....	113
Figure 5.6:	Experimental setup used to compare single-phase and segmented flow .....	116
Figure 5.7:	Comparison of NCs prepared in single and two phase flow.....	117
Figure 6.1:	Monomer concentration profile for the formation of three types of NCs.....	122
Figure 6.2:	Effect of BEHP ligand during synthesis of CdSe NCs .....	124
Figure 6.3:	Diagram of addition of a second stream into a gas-liquid segmented flow.....	127
Figure 6.4:	Channel network used in the flow distribution calculation .....	129
Figure 6.5:	Calculated flow distributions for various geometries and feed rates.....	133
Table 6.1:	Side channel pressure drops.....	134
Figure 6.6:	Microreactor with two feeder channels manifolds for adding precursors .....	135
Figure 6.7:	Fluorescence image acquired during flow distribution measurement .....	137
Figure 6.8:	Sequence of image analysis steps used to determine the flow distribution .....	138
Figure 6.9:	Comparison of measured flow with ideally uniform flow case.....	140
Figure 6.10:	Flow results for a device with insufficient pressure-drop features.....	141
Figure 6.11:	Reactor during synthesis of CdSe/ZnS core/shell NCs.....	145
Figure 6.12:	Absorbance and PL spectra of cores and CdSe/ZnS core/shell NCs .....	146
Figure 6.13:	Photograph of reactor during synthesis of CdSe/ZnSe NCs.....	148
Figure 6.14:	PL spectra resulting from increasing amounts of Cd in the side stream.....	149
Figure 6.15:	Spectra of CdSe NC cores and various core/shell NCs .....	150
Figure 6.16:	Size distributions based on TEM images of NC samples in figure 6.15 .....	152
Figure 7.1:	Variation of vapor pressure with temperature for a selection of solvents .....	160
Figure 7.2:	Experimental setup for high pressure synthesis.....	161
Figure 7.3:	Results for high-pressure synthesis of CdSe NCs in toluene.....	162
Figure A.1:	Scanning electron micrograph of silicon grass .....	169
Figure A.2:	Etching of photoresist and oxide during DRIE.....	171
Figure A.3:	Cross-talk between channels resulting from oxide damage.....	171



# Chapter 1

## Introduction and Motivation

### 1.1 Quantum Confinement

Colloidal semiconductor nanocrystals (NCs) or quantum dots are a class of materials with unique chemical and electronic properties. A quantum dot is a small particle composed of a semiconductor core ( $\varphi = 1\text{-}10\text{ nm}$ ) surrounded by a layer of organic ligands (figure 1.1). Colloidal NCs can be synthesized in gram scales and are isolable, dispersible in common solvents, and readily manipulated using wet chemical techniques. A distinction should be made between colloidal quantum dots and epitaxially grown quantum dots.<sup>1</sup> The latter, also referred to as “self-assembled” quantum dots, consist of islands of semiconductor grown on a substrate and will not be discussed in this thesis. Colloidal semiconductor NCs have attracted a great deal of research interest because their optical properties can be controlled by varying the particle size during synthesis. The strong size dependence of the optical response of NCs is explained by the quantum confinement phenomenon shown in figure 1.2. As the size of a semiconductor crystal is reduced below the material’s bulk Bohr exciton radius, the electronic structure evolves from a set of bands of continuum states to a set of discrete atomic-like states. Practically speaking, strong quantum confinement is observed for many semiconductor NCs with average diameters ranging from  $\sim 1$  to 10 nm.

The optical absorbance and fluorescence spectra of a typical CdSe NC sample is shown

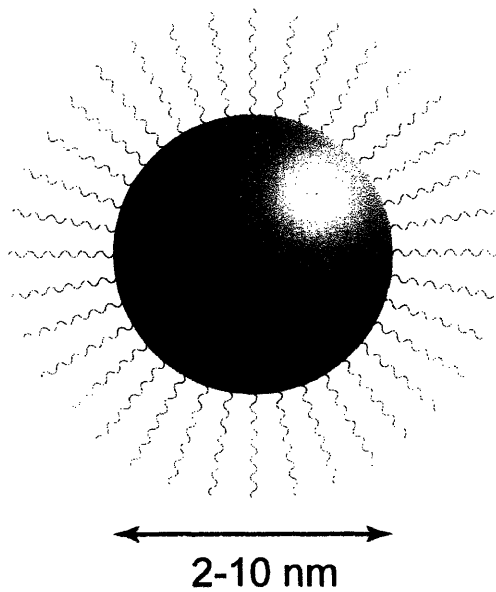


**Figure 1.1:** Cartoon of a nanocrystal showing the semiconductor core and layer of passivating organic ligands.

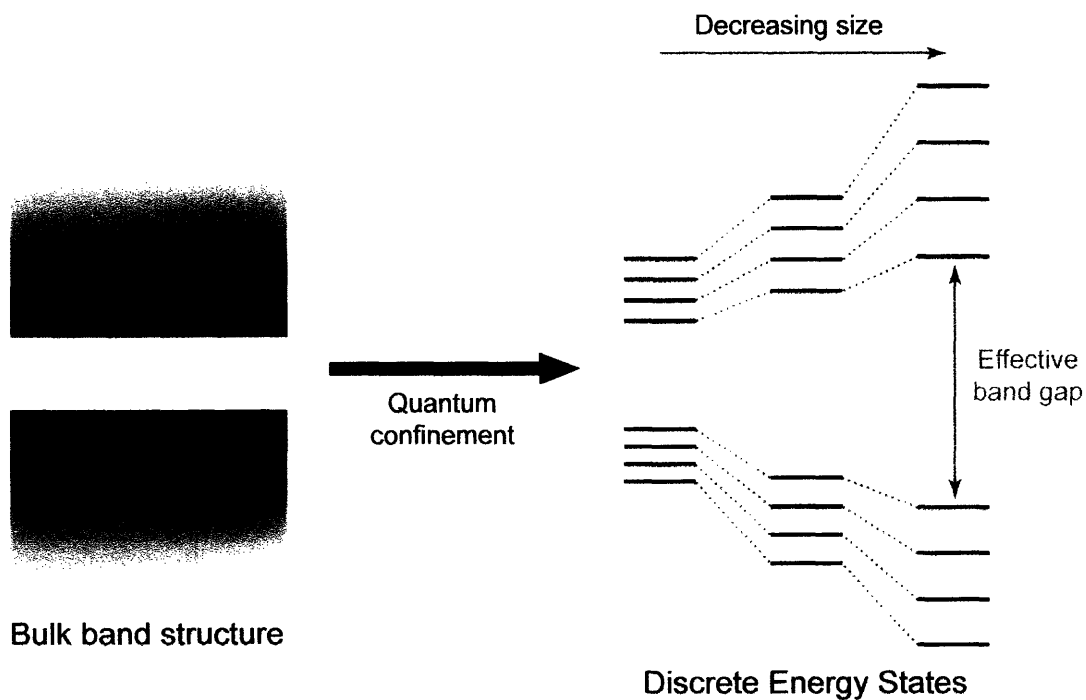


**Figure 1.2:** Schematic depiction of quantum confinement. As the size of a semiconductor is reduced below the bulk Bohr radius, the electronic structure evolves from a set of bands to discrete states. The splitting between the states continues to increase as the size decreases.



in figure 1.3. Unlike the absorbance spectrum of bulk CdSe, which is broad and featureless, several distinct optical transitions are present in the NC sample. Moreover, the fluorescence spectrum is very narrow (linewidth < 30nm for a monodisperse sample). The electronic fine structure and details of the optical splitting have been studied extensively<sup>2-6</sup> (especially for CdSe) and will not be discussed here. Qualitatively, the splitting between the discrete states is very sensitive to the size so the optical properties of these materials can be tuned by controlling the average NC diameter during synthesis. Figure 1.4 shows absorbance spectra for a size series of CdSe NCs, and figure 1.5 plots the corresponding sizing curve for CdSe. The narrow emission spectra (not shown) also evolves across the entire spectral range with varying NC size. The figures demonstrate that for CdSe, the color can be tuned over virtually the entire visible spectrum by controlling the NC diameter. Another attractive feature of semiconductor NCs is that the absorbance cross section continues to increase to the blue of the first absorbance feature (effective bandgap). Thus, unlike typical organic fluorophores, multiple emission colors can be excited with a single wavelength, and each emitted color is very saturated (narrow). It is not surprising that semiconductor NCs have been extensively studied for use in a variety of optical applications including biological fluorescent labels,<sup>7-10</sup> electroluminescent devices,<sup>11-16</sup> and lasers.<sup>17-21</sup>

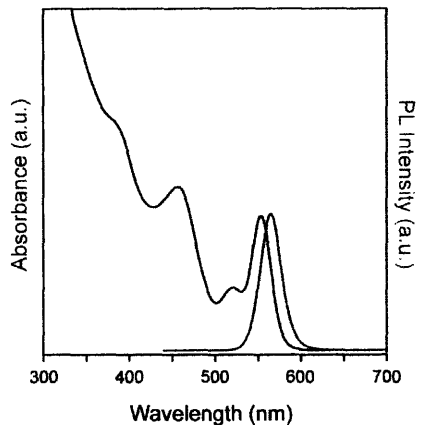


**Figure 1.3:** Absorbance (blue) and photoluminescence (red) spectra in hexanes of CdSe NCs with an average diameter of 4.0 nm.

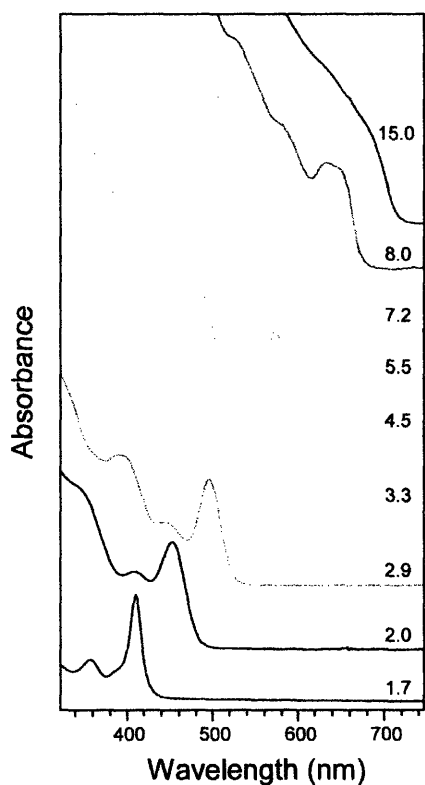


**Figure 1.4:** Absorbance spectra of a size series of CdSe NCs demonstrating the tunability over the entire visible spectrum. Corresponding average NC diameter (in nm) is shown for each spectrum. Adapted from Murray, C. B. Ph.D. Thesis, Massachusetts Institute of Technology, Cambridge, MA, 1995.

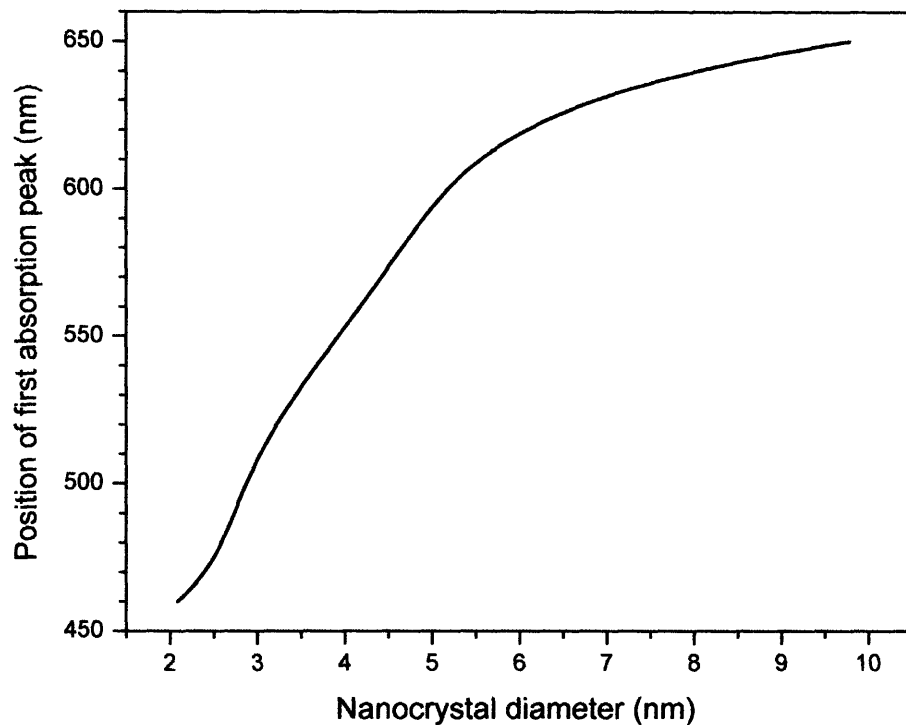


**Figure 1.5:** Sizing curve for CdSe NCs showing the relationship between the position of the band-edge absorption and average NC diameter. The curve is an empirical fit to data obtained from transmission electron microscopy and small-angle X-ray scattering. Adapted from Kuno, M. K. Ph.D. Thesis, Massachusetts Institute of Technology, Cambridge, MA 1998.

## 1.2 Classical Nucleation and Growth

For any application using semiconductor NCs, it is essential to begin with high quality samples. The production of highly crystalline and monodisperse samples of the desired size requires an understanding of the details of the NCs nucleation and growth process. Classical nucleation and growth models provide a starting point for understanding these mechanisms, and these models can qualitatively predict many of the trends observed during the synthesis of colloidal NCs. Though more details will be given in the next section, NCs are generally prepared by thermal decomposition of precursors in a mixture of solvents and coordinating ligands. As shown schematically in figure 1.6, the formation of NCs proceeds in three stages. In the first stage, the precursors quickly decompose to form reactive monomers. The monomer concentration increases until a critical supersaturation is reached at which point nuclei begin to form. The nucleation burst partially relieves the supersaturation, so that the concentration falls below the critical level. The solution is still supersaturated so that slower NC growth continues upon existing nuclei. It is important to realize that in reality, growth competes to some extent while nuclei are forming, which generally increases the polydispersity of the final sample. Therefore, a general criterion for producing low polydispersity NCs is to prepare them under conditions in which the nucleation period is much shorter than the overall growth time.

The details of nucleation and growth determine the final size and size distribution of a NC sample. Classically, the rate of homogeneous nucleation (number per unit time per unit volume) is given by an Arrhenius expression:<sup>22,23</sup>

$$J = A \exp \left[ - \frac{16\pi\gamma^3 V_m}{3k_B^3 T^3 (\ln S)^2} \right] \quad \text{Eq. 1.1}$$

where  $\gamma$  is the surface energy,  $V_m$  is the molecular volume, and  $S$  is the supersaturation ratio. The

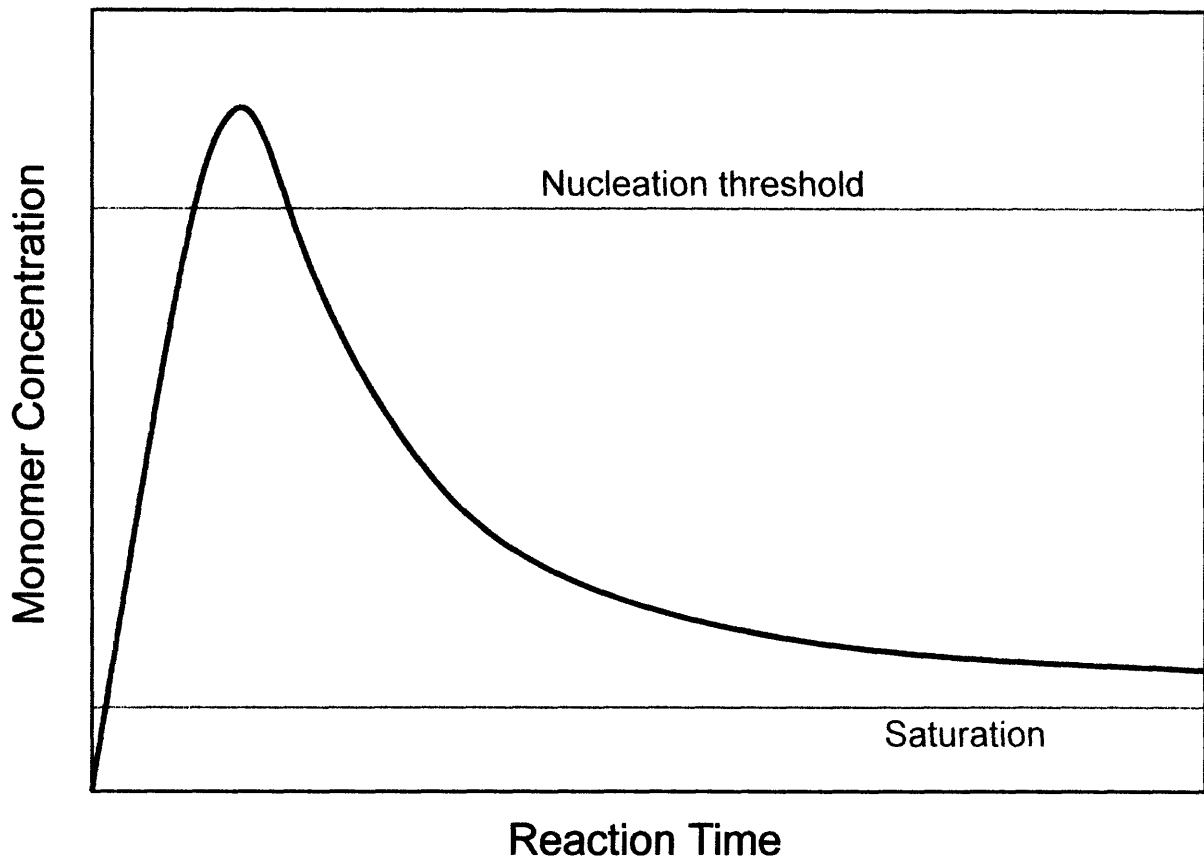


**Figure 1.6:** The monomer concentration during crystallization/precipitation. Adapted from reference 24.

latter is the ratio of the monomer concentration in solution to the equilibrium solubility concentration. This expression often fails to quantitatively predict the nucleation rate in even the simplest precipitations. However, the expression does imply that the nucleation rate depends very strongly on the supersaturation ratio  $S$ , and this appears to be the case in many systems. For instance, the LaMer model<sup>24</sup> shown in figure 1.6 assumes that the dependence is so strong that there is effectively a threshold  $S$  below which the nucleation rate is zero.

The growth on existing nuclei occurs by monomers in solution 1) diffusing from bulk solution through some diffusion layer (of thickness  $\delta$ ) to the NC surface and then 2) reacting to incorporate into the crystal lattice. Figure 1.7 is a general schematic of the monomer concentration profile near the surface of a growing NC. The concentration gradient between the bulk solution and the region near the NC surface drives the flux of monomers which ultimately incorporate into the crystal.

It is instructive to consider two limiting cases, diffusion-controlled and kinetic-controlled growth. In the former, the surface reaction is so fast that the monomer concentration near the surface is able to maintain the equilibrium solubility value  $C_{eq}$ . For small particles, the equilibrium solubility is a function of the particle radius  $R$  according to the Gibbs-Thomson equation:<sup>23</sup>

$$C_{eq} = C_{\infty} \exp\left(\frac{2\gamma V_m}{k_B TR}\right) \quad \text{Eq. 1.2}$$

where  $C_{\infty}$  is the solubility concentration for a flat surface. Figure 1.8 shows the monomer concentration profile near the surface for various NC radii. The figure shows that even though the solution may be supersaturated with respect to the *bulk* material, the dissolution of smaller

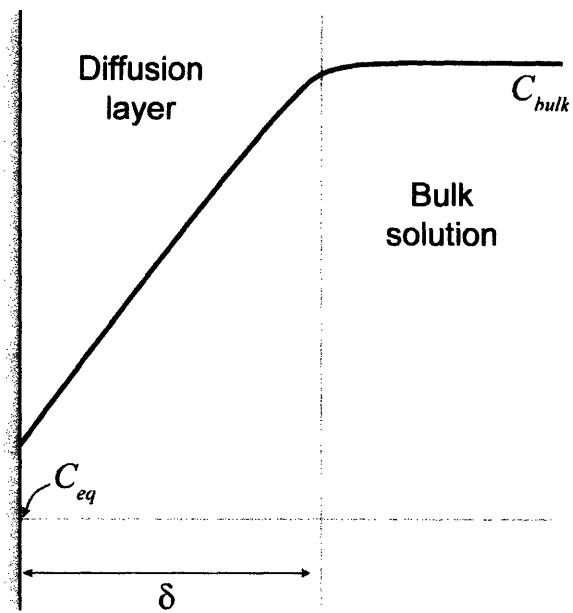


**Figure 1.7:** Generic diagram of the monomer concentration profile near the surface of a single nanocrystal.

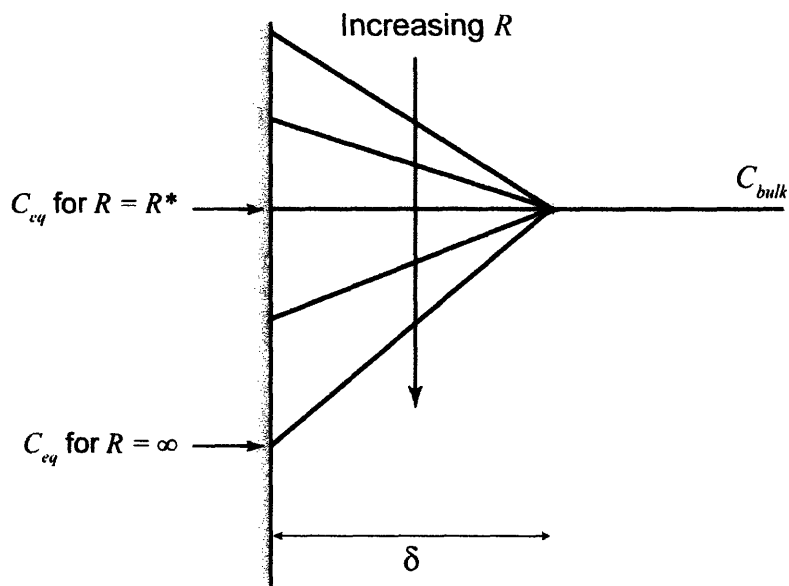


**Figure 1.8:** Monomer concentration profile near the NC surface taking into account the Gibbs-Thomson effect. Small NCs can dissolve even if the solution concentration is supersaturated with respect to the bulk material.

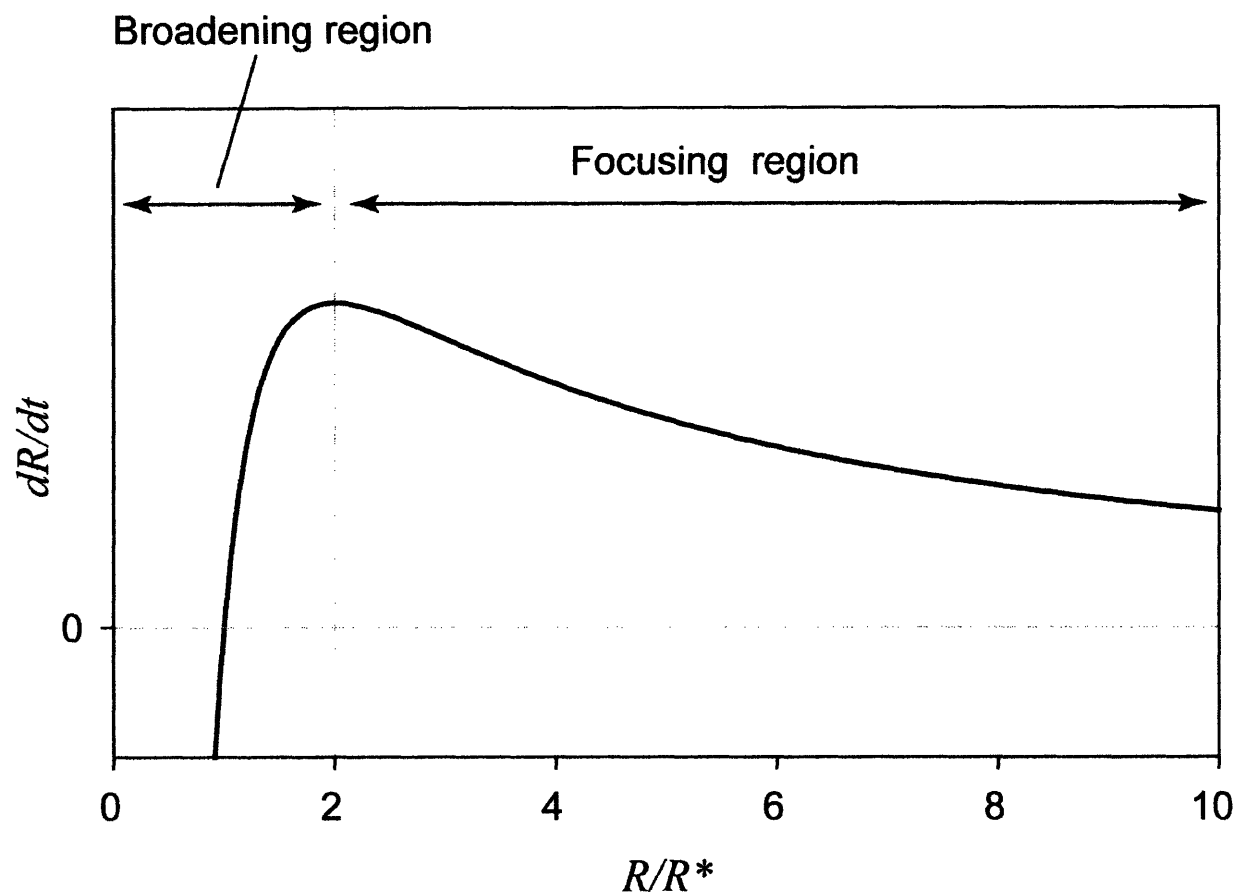


**Figure 1.9:** The variation of the growth rate of a single NC with particle radius. For an ensemble of NCs with sizes in the focusing regime, the size distribution will narrow as growth proceeds. If the NC sizes fall within the broadening regime, the ensemble will grow by an Ostwald ripening mechanism.



NCs is thermodynamically favored under some conditions (Ostwald ripening). Using the Gibbs-Thomson equation and assuming a steady-state flux of monomers and a thick diffusion layer ( $\delta \gg R$ ), the *single NC* growth rate dependence on size is given by:<sup>25</sup>

$$\frac{dR}{dt} = \frac{2\gamma DV_m^2 C_\infty}{k_B T} \frac{1}{R} \left( \frac{1}{R^*} - \frac{1}{R} \right) \quad \text{Eq. 1.3}$$

where  $D$  is the monomer diffusion coefficient, and  $R^*$  is the radius for which the growth rate is zero. The growth curve (figure 1.9) exhibits a maximum at  $R = 2R^*$ . For  $R > 2R^*$ , the growth rate decreases with increasing radius (smaller particles grow faster than larger ones), and the size distribution *narrows* with time. For  $R < 2R^*$ , smaller particles grow slower (or even dissolve) compared to larger particles, and growth proceeds by an Ostwald ripening mechanism, leading to *broadening* of the size distribution.

In the second limiting case, kinetic-controlled growth, the rate is limited by a reaction at the surface rather than mass transport from solution. The simplest mechanism is a first order reaction at the NC surface with rate constant  $k_r$ , and the single NC growth rate in this case is then given by:<sup>25</sup>

$$\frac{dR}{dt} = \frac{2\gamma k_r V_m^2 C_\infty}{k_B T} \left( \frac{1}{R^*} - \frac{1}{R} \right) \quad \text{Eq. 1.4}$$

In contrast to the diffusion controlled case, the  $dR/dT$  monotonically increases with  $R$  so that smaller NCs grow slower than larger ones, leading to broadening for all possible size distributions. Another important difference – which is not incorporated into these continuum models – is that under kinetic-control, growth will proceed fastest on the most reactive NC facet. In the diffusion-controlled case, the growth rate is determined by the equilibrium solubility of a particular NC facet. This has consequences in the growth of anisotropic NC morphologies and will be discussed in more detail in Chapter 6.

### 1.3 Synthesis of Colloidal Nanocrystals by Batch Methods

Many NC synthesis reactions appear to be qualitatively consistent with classical nucleation and growth models. In particular, diffusion-controlled growth arguments have been used to explain the observed narrowing and subsequent broadening of the size distribution during synthesis.<sup>26,27</sup> Early in the growth, the supersaturation of monomers is high so that essentially all of the particle sizes are larger than  $2R^*$ , and the size distribution sharpens (figure 1.9). As the growth continues and concentration of monomers is depleted,  $R^*$  increases so that eventually all of the sizes in the ensemble are less than  $2R^*$ , resulting in broadening of the size distribution. Thus, the preparation of monodisperse samples requires maintaining a relatively high monomer concentration throughout the process so that the growth does not proceed by Ostwald ripening. Moreover, the initial nucleation time should be relatively short so that the majority of the reaction time is spent in the growth focusing regime.

The above requirements are usually realized by performing NC synthesis using a “hot injection” method. In this method, small batches of NCs are prepared by rapidly injecting precursors into a heated flask containing a mixture of solvent and ligands. Relatively high temperatures are used ( $\sim 300^\circ\text{C}$ ) so that the precursors rapidly decompose to form monomer species, thereby ensuring a short nucleation burst followed by slower growth focusing on existing nuclei. High temperature also serves to anneal out defects and improve the crystallinity of the NCs. Reaction parameters including the solvent/ligands, precursors, temperature and growth time are chosen to optimize the ultimate final product quality. The first successful use of the hot injection method for preparation of semiconductor NCs was reported in 1993.<sup>28</sup> In this report, cadmium chalcogenide NCs were prepared using dimethylcadmium as a precursor and a mixture of organophosphine and organophosphine oxide as the coordinating solvent. The

chalcogenide source used was phosphine selenide, phosphine telluride, or bis(trimethylsilyl) sulfide. The paper is notable because monodisperse, luminescent, and crystalline NCs were prepared over a significant range of average sizes.

Following the 1993 report, the field of semiconductor NC synthesis grew rapidly as the hot injection method was extended to other compound semiconductors. For instance, II-VI,<sup>29-31</sup> IV-VI<sup>32,33</sup> and III-V<sup>26,34-37</sup> NCs with low polydispersity and relatively high quantum yields have been prepared in recent years. Moreover, since 1993, the chemistry for cadmium chalcogenide NCs has been modified and optimized substantially.<sup>38-40</sup> One notable recent trend is the shift away from pyrophoric organometallic compounds to the use of more stable metal salts as precursors. Additionally, the development of spherical NC preparations described above led to the synthesis of more complicated NC architectures. For instance, non-spherical NCs and heterostructured NCs composed of two or more different semiconductors have been reported. These materials will be discussed in more detail in Chapter 6.

Though a great deal of progress has been made in the field of NC synthesis, the batch process used to carry out the reaction suffers from several inherent drawbacks. The quality and average size of NCs synthesized using the hot injection method can depend strongly on factors which are difficult to control such as the injection rate, local temperature and concentration fluctuations, rate of stirring, and rate of cooling. In other words, the vessel temperature and mass transfer characteristics are not well-defined, and significant variation from batch to batch is commonly observed. These irreproducibility issues only become worse when one considers scaling up the NC reaction. From a kinetics standpoint, the ill-defined mixing and thermal characteristics of the batch method make it difficult to extract reliable mechanistic information, especially at short times.

## 1.4 Continuous Flow Microfluidic Reactors

Microreaction technology provides a means of overcoming the limitations inherent to the batch process. Coeval with the increasing interest in semiconductor NCs, a great deal of effort has been focused on developing microfluidic technologies for chemical synthesis. The motivation for using microchemical systems is that there are often fundamental advantages to carrying out reactions at the microscale compared to performing them using conventional macroscale processes. Microreactors have the potential to be widely adopted across a wide range of chemical reaction classes and industrial processes. These systems have already been used to carry out a multitude of organic reactions ranging from gas-liquid, homogeneous liquid, and gas-liquid-solid (catalyst) phase reactions. Integration of sensors, mixers and other actuators for reaction intensification and characterization is an important aspect of design development. The field of microreaction technology is broad and fascinating, and this thesis will focus on the problem of applying the technology to the synthesis of semiconductor NCs. For a broader overview of the field and information on microreactors applied to other types of chemistries, several reviews are available.<sup>41-44</sup>

Several characteristics make a continuous flow microfluidic system an attractive method for preparing semiconductor NCs. In contrast to the batch method, continuous flow systems perform reactions at steady state, making it possible to achieve better control and reproducibility (figure 1.10). Further benefits are realized by scaling down the reactor dimensions to micrometers, thereby reducing the consumption of reagents during the optimization process and improving the uniformity of temperature and residence times within the reaction volume. A microfluidic approach makes it possible to rapidly and continuously screen through important

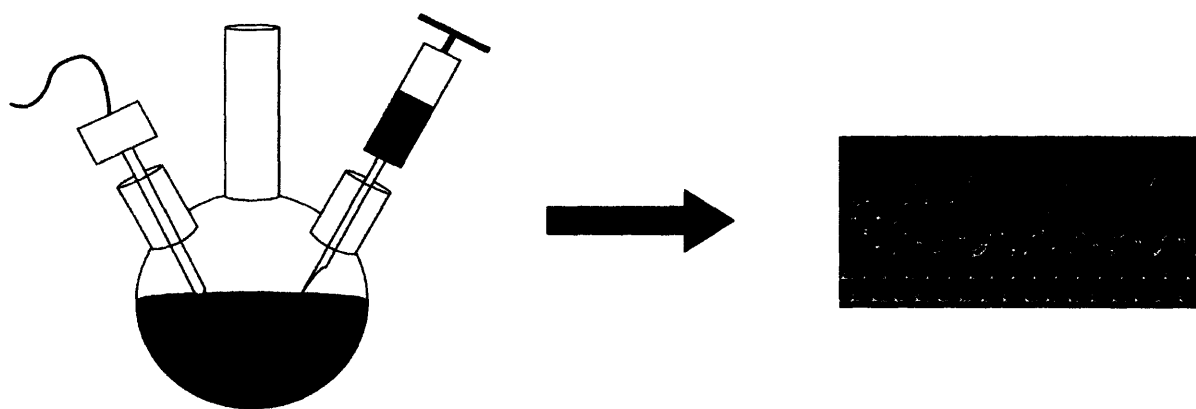


**Figure 1.10:** Comparison of batch and continuous flow microfluidic methods for NC synthesis. The microreactor shown on the right is discussed in Chapters 4 and 5.

reaction parameters, while using minimal amounts of reagents, until NCs of the desired size and monodispersity are produced. Each set of parameters would represent a separate reaction if the optimization procedure were performed using a batch process. After the optimal parameters are determined in a single microreactor, the NC reaction can be scaled up by replication and running many devices in parallel. The inherent advantages of a microfluidic flow system make it a natural choice for extracting mechanistic data on NC nucleation and growth processes, information which has proved difficult to obtain using conventional macroscale batch methods. Even at high flow rates corresponding to short reaction times, flow at the microscale occurs at Reynolds numbers<sup>45</sup> which are well below the turbulent regime. Compared to an uncontrolled hot injection process, the laminar flow in microchannels greatly simplifies the analysis of the heat and mass transfer effects on the kinetics of nucleation and growth. One disadvantage of these reactors is that slow diffusive mixing can pose a problem when carrying out reactions. However, several strategies can be employed to greatly improve the mixing characteristics in the laminar flow regime and will be discussed in further detail in Chapter 4.

## **1.5 Thesis Overview**

This thesis presents the design and application of several microfluidic reactors for NC synthesis. Chapter 2 describes the preparation of a size series of CdSe NCs using a simple single-phase capillary reactor. The heat and mass transfer analysis in Chapter 3 reveals that slow mixing and axial dispersion can have a strong influence on the ultimate quality of NC samples produced in the capillary reactor. Chapter 4 describes the design and fabrication of a gas-liquid segmented flow reactor which has superior mass transfer characteristics. In Chapter 5, the design is applied to preparation of CdSe NCs, and the results are compared with those obtained

using the single-phase flow approach. The segmented flow concept is extended in Chapter 6 in a reactor design capable of continuous addition of a second set of precursors. The microreactor is applied to the synthesis of heterostructured NCs. Chapter 7 concludes the thesis with a brief summary and some suggestions for future research.

## 1.6 References

1. Petroff, P. M.; Lorke, A.; Imamoglu, A., "Epitaxially self-assembled quantum dots." *Physics Today*, May 2001, 46-52.
2. Brus, L. E.; "Electron-electron and electron-hole interactions in small semiconductor crystallites: The size dependence of the lowest excited electronic state." *Journal of Chemical Physics* **1984**, *80*, 4403-4409.
3. Xia, J. B.; "Electronic structures of zero-dimensional quantum wells." *Physical Review B* **1989**, *40*, 8500-8507.
4. Norris, D. J.; Bawendi, M. G.; "Measurement and assignment of the size-dependent optical spectrum of CdSe quantum dots." *Physical Review B* **1996**, *53*, 16338-16346.
5. Efros, A. L.; Rosen, M.; "Quantum size level structure of narrow-gap semiconductor nanocrystals: effect of band coupling." *Physical Review B* **1998**, *58*, 7120-7134.
6. Efros, A. L.; Rosen, M.; "The electronic structure of semiconductor nanocrystals." *Annual Review of Materials Science* **2000**, *30*, 475-521.
7. Bruchez, M.; Moronne, M.; Gin, P.; Weiss, S.; Alivisatos, A. P.; "Semiconductor nanocrystals as fluorescent biological labels." *Science* **1998**, *281*, 2013-2016.
8. Mattoussi, H.; Mauro, J. M.; Goldman, E. R.; Anderson, G. P.; Sundar, V. C.; Mikulec, F. V.; Bawendi, M. G.; "Self-assembly of CdSe-ZnS quantum dot bioconjugates using an engineered recombinant protein." *Journal of the American Chemical Society* **2000**, *122*, 12142-12150.
9. Chan, W. C. W.; Maxwell, D. J.; Gao, X. H.; Bailey, R. E.; Han, M. Y.; Nie, S. M.; "Luminescent quantum dots for multiplexed biological detection and imaging." *Current Opinion in Biotechnology* **2002**, *13*, 40-46.
10. Stroh, M.; Zimmer, J. P.; Duda, D. G.; Levchenko, T. S.; Cohen, K. S.; Brown, E. B.; Scadden, D. T.; Torchilin, V. P.; Bawendi, M. G.; Fukumura, D.; Jain, R. K.; "Quantum

- dots spectrally distinguish multiple species within the tumor milieu in vivo." **2005**, *11*, 678-682.
11. Colvin, V. L.; Schlamp, M. C.; Alivisatos, A. P.; "Light-emitting diodes made from cadmium selenide nanocrystals and a semiconducting polymer." *Nature* **1994**, *370*, 354-357.
  12. Dabbousi, B. O.; Bawendi, M. G.; Onitsuka, O.; Rubner, M. F.; "Electroluminescence from CdSe quantum-dot/polymer composites." *Applied Physics Letters* **1995**, *66*, 1316-1318.
  13. Schlamp, M. C.; Peng, X.; Alivisatos, A. P.; "Improved efficiencies in light emitting diodes made with CdSe(CdS) core/shell type nanocrystals and a semiconducting polymer." *Journal of Applied Physics* **1997**, *82*, 5837-5842.
  14. Tessler, N.; Medvedev, V.; Kazes, M.; Kan, S.; Banin, U.; "Efficient near-infrared polymer nanocrystal light-emitting diodes." *Science* **2002**, *295*, 1506-1508.
  15. Coe, S.; Woo, W.-K.; Bawendi, M. G.; Bulović, V.; "Electroluminescence from single monolayers of nanocrystals in molecular organic devices." *Nature* **2002**, *420*, 800-803.
  16. Steckel, J. S.; Coe-Sullivan, S.; Bulović, V.; Bawendi, M. G.; "1.3 $\mu$ m to 1.55 $\mu$ m tunable electroluminescence from PbSe quantum dots embedded within an organic device." *Advanced Materials* **2003**, *15*, 1862-1866.
  17. Klimov, V. I.; Mikhailovsky, A. A.; Xu, S.; Malko, A.; Hollingsworth, J. A.; Leatherdale, C. A.; Eisler, H. J.; Bawendi, M. G.; "Optical gain and stimulated emission in nanocrystal quantum dots." *Science* **2000**, *290*, 314-317.
  18. Kazes, M.; Lewis, D. Y.; Ebenstein, Y.; Mokari, T.; Banin, U.; "Lasing from semiconductor quantum rods in a cylindrical microcavity." *Advanced Materials* **2002**, *14*, 317-321.
  19. Sundar, V. C.; Eisler, H. J.; Bawendi, M. G.; "Room-temperature, tunable gain media from novel II-VI nanocrystal-titania composite matrices." *Advanced Materials* **2002**, *14*, 739-743.
  20. Malko, A. V.; Mikhailovsky, A. A.; Petruska, M. A.; Hollingsworth, J. A.; Htoon, H.; Bawendi, M. G.; Klimov, V. I.; "From amplified spontaneous emission to microring lasing using nanocrystal quantum dot solids." *Applied Physics Letters* **2002**, *81*, 1303-1305.
  21. Chan, Y.; Snee, P. T.; Caruge, J.-M.; Yen, B. K.; Nair, G. P.; Nocera, D. G.; Bawendi, M. G.; "A solvent-stable nanocrystal-silica composite laser." *Journal of the American Chemical Society* **2006**, *128*, 3146-3147.



22. Mullin, J. W., *Crystallization*; 3rd ed.; Butterworth-Heinemann: Boston, 1993.
23. Adamson, A. W., *Physical Chemistry of Surfaces*; 5th ed.; Wiley: New York, 1990.
24. LaMer, V. K.; Dinegar, R. H.; "Theory, production and mechanism of formation of monodispersed hydrosols." *Journal of the American Chemical Society* **1950**, *72*, 4847-4854.
25. Sugimoto, T.; "Preparation of monodispersed colloidal particles." *Advances in Colloid and Interface Science* **1987**, *28*, 65-108.
26. Peng, X. G.; Wickham, J.; Alivisatos, A. P.; "Kinetics of II-VI and III-V colloidal semiconductor nanocrystal growth: "Focusing" of size distributions." *Journal of the American Chemical Society* **1998**, *120*, 5343-5344.
27. Murray, C. B.; Kagan, C. R.; Bawendi, M. G.; "Synthesis and characterization of monodisperse nanocrystals and close-packed nanocrystal assemblies." *Annual Review of Materials Science* **2000**, *30*, 545-610.
28. Murray, C. B.; Norris, D. J.; Bawendi, M. G.; "Synthesis and characterization of nearly monodisperse CdE (E = S, Se, Te) semiconductor nanocrystallites." *Journal of the American Chemical Society* **1993**, *115*, 8706-8715.
29. Hines, M. A.; Guyot-Sionnest, P.; "Bright UV-blue luminescent colloidal ZnSe nanocrystals." *Journal of Physical Chemistry B* **1998**, *102*, 3655-3657.
30. Li, L. S.; Pradhan, N.; Wang, Y.; Peng, X.; "High quality ZnSe and ZnS nanocrystals formed by activating zinc carboxylate precursors." *Nano Letters* **2004**, *4*, 2261-2264.
31. Rogach, A. L.; Harrison, M. T.; Kershaw, S. V.; Kornowski, A.; Burt, M. G.; Eychmuller, A.; Weller, H.; "Colloidally prepared CdHgTe and HgTe quantum dots with strong near-infrared luminescence." *Physica Status Solidi B-Basic Research* **2001**, *224*, 153-158.
32. Murray, C. B.; Sun, S. H.; Gaschler, W.; Doyle, H.; Betley, T. A.; Kagan, C. R.; "Colloidal synthesis of nanocrystals and nanocrystal superlattices." *IBM Journal of Research and Development* **2001**, *45*, 47-56.
33. Hines, M. A.; Scholes, G. D.; "Colloidal PbS nanocrystals with size-tunable near-infrared emission: Observation of post-synthesis self-narrowing of the particle size distribution." *Advanced Materials* **2003**, *15*, 1844-1849.
34. Guzelian, A. A.; Banin, U.; Kadavanich, A. V.; Peng, X.; Alivisatos, A. P.; "Colloidal chemical synthesis and characterization of InAs nanocrystal quantum dots." *Applied Physics Letters* **1996**, *69*, 1432-1434.

35. Cao, Y. W.; Banin, U.; "Synthesis and characterization of InAs/InP and InAs/CdSe core/shell nanocrystals." *Angewandte Chemie International Edition* **1999**, *38*, 3692-3694.
36. Cao, Y. W.; Banin, U.; "Growth and properties of semiconductor core/shell nanocrystals with InAs cores." *Journal of the American Chemical Society* **2000**, *122*, 9692-9702.
37. Battaglia, D.; Peng, X. G.; "Formation of high quality InP and InAs nanocrystals in a noncoordinating solvent." *Nano Letters* **2002**, *2*, 1027-1030.
38. Peng, Z. A.; Peng, X. G.; "Formation of high-quality CdTe, CdSe, and CdS nanocrystals using CdO as precursor." *Journal of the American Chemical Society* **2001**, *123*, 183-184.
39. Qu, L. H.; Peng, Z. A.; Peng, X. G.; "Alternative routes toward high quality CdSe nanocrystals." *Nano Letters* **2001**, *1*, 333-337.
40. Yu, W. W.; Peng, X.; "Formation of high-quality CdS and other II-VI semiconductor nanocrystals in noncoordinating solvents: tunable reactivity of monomers." *Angewandte Chemie-International Edition in English* **2002**, *41*, 2368-2371.
41. DeWitt, S. H.; "Microreactors for chemical synthesis." *Current Opinion in Chemical Biology* **1999**, *3*, 350-356.
42. Jähnisch, K.; Hessel, V.; Löwe, H.; Baerns, M.; "Chemistry in microstructured reactors." *Angewandte Chemie International Edition* **2004**, *43*, 406-446.
43. Jensen, K. F.; "Microchemical systems: status, challenges, opportunities." *AIChE Journal* **1999**, *45*, 2051-2054.
44. Jensen, K. F.; "Microreaction engineering – is smaller better?" *Chemical Engineering Science* **2001**, *56*, 293-303.
45. Bird, B. B.; Stewart, W. E.; Lightfoot, E. N., *Transport Phenomena*; 2nd ed.; Wiley: New York, 2002.

## Chapter 2

# A Single-Phase Liquid Capillary Reactor for Nanocrystal Synthesis<sup>†</sup>

### 2.1 Introduction

In this chapter, the preparation of CdSe NCs in a simple heated capillary reactor is presented. Coeval with the work described in this chapter, there were a few reports on the preparation of II-VI NCs in microreactors,<sup>1-3</sup> but these reports did not demonstrate the wide optical tunability, low polydispersities, and high quantum yields attainable in the batch process, nor did they extract new kinetic data on particle formation. In spite of the advantages of flow systems described in Chapter 1, it has been difficult to simply adopt the chemistry used in batch preparations of semiconductor NCs to a microfluidic flow reactor. CdSe is probably the most well characterized colloidal semiconductor NC system because its effective band gap can be tuned over the majority of the visible region. However, existing preparations are generally not amenable to a continuous flow system. As highlighted in the previous chapter, the most widely used preparation of high quality CdSe quantum dots involves the rapid injection of dimethyl cadmium and tri-n-octylphosphine selenide (TOPSe) into a hot solvent consisting of a mixture of tri-n-octylphosphine (TOP) and tri-n-octylphosphine oxide (TOPO).<sup>4</sup> The solvent also serves as the source of surface ligands for the growing NCs. This method ensures that nucleation occurs very rapidly, followed by slower particle growth on existing nuclei, and the particles produced can be reasonably monodisperse and crystalline. Several difficulties arise when this chemistry is

---

<sup>†</sup> Much of this chapter has appeared in print: B. K. H. Yen, N. E. Stott, K. F. Jensen, M. G. Bawendi, *Adv. Mater.* **2003**, *15*, 1858-1862.

implemented in a continuous flow system, the most obvious one being that the solvent is a solid at room temperature. Also, when  $(\text{CH}_3)_2\text{Cd}$  is used as a precursor, gas is rapidly evolved in the reaction, making it difficult to achieve reproducible reactor residence times. Finally, at the high reaction temperatures, TOPO can decompose and lead to clogging of the reactor channel, a problem that is only exacerbated as the channel dimensions are made smaller. Therefore, it was necessary to develop a new chemistry for CdSe NC synthesis that is more compatible with a microfluidic flow system. Guided by several recent reports on the preparation of semiconductor NCs,<sup>5-8</sup> cadmium oleate and TOPSe were chosen as the Cd and Se sources, respectively. These precursors are dissolved in a high-boiling solvent system consisting of squalane, oleyl amine, and TOP. This choice of precursors and solvent avoids problems of outgassing and clogging within the reactor channel, making it possible to use a simple capillary reactor to prepare CdSe NCs with excellent size distributions and high photoluminescence (PL) quantum yields. We also demonstrate that we can use the flow system to tune the band-edge absorbance (by varying the average NC size) over a substantial range.

## **2.2 Experimental**

### **2.2.1 Capillary Reactor Setup**

The continuous flow reactor (figure 2.1) consisted of a miniature convective mixer followed by a heated glass reaction channel (250 $\mu\text{m}$  I.D.) maintained at a constant temperature (180-320 $^\circ\text{C}$ ). The Cd and Se precursor solutions were delivered in two separate flows and combined in the mixing chamber before they reached the heated reaction section. The presence of the chamber was necessary because once the Cd and Se precursor solutions are combined at

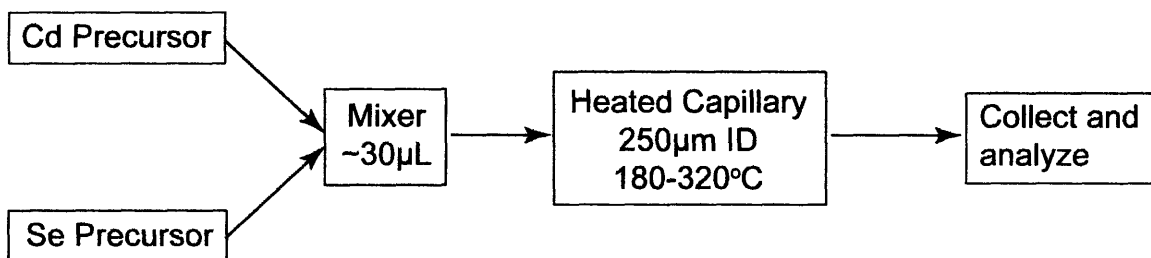


**Figure 2.1:** Experimental setup for the capillary reactor system.

room temperature, small CdSe clusters form over several hours. Since this cluster formation resulted in irreproducibility in the sizes of the final NCs produced by the reactor, the Cd and Se precursors could not be mixed until just prior to reaching the heated section. The volume of the mixer (~30 $\mu$ L) was chosen such that the chamber residence time was long enough (~1 to 15 minutes depending on flow rate) to ensure complete mixing but short enough to avoid formation of small clusters.

The reactor consisted of a length of glass tubing with a 250 $\mu$ m channel diameter placed inside an aluminum heating chuck. Heating was provided by cartridge heaters inserted within the aluminum block, and the temperature was monitored using a small thermocouple inserted next to the glass tubing. The total length of the heating section was 14.6 cm. In order to prevent formation of N<sub>2</sub> bubbles in the heated section, the Cd and Se precursor solutions were thoroughly degassed at 90 °C before being carefully drawn into syringes. The precursor solutions were then delivered in two separate flows with syringe pumps. After combining the two flows with a tee, the fluid reached a miniature convective mixing chamber containing a magnetic stir bar. After the mixing chamber, the precursors flowed into the heated section, where they quickly reacted to form NCs. The NC solution was then collected for absorption and photoluminescence measurements.

### **2.2.2 Synthetic Methods and Optical Characterization**

Typically, a Cd precursor solution was prepared by heating a suspension of 74.8 mg (0.5 mmol) Cd(OH)<sub>2</sub>, 350  $\mu$ L (2.2 mmol) oleic acid (cis-9-octadecenoic acid), and 9 mL squalane (2,6,10,15,19,23-hexamethyltetracosane) at 150 °C under vacuum. After approximately 10 minutes, the solution became optically clear, at which point the temperature was lowered to

100°C. The solution was further degassed for at least 90 minutes to remove any excess water. Upon cooling to room temperature, 4 mL oleyl amine (cis-1-amino-9-octadecene) were added. The Se precursor solution was prepared by diluting a portion of a 1.5 M TOPSe/TOP stock solution in squalane. The 1.5 M TOPSe/TOP stock solution was prepared as previously reported.<sup>4</sup> All of the above manipulations were performed under a dry N<sub>2</sub> atmosphere.

Optical absorption spectra were acquired using a Hewlett-Packard 8453 diode array spectrometer. Photoluminescence spectra were acquired using a SPEX Fluorolog 1680 spectrometer, using right-angle collection. Samples were prepared by diluting the raw NC solutions in hexanes. Quantum yields were determined by comparing the integrated emission of a given NC sample solution with that of an appropriate reference dye. The following dyes (and quantum yields) were used: Rhodamine 560 chloride in basic ethanol (92%), Rhodamine 590 chloride in methanol (89%), Rhodamine 610 chloride in methanol (57%), and Rhodamine 640 perchlorate in methanol (100%).

## 2.3 Results and Discussion

The excellent stability of the capillary reactor was demonstrated by continuously flowing precursors through the reactor for 8 h. Absorbance spectra taken of the NCs sampled during these long runs were indistinguishable from each other (figure 2.2). By systematically varying the temperature, flow rate, and concentration it was possible to finely tune the size of NCs produced in the reactor. Figure 2.3 summarizes some results for a fixed precursor composition. Average NC radii were determined from the position of the band-edge absorbance peak and calibration curves based on TEM and X-ray scattering results (figure 1.5 in Chapter 1).<sup>4,9,10</sup> The

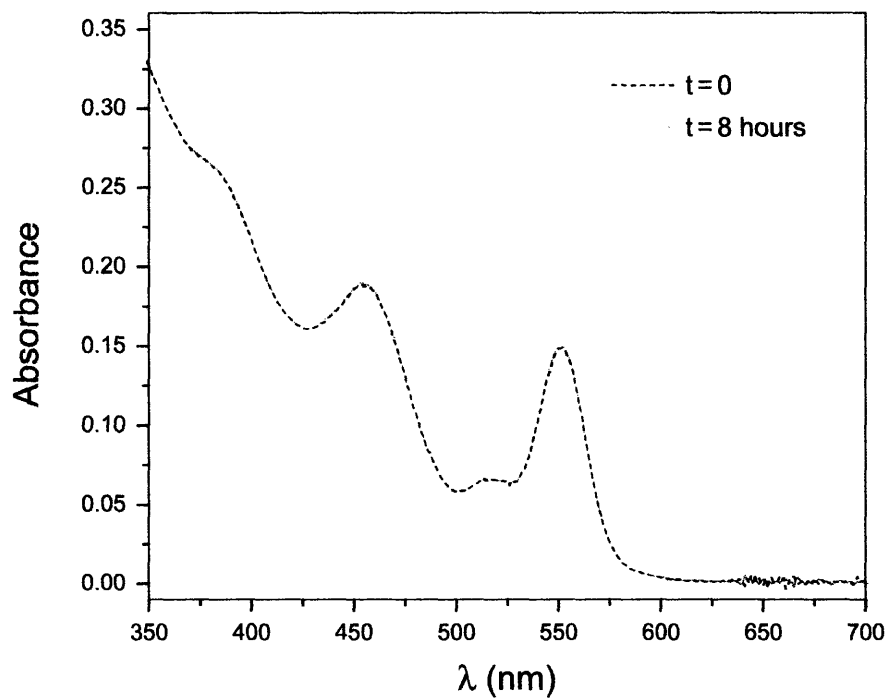


**Figure 2.2:** Stability of the capillary reactor over 8 hours of continuous operation. Absorbance spectra of samples taken at the beginning and end of the run are shown.  $T = 280^{\circ}\text{C}$ ,  $3\mu\text{L}/\text{min}$ , 15:1 Se:Cd.



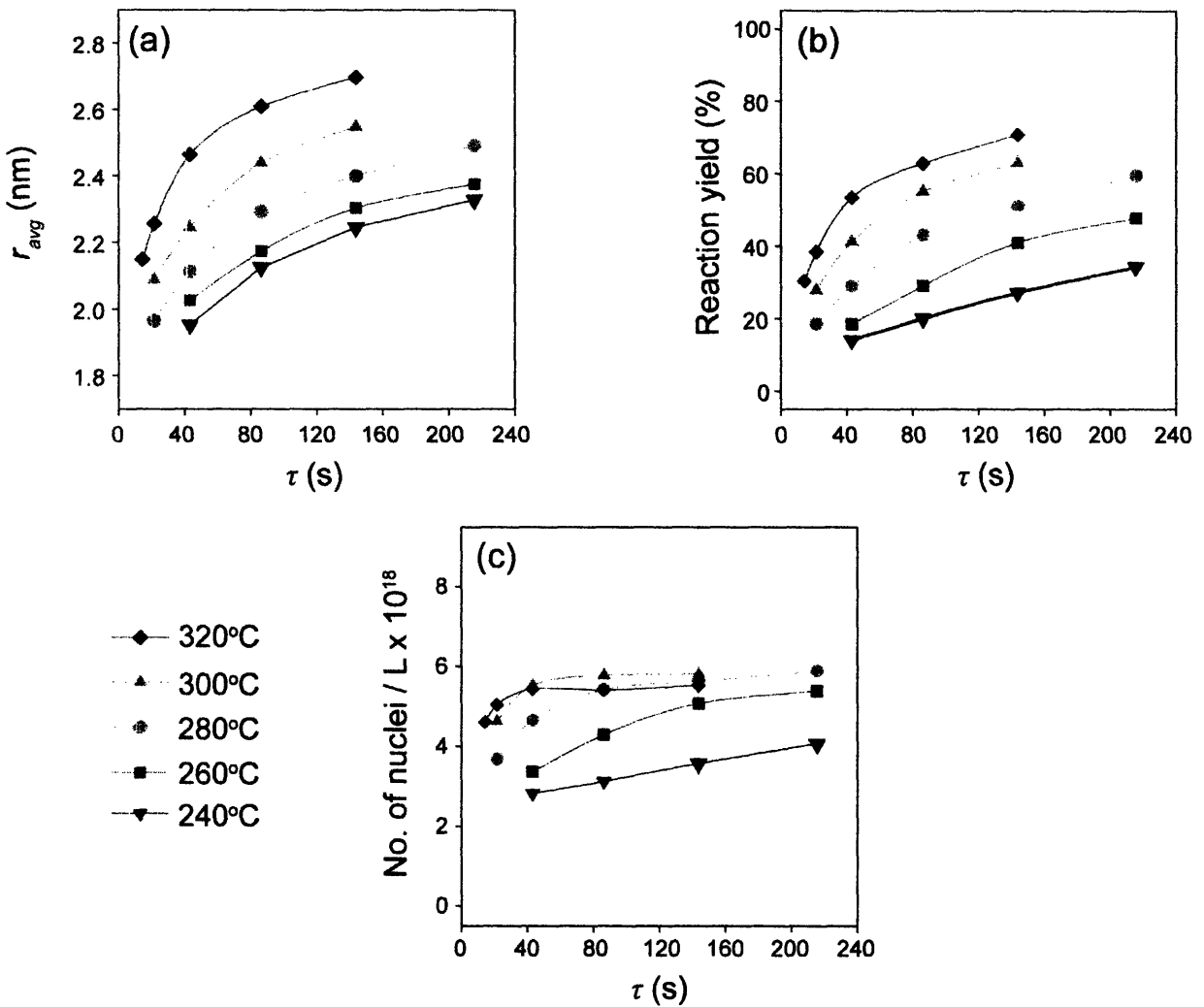


**Figure 2.3:** (a)-(c) Results for NCs prepared using a 1:1 Se:Cd precursor composition.  $\tau$  is the residence time in the heated section. The spectra, average radii ( $r_{avg}$ ), and size distributions for samples represented by the red diamonds in this figure are shown in figures 2.4a-b. A similar data set for samples along the dashed line is shown in figures 2.4c-d.

reaction yield and number of nuclei/volume were determined from the optical density and absorbance cross-section at 350 nm as previously reported.<sup>11</sup> As expected, higher reaction yields and the production of larger NCs were observed as the residence time or temperature is increased. In figure 2.3c, the assumption has been made that the number of NCs is equal to the number of nuclei, which is true as long as growth does not proceed extensively by an Ostwald ripening mechanism. In Ostwald ripening, the concentration of monomers is low enough that smaller dots dissolve at the expense of larger dots, and a decrease in the number of dots would be observed with sufficiently long growth time. In all of the data presented here, the residence time was kept short enough so that this process did not occur.

Representative spectra for samples prepared at a constant temperature (figure 2.4a) or constant flow rate (figure 2.4c) illustrate some important general trends. Though the average NC size can be tuned by changing the reactor conditions, we observed a corresponding variation in the size distribution of samples produced (figures 2.4b,d). In particular, the ratio of the size distribution to average radius ( $\sigma_r/r_{avg}$ ) becomes unacceptably large (>10 %) at extremes of low temperatures or high flow rates. At the other extremes, as explained below, the kinetics of nucleation and growth place an upper limit on the temperature and a lower limit on the flow rate. In other words, changing reactor conditions makes it possible to vary the average NC size over a wide range, but only at the expense of increasing polydispersity. Given the relatively narrow range of monodisperse sizes available by simply changing the reactor conditions, we sought to access a larger range by systematically varying the precursor concentration. Figure 2.5a illustrates that increasing the TOPSe concentration, while keeping the cadmium oleate

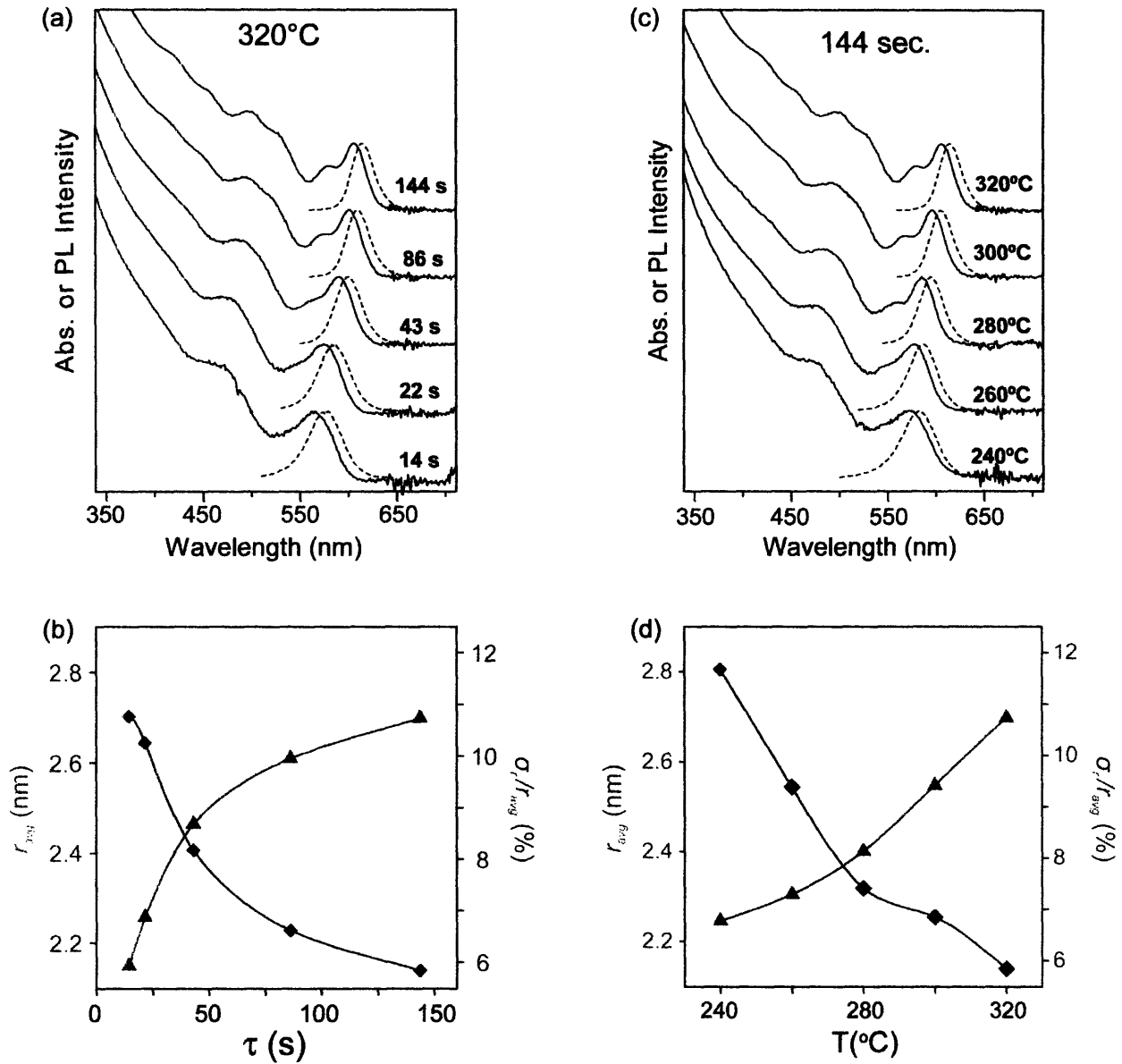


**Figure 2.4:** (a) Absorbance and PL spectra for samples produced at various flow rates while keeping temperature (320°C) and precursor concentration (1:1 Se:Cd) constant. (b) Corresponding average NC size and size distribution ( $\sigma_r$ ) of the samples represented in a). (c) Spectra for samples prepared at various temperatures while keeping the flow rate ( $\tau = 144$  s) and precursor concentration constant. (d) Corresponding average NC size and width of the size distribution of the samples represented in (c). The size distribution of each sample was determined from the PL peak width assuming a linewidth of  $\sim 50$  meV for the emission of a single NC at room temperature.

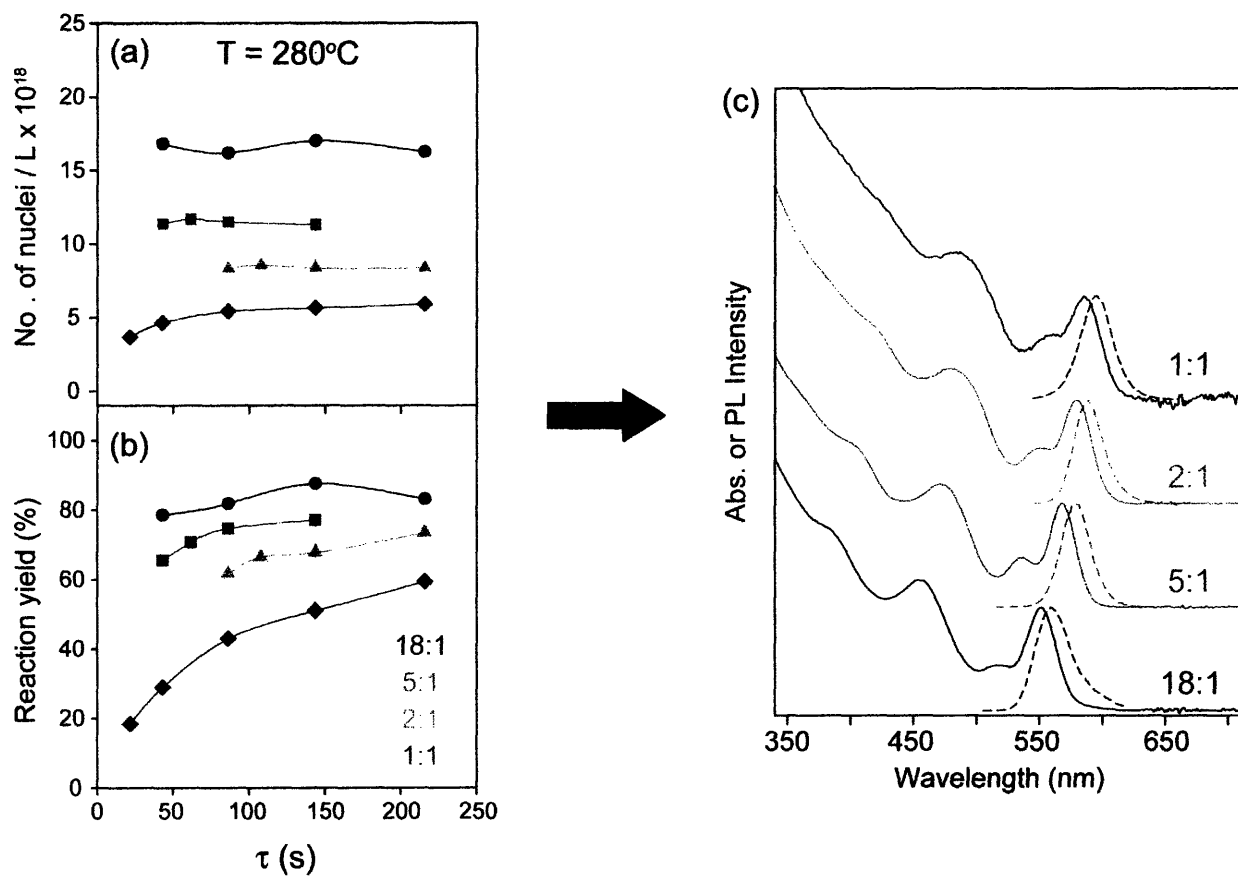


**Figure 2.5:** (a) Dependence of the number of nuclei on the concentration of TOPSe for a reactor temperature of 280°C. The cadmium oleate concentration was fixed. (b) The corresponding reaction yields for the reaction conditions in (a). (c) Absorbance and PL spectra for samples along the dashed line ( $\tau = 144$  s).

concentration constant, leads to a dramatic increase in the number of nuclei that are formed. With more (less) nuclei on which to grow, smaller (larger) dots are formed, and the position of the first absorbance peak shifts accordingly (figure 2.5c).

By controlling the nucleation event, it is possible to rationally tune the effective band gap of the NCs continuously over a substantial range while maintaining excellent size distributions. Figure 2.6 shows the absorbance and PL spectra of a size series of NCs with absorbance maxima ranging from 510 to 606 nm (average radii from  $\sim 1.5$  to  $\sim 2.7$  nm). Four TOPSe concentrations (1:1, 2:1, 5:1, and 18:1 Se:Cd) were used to obtain the size series shown. By controlling the number of nuclei systematically with concentration, we were able to access four size ranges, and within each range, the temperature and flow rates were varied to more finely tune the average NC size. The high PL quantum yields (between 28-51%), primarily due to the presence of amines, and the narrow emission peak widths (full-width-half-maximum between 27-34 nm) indicate the excellent quality of the samples shown in figure 2.6.

An important result described above is the variation of the size distribution with temperature or flow rate. Understanding this trend provides insight into reactor design issues and underlying nucleation and growth processes. For instance, figures 2.4a,b show that the size distribution becomes unacceptably broad as the flow rate is increased (reaction time decreased). Nonuniformity of reaction conditions across the channel can contribute to broadening of the size distribution. A heat transfer calculation shows that upon entering the heated section, the fluid at the center of the channel heats to within  $5^{\circ}\text{C}$  of the target temperature in  $\sim 0.3$  seconds. The fluid thermal conductivity, density, and heat capacity, were estimated from several references, and constant temperature boundary conditions at the wall were used. The full details of the

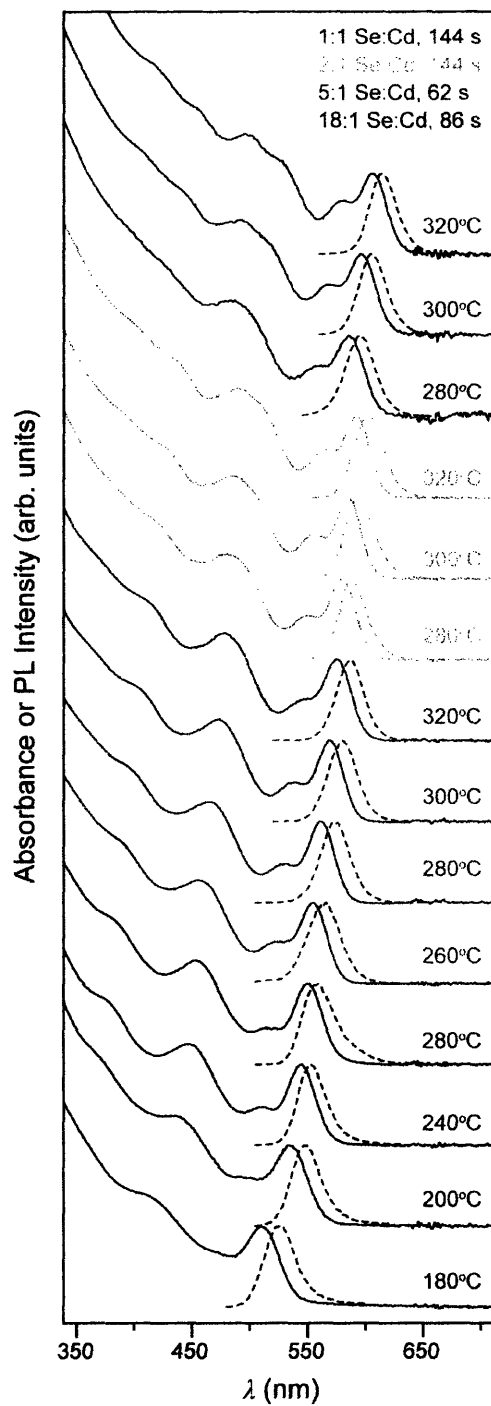


**Figure 2.6:** Size series for samples prepared using four TOPSe concentrations – 1:1 Se:Cd, 2:1 Se:Cd, 5:1 Se:Cd, and 18:1 Se:Cd. For each TOPSe concentration, the average NC size was controlled by varying the temperature at a fixed flow rate.

calculation and estimation of fluid properties will be given in the next chapter. Given such a rapid rate of heating, one can conclude that the dispersion in reaction conditions is dominated by the residence time distribution (RTD). For laminar flow in a cylindrical channel, the flow takes on a parabolic velocity profile so that NCs in the center move faster than those near the channel wall. Superimposed on this flow profile is the radial diffusion of NCs across the channel, and the combination gives rise to a distribution of residence times experienced by NCs exiting the reaction section. The residence time  $\tau$  shown in figures 2.3-2.5, for example, is technically an *average* residence time. The width of the RTD function ( $\sigma_t$ ) can be estimated using the Taylor dispersion model. Briefly, in this model, the extent of axial dispersion is characterized by a dispersion coefficient,  $D^* = \frac{u^2 R^2}{48D}$ , where  $R$  is the radius of the channel,  $u$  is the average flow velocity, and  $D$  is the diffusion coefficient. Further details of the dispersion calculation are given in the next chapter. From  $\sigma_t$  and the size vs. time curve (figure 2.4b, triangles), the RTD contribution to the overall size distribution was calculated. At shorter times, the RTD effect is significant, accounting for ~60% of the overall size distribution for  $\tau = 14$  s. At longer times, the RTD effect becomes negligible, accounting for <10% of the overall size distribution for the longest  $\tau$  shown in the figure (144 s). This analysis partially explains the narrowing of the overall size distribution with increased reaction time.

The underlying kinetics of NC formation also play an important role in the observed size distributions in figure 2.4b. Under certain conditions, there is a natural distribution in growth rates with size that results in narrowing of the size distribution. As described in Chapter 1, for steady-state, diffusion-controlled growth of a spherical particle, the growth rate ( $dR/dt$ ) as a function of particle radius ( $R$ ) has a maximum at a critical radius  $R_{cr} = 2R^*$ . For  $R > R_{cr}$ , the growth rate decreases with increasing radius (smaller particles grow faster than larger ones), and

the size distribution narrows with time. For  $R < R_{cr}$ , smaller particles grow slower or even dissolve compared to larger particles (Ostwald ripening), and this leads to broadening of the size distribution (figure 1.9 in Chapter 1). If the growth rate is also dictated by reaction at the surface (mixed diffusion and kinetic control), the growth rate can still have a maximum at some critical radius, and the curve still exhibits focusing and defocusing regions.<sup>12</sup> These arguments have been used to explain the observed narrowing and subsequent broadening of the size distribution during the batch synthesis of semiconductor NCs.<sup>13</sup> In such a preparation, supersaturation of monomers is high early in the growth so that essentially all of the particle sizes are larger than  $R_{cr}$ , and the size distribution sharpens. As the growth continues and concentration of monomers is depleted,  $R_{cr}$  increases so that eventually all of the sizes are less than  $R_{cr}$ , and the size distribution broadens. For NCs prepared in a flow reactor, the combination of the RTD and growth focusing/defocusing define an optimal range of flow rates that can produce monodisperse samples. For times shorter than this range, the dispersion in residence times is large, and the growth focusing does not proceed long enough to compensate, resulting in poor quality samples. For very short times, nucleation is incomplete, further broadening the size distribution. For times longer than the optimal range, the concentration of monomer decreases enough so that growth proceeds by Ostwald ripening and the size distribution begins to broaden. Under some conditions, such as a very broad initial size distribution, it is possible for Ostwald ripening to lead to narrowing of the size distribution.<sup>12</sup> Such conditions were not present in the data shown here.

The dependence of size distribution on temperature (figure 2.4d) can also be explained from kinetic arguments, in particular from the nucleation data shown in figure 2.3c. With the exception of the 240°C curve, the number of nuclei increases with time and then saturates to a



constant value. This is consistent with existing nucleation and growth models in which NC formation proceeds by a simultaneous nucleation and growth period followed by purely growth on existing nuclei. Since the kinetics of nucleation and growth are strongly temperature dependent, the formation of nuclei (the rising portion of the curves in figure 2.3c) takes substantially longer as the temperature is lowered. In fact, at 240°C, the nucleation is slowed so much that even at the longest residence time shown (216 s), nucleation is incomplete, and the curve does not saturate. Therefore, at lower temperatures, the kinetics are slowed to such an extent that the majority or all of the residence time is characterized by mixed nucleation and growth (the curves in figure 2.3c have not saturated), resulting in poor size distributions. At high temperatures, nucleation ends quickly so that the majority of the time spent in the heated section is purely characterized by growth focusing. Another important observation is that the curves in figure 2.3c approach essentially the same value. In other words, changing the temperature affects the rate of nucleation, but the *final number of nuclei formed remains essentially constant*. Thus, with this chemistry there is a fundamental limit on the range of sizes that may be accessed by changing the temperature.

In order to access a larger size range while maintaining acceptable size distributions, we systematically varied the concentration of the TOPSe precursor (figure 2.5). Nucleation can often be described by an exponential relationship with the supersaturation ratio (Eq. 1.1 in Chapter 1) so it is not surprising that the CdSe NC nucleation rate is very sensitive to the initial precursor (TOPSe) concentration. Increasing the TOPSe concentration increases the nucleation rate *relative* to the growth, resulting in formation of a larger number of nuclei as shown in figure 2.5a, which summarizes the effect of varying the TOPSe concentration at constant cadmium oleate concentration and reactor temperature. Also, a higher TOPSe concentration resulted in

faster overall reaction kinetics as indicated by higher reaction yields (figure 2.5b). This is due to two effects: first, a higher concentration of precursors results in faster overall kinetics, and secondly, a higher concentration of nuclei on which to grow results in faster depletion of monomers in solution.

## 2.4 Conclusions

In summary, a combination of the RTD and intrinsic nucleation and growth processes place restrictions on the range of sizes that can be accessed for a given precursor concentration. By changing the TOPSe concentration, it is possible to control the nucleation rate, thereby enabling the use of a simple capillary reactor to produce high quality CdSe NCs with sizes corresponding to a wide spectral range. A continuous flow system serves as a powerful kinetic tool for elucidating NC nucleation and growth kinetics. The arguments used to describe the nucleation and growth process and the corresponding variations in size distribution can be applied generally.

The limitations imposed by the broad RTDs in the capillary system can be addressed by introducing a segmented, rather than a homogeneous flow into the reactor. In such an approach, the flow is comprised of small, alternating segments of two different phases moving through the heated section. Each segment behaves essentially like a miniature stirred tank reactor, so that molecules within each segment experience a very uniform RTD. In a previous report on the preparation of CdSe NCs with a flow system,<sup>2</sup> researchers used a segmented flow by introducing N<sub>2</sub> bubbles into the precursor stream, and they observed somewhat improved size distributions in comparison to the single-phase flow case. Similar results were observed with the capillary reactor when a lower boiling solvent was used (di-n-octyl ether rather than squalane). At

temperatures greater than  $\sim 280^{\circ}\text{C}$ , the solvent boils within the heated section, forming alternating segments of gas and liquid within the channel. However, it was difficult to estimate the flow velocity of the fluid in the heated region due to the nature of the bubble formation. In Chapters 4-6, more sophisticated microreactor designs are presented which apply the segmented flow concept to NC synthesis.

## 2.5 References

1. Chan, E. M.; Mathies, R. A.; Alivisatos, A. P.; "Size-controlled growth of CdSe nanocrystals in microfluidic reactors." *Nano Letters* **2003**, *3*, 199-201.
2. Nakamura, H.; Yamaguchi, Y.; Miyazaki, M.; Maeda, H.; Uehara, M.; Mulvaney, P.; "Preparation of CdSe nanocrystals in a micro-flow reactor." *Chemical Communications* **2002**, 2844-2845.
3. Edel, J. B.; Fortt, R.; deMello, J. C.; deMello, A. J.; "Microfluidic routes to the controlled production of nanoparticles." *Chemical Communications* **2002**, 1136-1137.
4. Murray, C. B.; Norris, D. J.; Bawendi, M. G.; "Synthesis and characterization of nearly monodisperse CdE (E = S, Se, Te) semiconductor nanocrystallites." *Journal of the American Chemical Society* **1993**, *115*, 8706-8715.
5. Murray, C. B.; Sun, S. H.; Gaschler, W.; Doyle, H.; Betley, T. A.; Kagan, C. R.; "Colloidal synthesis of nanocrystals and nanocrystal superlattices." *IBM Journal of Research and Development* **2001**, *45*, 47-56.
6. Peng, Z. A.; Peng, X. G.; "Formation of high-quality CdTe, CdSe, and CdS nanocrystals using CdO as precursor." *Journal of the American Chemical Society* **2001**, *123*, 183-184.
7. Qu, L. H.; Peng, Z. A.; Peng, X. G.; "Alternative routes toward high quality CdSe nanocrystals." *Nano Letters* **2001**, *1*, 333-337.
8. Bawendi, M. G.; Stott, N. E. "Preparation of Nanocrystallites." *US Patent 6,576,291*; 2003.
9. Mattoussi, H.; Cumming, A. W.; Murray, C. B.; Bawendi, M. G.; Ober, R.; "Properties of CdSe nanocrystal dispersions in the dilute regime: Structure and interparticle interactions." *Physical Review B* **1998**, *58*, 7850-7863.

10. Kuno, M. K. "Band edge spectroscopy of CdSe quantum dots." Ph.D. Thesis, Massachusetts Institute of Technology, Cambridge, MA, 1998.
11. Leatherdale, C. A.; Woo, W.-K.; Mikulec, F. V.; Bawendi, M. G.; "On the absorption cross section of CdSe nanocrystal quantum dots." *Journal of Physical Chemistry B* **2002**, *106*, 7619-7622.
12. Talapin, D. V.; Rogach, A. L.; Haase, M.; Weller, H.; "Evolution of an ensemble of nanoparticles in a colloidal solution: theoretical study." *Journal of Physical Chemistry B* **2001**, *105*, 12278-12285.
13. Peng, X. G.; Wickham, J.; Alivisatos, A. P.; "Kinetics of II-VI and III-V colloidal semiconductor nanocrystal growth: "Focusing" of size distributions." *Journal of the American Chemical Society* **1998**, *120*, 5343-5344.

## Chapter 3

### Analysis of Heat and Mass Transfer Effects

#### 3.1 Heat Transfer

##### 3.1.1 The Graetz-Nusselt Problem

In the last chapter, it was stated that the fluid entering the heated reaction section reaches the target temperature rapidly, in  $\sim 0.3$ s. The details of the calculation of the channel temperature profile are described in this section. The coordinate system and boundary conditions used in the calculation are summarized in figure 3.1.  $r = 0$  is chosen to correspond to the tube centerline. We consider a fluid flowing in a tube with radius  $R$ . The fluid is initially at temperature  $T_e$  until it reaches a region with a constant wall temperature  $T_w$ . The goal is to solve for the temperature profile within the fluid for  $z > 0$ .

The steady-state temperature profile within the reactor is found by solving the energy balance equation where we have assumed that viscous dissipation is negligible, fluid density and heat capacity are constant, and the fluid is incompressible ( $\nabla \cdot \mathbf{v} = 0$ ).<sup>1</sup>

$$\rho C_p \mathbf{v} \cdot \nabla T = k \nabla^2 T \quad \text{Eq. 3.1}$$

In the above equation,  $\rho$  is the density,  $C_p$  is the heat capacity,  $\mathbf{v}$  is the fluid velocity, and  $k$  is the thermal conductivity. Equation 3.1 is subject to the following boundary conditions:

$$T(R, z) = T_w \quad T(r, 0) = T_e \quad T(0, z) \text{ is finite} \quad \text{Eqs. 3.2a-c}$$

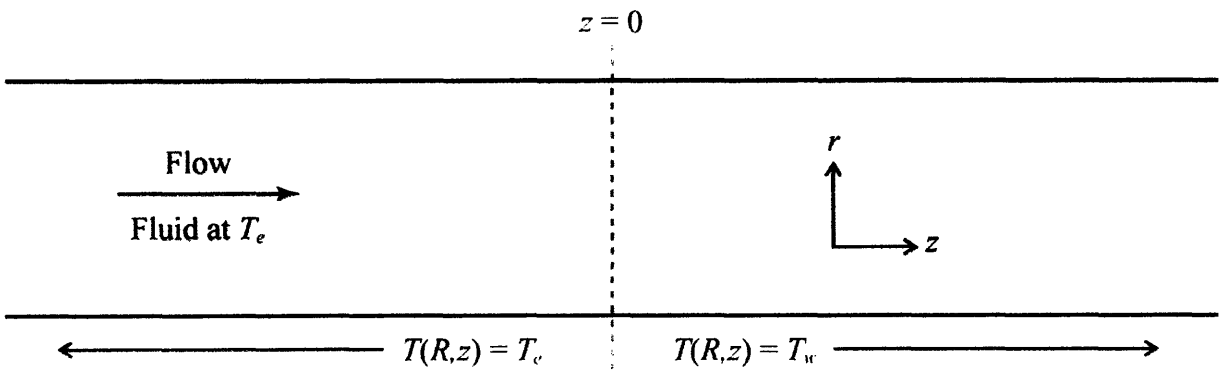


**Figure 3.1:** Cylindrical coordinate system and boundary conditions defining the Graetz-Nusselt problem.

The fluid velocity in the  $z$  direction is given by the well-known equation for fully-developed laminar flow in circular channels:<sup>1</sup>

$$v(r) = 2v_{avg} \left[ 1 - \left( \frac{r}{R} \right)^2 \right] \quad \text{Eq. 3.3}$$

Next, equation 3.1 can be written in cylindrical coordinates and the expression for the velocity profile (equation 3.3) substituted into equation 3.1. From symmetry,  $T = T(r, z)$  and  $\mathbf{v} = v(z)$  so any terms containing  $\theta$ ,  $v_r$ , or  $v_\theta$  are zero. Furthermore, axial heating can be neglected so the term containing  $\partial^2 T / \partial z^2$  is also zero. Thus, the final differential equation describing the energy balance in the tube is given by:

$$2v_{avg} \left[ 1 - \left( \frac{r}{R} \right)^2 \right] \frac{\partial T}{\partial z} = \frac{k}{\rho C_p} \left[ \frac{1}{r} \frac{\partial}{\partial r} \left( r \frac{\partial T}{\partial r} \right) \right] \quad \text{Eq. 3.4}$$

It is convenient to rewrite the above in terms of dimensionless quantities:

$$\Theta = \frac{T_w - T}{T_w - T_e} \quad \eta = \frac{r}{R} \quad \psi = \frac{zk}{2\rho C_p v_{avg} R^2} \quad \text{Eq. 3.5a-c}$$

Introducing the above transformations into equation 3.4 and equations 3.2a-c results in the following:

$$(1 - \eta^2) \frac{\partial \Theta}{\partial \psi} = \frac{1}{\eta} \frac{\partial}{\partial \eta} \left( \eta \frac{\partial \Theta}{\partial \eta} \right) \quad \text{Eq. 3.6}$$

$$\Theta(1, \psi) = 0 \quad \Theta(\eta, 0) = 1 \quad \Theta(0, \psi) \text{ is finite} \quad \text{Eqs. 3.7a-c}$$

The solution to equation 3.6 can be found by the method of separation of variables, and we look for solutions of the form:

$$\Theta(\eta, \psi) = X(\eta)Y(\psi) \quad \text{Eq. 3.8}$$

Substituting equation 3.8 into 3.6 and rearranging results in two ordinary differential equations.

The differential equation containing  $Y(\psi)$  can be integrated directly, and  $Y(\psi)$  takes the form:

$$Y(\psi) = \exp(-\lambda^2 \psi) \quad \text{Eq. 3.9}$$

where  $-\lambda^2$  is an the integration constant. The differential equation containing  $X(\eta)$  is given by

$$\frac{\partial}{\partial \eta} \left( \eta \frac{\partial X}{\partial \eta} \right) + \lambda^2 \eta (1 - \eta^2) X = 0 \quad \text{Eq. 3.10}$$

$$X(0) \text{ is finite} \quad X'(0) \text{ is finite} \quad X(1) = 0 \quad X'(1) = 0 \quad \text{Eqs. 3.11a-d}$$

The equation and boundary conditions (equations 3.10-3.11) are in the form of a Sturm-Liouville problem, so its solutions are given by a set of eigenfunctions  $\{X_n\}$  and eigenvalues  $\{\lambda_n^2\}$ .

Therefore, the general solution to equation 3.6 is an infinite sum containing  $X_n$  and  $\lambda_n^2$ :

$$\Theta(\eta, \psi) = \sum_{n=0}^{\infty} A_n X_n(\eta) \exp(-\lambda_n^2 \psi) \quad \text{Eqs. 3.12}$$

Since the eigenfunctions are orthogonal, the weighting coefficient ( $A_n$ 's) can be found by applying the boundary condition  $\Theta(\eta, 0) = 1$  and taking the Sturm-Liouville inner product with  $X_n(\eta)$ .

$$A_n = \frac{\langle \Theta(\eta, 0), X_n(\eta) \rangle}{\langle X_n(\eta), X_n(\eta) \rangle}$$

$$A_n = \frac{\int_0^1 \eta(1-\eta^2) X_n(\eta) d\eta}{\int_0^1 \eta(1-\eta^2) X_n^2(\eta) d\eta} \quad \text{Eq. 3.13}$$

Thus, the temperature profile  $\Theta(\eta, \psi)$  is completely determined by equations 3.12 and 3.13. In general, the eigenfunctions, eigenvalues, and weighting coefficients cannot be found analytically. However, they are tabulated for  $n \leq 10$  in a number of references<sup>2,3</sup> and reproduced below.



**Table 3.1:** Eigenvalues  $\lambda_n$  and Constants  $A_n$ 

$n$	$\lambda_n$	$A_n$
0	2.70436	1.47643
1	6.67903	-0.80612
2	10.67337	0.58876
3	14.67107	-0.47585
4	18.66987	0.40502
5	22.66914	-0.35575
6	26.66866	0.31916
7	30.66832	-0.29073
8	34.66807	0.26789
9	38.66788	-0.24906
10	42.66773	0.23322

**Table 3.2:** Eigenfunctions  $R_n(r/R)$  for values of  $r/R$ 

$n$	$R_n(r/R)$								
	$r/R = 0.1$	0.2	0.3	0.4	0.5	0.6	0.7	0.8	0.9
0	0.98184	0.92889	0.84547	0.73809	0.61460	0.48310	0.35101	0.22426	0.10674
1	0.89181	0.60470	0.23386	-0.10959	-0.34214	-0.43218	-0.39763	-0.28449	-0.14113
2	0.73545	0.15247	-0.31521	-0.39208	-0.14234	0.16968	0.33149	0.30272	0.16262
3	0.53108	-0.23303	-0.35914	0.06793	0.31507	0.11417	-0.19604	-0.29224	-0.17762
4	0.30229	-0.40260	0.00054	0.29907	-0.07973	-0.25523	0.03610	0.25918	-0.18817
5	0.07488	-0.32121	0.28982	-0.04766	-0.20532	0.19750	0.10372	-0.20893	-0.19522
6	-0.12642	-0.07613	0.20122	-0.25168	0.19395	-0.01391	-0.18883	0.14716	0.19927
7	-0.28107	0.17716	-0.10751	0.03452	0.05514	-0.15368	0.20290	-0.07985	-0.20068
8	-0.37523	0.29974	-0.25305	0.22174	-0.20502	0.19303	-0.15099	0.01298	0.19967
9	-0.40326	0.23915	-0.08558	-0.02483	0.08126	-0.09176	0.05652	0.04787	-0.19645
10	-0.36817	0.04829	0.16645	-0.20058	0.13289	-0.06474	0.04681	-0.09797	0.19120

$R_n(0) = 1$  and  $R_n(1) = 0$  for all  $n$

For  $n > 10$ , the following asymptotic forms for  $\lambda_n$ ,  $A_n$ , and  $X_n(\eta)$  can be used with little loss in precision:<sup>4</sup>

$$\lambda_n = 4n + \frac{8}{3} \quad \text{Eq. 3.14}$$

$$X_n(\eta) = \begin{cases} J_0(\lambda_n \eta), & \text{for small } \eta \text{ (near center)} \\ \sqrt{\frac{2}{\pi \lambda_n \eta}} \frac{\cos\left[\left(\frac{\lambda_n}{2}\right)\eta\sqrt{1-\eta^2} + \left(\frac{\lambda_n}{2}\right)\sin^{-1}(\eta) - \frac{\pi}{4}\right]}{(1-\eta^2)^{1/4}}, & \text{for medium } \eta \\ \sqrt{\frac{2(1-\eta)}{3}} (-1)^n J_{1/3}\left(\frac{\lambda_n \sqrt{8}}{3} (1-\eta)^{3/2}\right), & \text{for large } \eta \text{ (near wall)} \end{cases} \quad \text{Eq. 3.15}$$

$$C_n = (-1)^n \frac{2 \cdot 6^{2/3} \Gamma(2/3)}{\pi} \lambda^{-2/3} \quad \text{Eq. 3.16}$$

In the above equations,  $J_m$  denotes an  $m^{\text{th}}$  order Bessel function of the first kind.

From the results summarized in tables 3.1-3.2 and equations 3.14-3.16, eigenvalues, eigenfunctions, and coefficients were calculated. The sum defining  $\Theta(\eta, \psi)$  (equation 3.12) converged to sufficient accuracy after calculating the first 60 terms. The resulting plot of the tube temperature profile in dimensionless variables is shown in figure 3.2.

### 3.1.2 Results for Capillary Reactor

For the capillary system described in Chapter 2, the actual fluid properties needed to be estimated to calculate the temperature profile in the heated section. Based on data in several references,<sup>5-7</sup> the heat capacity  $C_p$  and thermal conductivity  $k$  were estimated to be  $0.1 \text{ W m}^{-1} \text{ K}^{-1}$  and  $3 \text{ J g}^{-1} \text{ K}^{-1}$ , respectively. The fluid density  $\rho$  was estimated to be  $0.9 \text{ g cm}^{-3}$ . These fluid properties and channel dimensions were then substituted into equation 3.5 for the dimensionless variables, and the full temperature profile within the capillary was recovered. Since the center

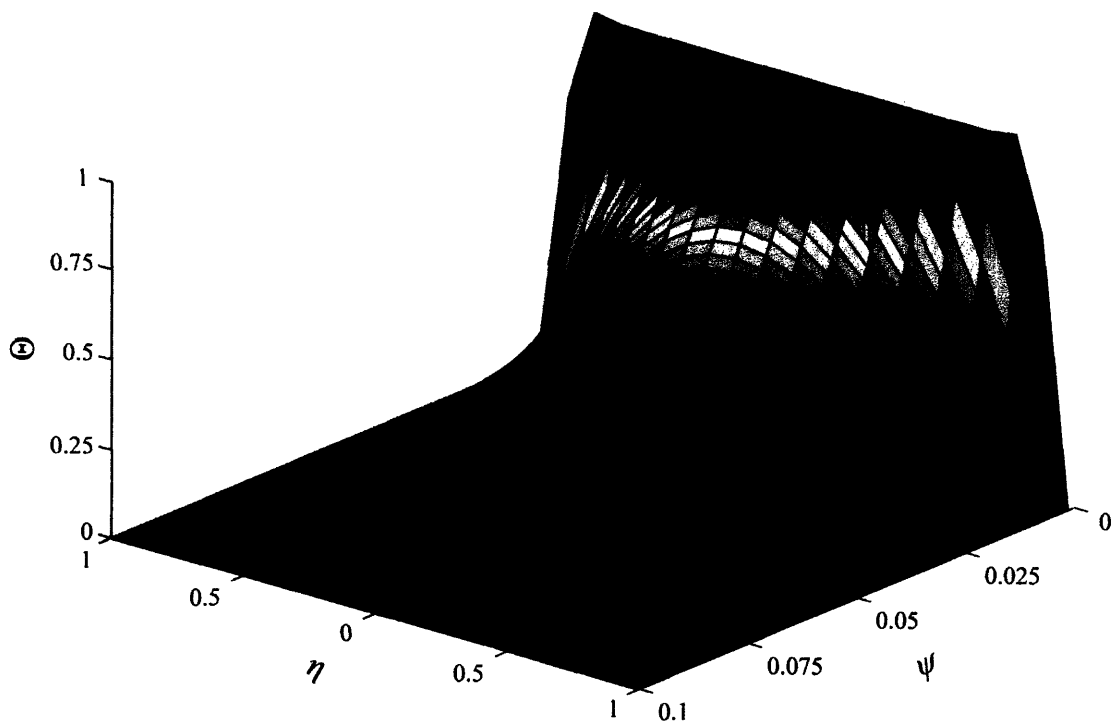


**Figure 3.2:** Temperature profile within the heated section of the tube. Dimensionless variables for temperature ( $\Theta$ ), radial distance ( $\eta$ ), and axial distance ( $\psi$ ) are defined in eqs. 3.5a-c.

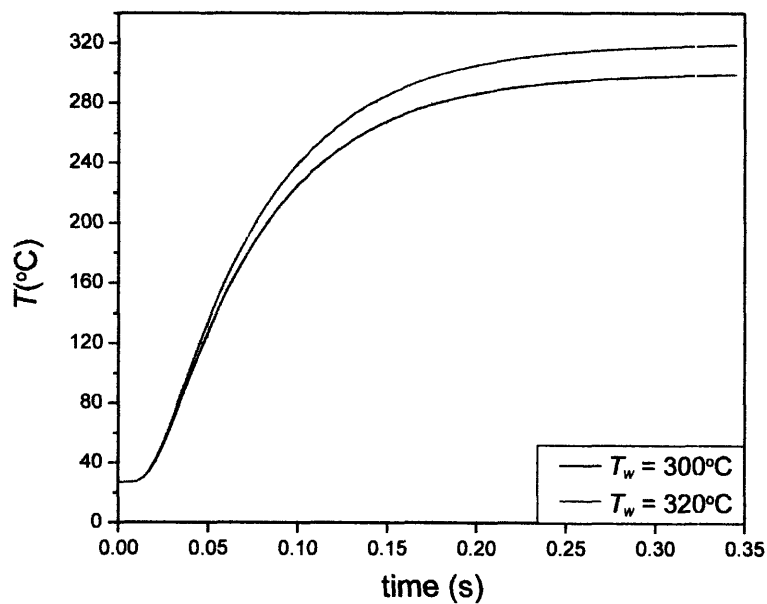


**Figure 3.3:** Temperature of the fluid entering the reaction zone as a function of time for a 250 $\mu\text{m}$  capillary. Two target (wall) temperatures are shown.

of tube takes the longest time to heat up, it is particularly useful to examine the profile along the center-line of the calculated temperature field. This temperature profile along  $r = 0$  is more experimentally relevant when plotted in terms of time rather than  $z$ , which can be accomplished through the use of the following transformation:

$$t = \frac{z}{2v_{avg}} = \frac{\rho C_p R^2}{k} \quad \text{Eq. 3.17}$$

The temperature trajectory of the fluid at the center of the capillary is shown in figure 3.3. The figure shows that the fluid entering the reaction zone heats to within 5°C of the target temperature very rapidly (within ~0.3 sec). Also, it is important to note that (from equation 3.17) this characteristic heating time is independent of flow rate.

## 3.2 Mass Transfer

### 3.2.1 Mixing Effects

As described in Chapter 2, the cadmium and selenium precursors react together slowly at room temperature to form small CdSe clusters. In order to ensure stable, reproducible results during runs, the two precursors cannot be in contact with each other for long periods of time prior to reaching the heated section of the capillary. Therefore, the Cd and Se precursors were delivered in separate syringes, and the two flows combined with a tee upstream from the capillary.

The time for the two streams in the capillary to become completely mixed can strongly influence the quality of the product and places a limit on the timescales accessible with the

reactor. The system mixing time can be estimated by calculating the time for a precursor molecule to diffuse across the capillary diameter:<sup>8</sup>

$$t = \frac{\langle x^2 \rangle}{2D} \quad \text{Eq. 3.18}$$

where the mean square distance travelled  $\langle x^2 \rangle$  is set equal to the capillary diameter. The diffusion coefficient  $D$  of a precursor molecule of radius  $a$  can be estimated from the Stokes-Einstein relation:<sup>8</sup>

$$D = \frac{kT}{6\pi a\mu} \quad \text{Eq. 3.19}$$

The fluid viscosity  $\mu$  at various temperatures is extrapolated from experimental values for squalane using a modified Arrhenius expression.<sup>9</sup> Depending on the reaction temperature and choice of radius  $a$ , a realistic mixing time for the capillary system ranges from 30 seconds to several minutes. In contrast to the heating time (Section 3.2), the precursor streams will mix over a timescale that is comparable to or longer than the overall reaction time. As described in the previous chapter, the slow diffusive mixing of the system was overcome by placing a miniature convective mixing chamber in-line with the flow. This ensured complete mixing of the precursors before they reached the heated section of the capillary. The volume of the mixer (~30  $\mu\text{L}$ ) was chosen such that the chamber residence time was long enough (~1 to 15 minutes depending on flow rate) to ensure complete mixing but short enough to avoid formation of small clusters.

### 3.2.2 Residence Time Distribution (RTD) Effects

A second mass transport effect which can strongly influence the quality of the NCs produced in the reactor is the system residence time distribution (RTD). Since the velocity profile of the flow in the capillary (eq 3.3) is parabolic, the particles in the center of the channel move faster and spend less time in the reactor in comparison to particles moving slowly near the wall. The result is that there is a distribution of residence times for the products coming out of the reactor. This dispersion in reaction times directly contributes to the overall size distribution of the product. Molecules or particles are simultaneously diffusing laterally across the streamlines which tends to counteract the effects of the nonuniform flow profile (figure 3.4). However, as pointed out in the previous section, the characteristic diffusion timescale is slow, and the RTD can still be quite broad under typical reaction conditions.

The starting point for determining the dispersion properties of a system is the analysis of an imaginary tracer experiment. Consider a short pulse of tracer molecules (with the same diffusion properties as the molecules or particles of interest) injected into the entrance ( $z = 0$ ) of the capillary of length  $L$ . Initially, the tracer concentration  $C(r, z, t)$  takes on a  $\delta$ -function concentration profile. As the pulse moves down the channel, it spreads due to velocity gradients (convection) and diffusion effects described above. An important experimentally measurable variable is the mean concentration  $C_m$  in the plane  $z = z_0$ . One can imagine continually measuring, say, the absorbance or fluorescence signal across the channel exit ( $z = L$ ) as the pulse passes by. The measured signal will then be proportional to  $C(z = L, t)$ . The signal time trace (or  $C_m(z = L, t)$ ) is proportional to the fraction of tracer molecules which had a

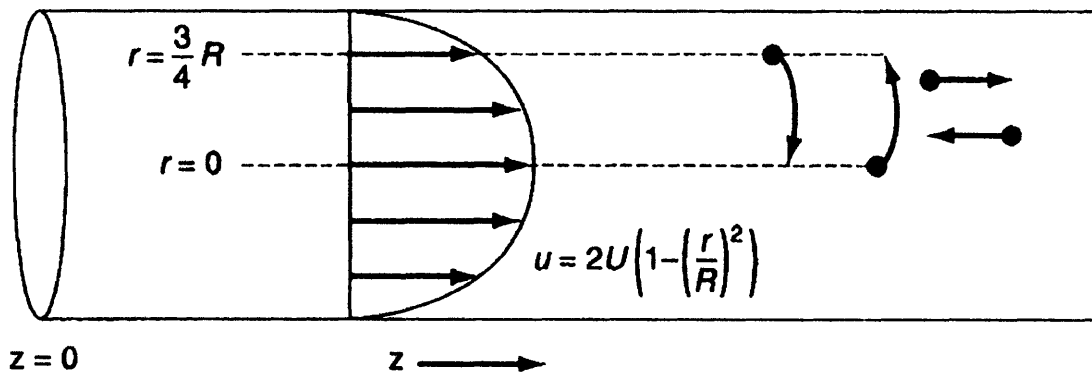


**Figure 3.4:** Schematic illustrating the source of the RTD in a cylindrical channel. The parabolic velocity profile and diffusion of molecules across streamlines is shown. From reference 10.

residence time between  $t$  and  $t + dt$ . In other words,  $C_m(z = L, t)$ , properly normalized, gives the RTD function of the system. By convention, the distribution function is called the  $E$ -curve in the literature.  $C_m(z, t)$  is found by solving for the spatial and temporal evolution of the tracer concentration  $C(r, z, t)$ , which is described by the full convection-diffusion equation.<sup>10</sup>

$$\frac{\partial C}{\partial t} + v(r) \frac{\partial C}{\partial z} = D \left[ \frac{1}{r} \frac{\partial}{\partial r} \left( r \frac{\partial C}{\partial r} \right) + \frac{\partial^2 C}{\partial z^2} \right] \quad \text{Eq. 3.20}$$

$$C_m(z, t) = \frac{1}{\pi R^2} \int_0^R C(r, z, t) 2\pi r dr \quad \text{Eq. 3.21}$$

Even for cylindrical channels and laminar flow, the complete solution to equations 3.20-3.21 must be found numerically. However, there are two important limiting cases which are useful for a large number of situations.

In the first case, the flow conditions are such that the width of the  $E$ -curve is not very large relative to the average residence time. It is then possible to simplify the calculation greatly using a one-parameter model which is usually just called the dispersion model. In this model, the spreading of the tracer plug is assumed to obey Fick's Law of Diffusion except an axial dispersion coefficient  $D^*$  is used in place of the diffusion coefficient:<sup>10-12</sup>

$$\frac{\partial C_m}{\partial t} = D^* \frac{\partial^2 C_m}{\partial z^2} \quad \text{Eq. 3.22}$$

The solution equation 3.22 is a family of curves that are Gaussian in  $z$ , and the  $E$ -curve is subsequently found by setting  $z = L$  in the expression for  $C_m$ . It is also useful to define adimensionless time  $\theta$  such that  $\theta = 1$  approximately corresponds to the mean residence time.



$$\theta = \frac{t}{\tau} \qquad \tau = \frac{L}{v_{avg}} \qquad \text{Eq. 3.23a-d}$$

$$E(\theta) = C_m(L, \theta) = \frac{1}{\sqrt{4\pi\theta\left(\frac{D^*}{v_{avg}L}\right)}} \exp\left[-\frac{(1-\theta)^2}{4\theta\left(\frac{D^*}{v_{avg}L}\right)}\right] \qquad \text{Eq. 3.24}$$

The variance  $\sigma_t$  of the  $E$ -curve is given by

$$\frac{\sigma_t^2}{\tau^2} = 2\frac{D^*}{v_{avg}L} + 8\left(\frac{D^*}{v_{avg}L}\right)^2 \qquad \text{Eq. 3.25}$$

The  $E$ -curves for various values of  $D^*/v_{avg}L$  are shown in figure 3.5. At smaller values, the RTD curve narrows and becomes more symmetric. This corresponds to slower flow rates (longer mean residence times) or a higher diffusion coefficient. As expected, in the limit of zero dispersion, the curve approaches that of an ideal plug flow reactor. It should be noted that the dispersion model is not accurate for large extents of axial dispersion (large  $D^*$ ). However, the trend of increased broadening and skewness at high flow rates or low diffusion coefficients shown in the curves is qualitatively correct.

Under conditions where the dispersion model is valid (small extents of dispersion),  $D^*$  takes on a closed-form expression containing flow speed, fluid properties, and geometrical factors. Taylor<sup>13</sup> was the first to derive the correlation for  $D^*$  in a cylindrical tube of radius  $R$ . Aris<sup>14</sup> later extended the Taylor expression to be valid over a wider range of flow conditions.

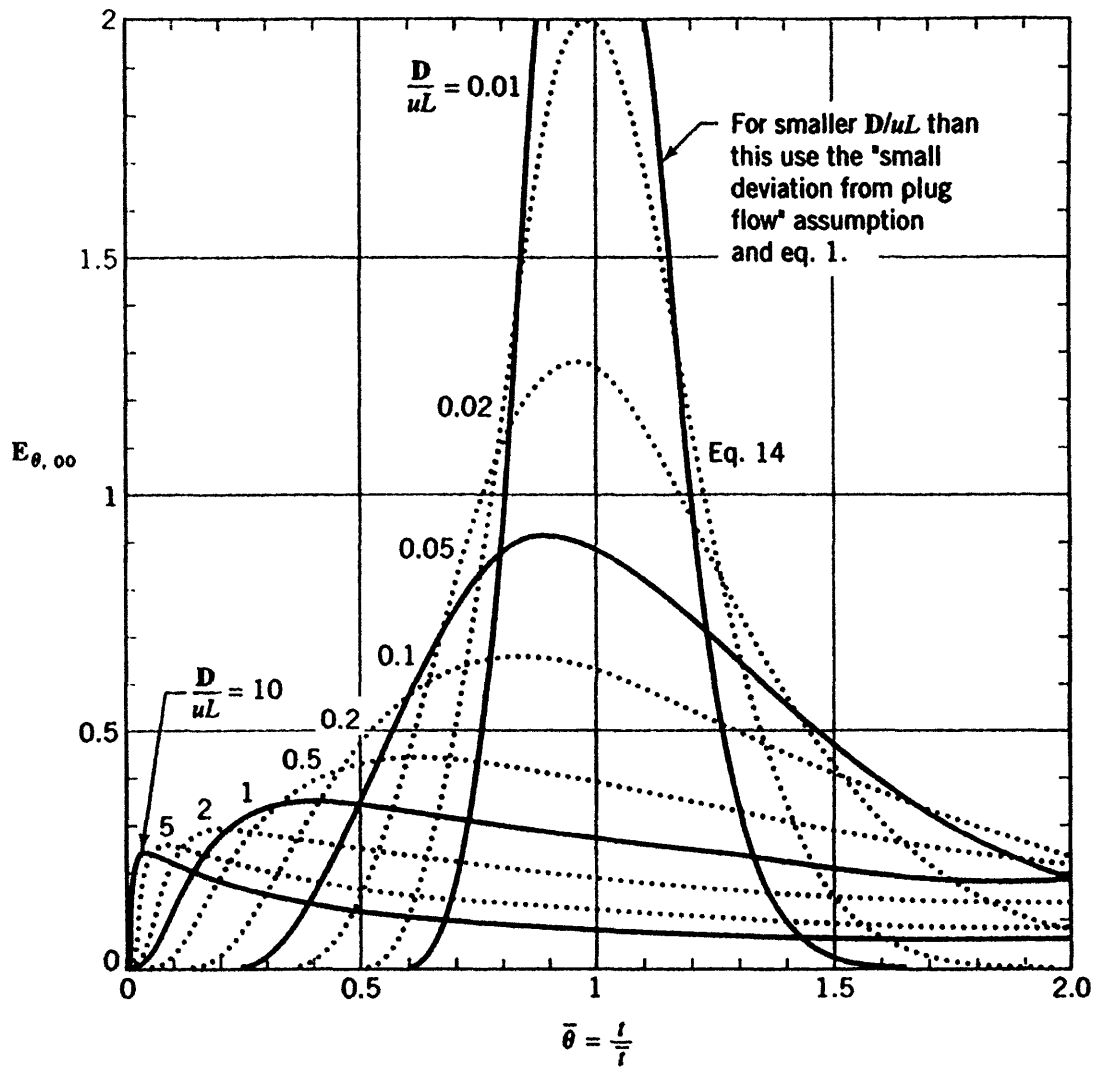


**Figure 3.5:**  $E$ -curves for open-open boundary conditions and various values of the axial dispersion coefficient.  $D$  corresponds to  $D^*$ , and  $u$  corresponds to  $v_{avg}$  in the text. From reference 11.

$$D^* = \frac{v_{avg}^2 R^2}{48D} \quad \text{Taylor} \quad \text{Eq. 3.26}$$

$$D^* = D + \frac{v_{avg}^2 R^2}{48D} \quad \text{Taylor-Aris} \quad \text{Eq. 3.27}$$

Here  $D$  is the diffusion coefficient of the tracer species and should not be confused with the axial dispersion coefficient  $D^*$ .

The second limiting case to consider is the pure convection regime. In this regime, diffusion does not contribute to the overall RTD, and the only source of spreading of the tracer pulse is due to convection (fluid velocity gradients). This occurs at high flow rates and/or low diffusion coefficients. The derivation of the  $E$ -curve for laminar flow in cylindrical tubes under such conditions is straightforward.<sup>10,11</sup> In contrast to the case of small dispersion, the shape of the curve is a monotonically decreasing function from  $\tau \leq t < \infty$ .

$$E(t) = \begin{cases} 0 & \text{for } t < \tau/2 \\ \frac{\tau^2}{2t^3} & \text{for } t \geq \tau/2 \end{cases} \quad \text{Eq. 3.28}$$

In the preceding discussion, the conditions over which either the dispersion or pure convection model are valid were qualitatively discussed. For practical implementation, however, the exact flow regimes over which these models are valid need to be identified. Figure 3.6 provides such a regime diagram and is adapted from several references.<sup>11,15</sup> The diagram is given in terms of flow conditions and channel aspect ratio. For the intermediate regime, neither the pure convection nor the dispersion model can be used. Instead, the full convection-diffusion equation must be solved numerically. Alternatively, values from regions bracketing the intermediate point can be calculated and averaged.

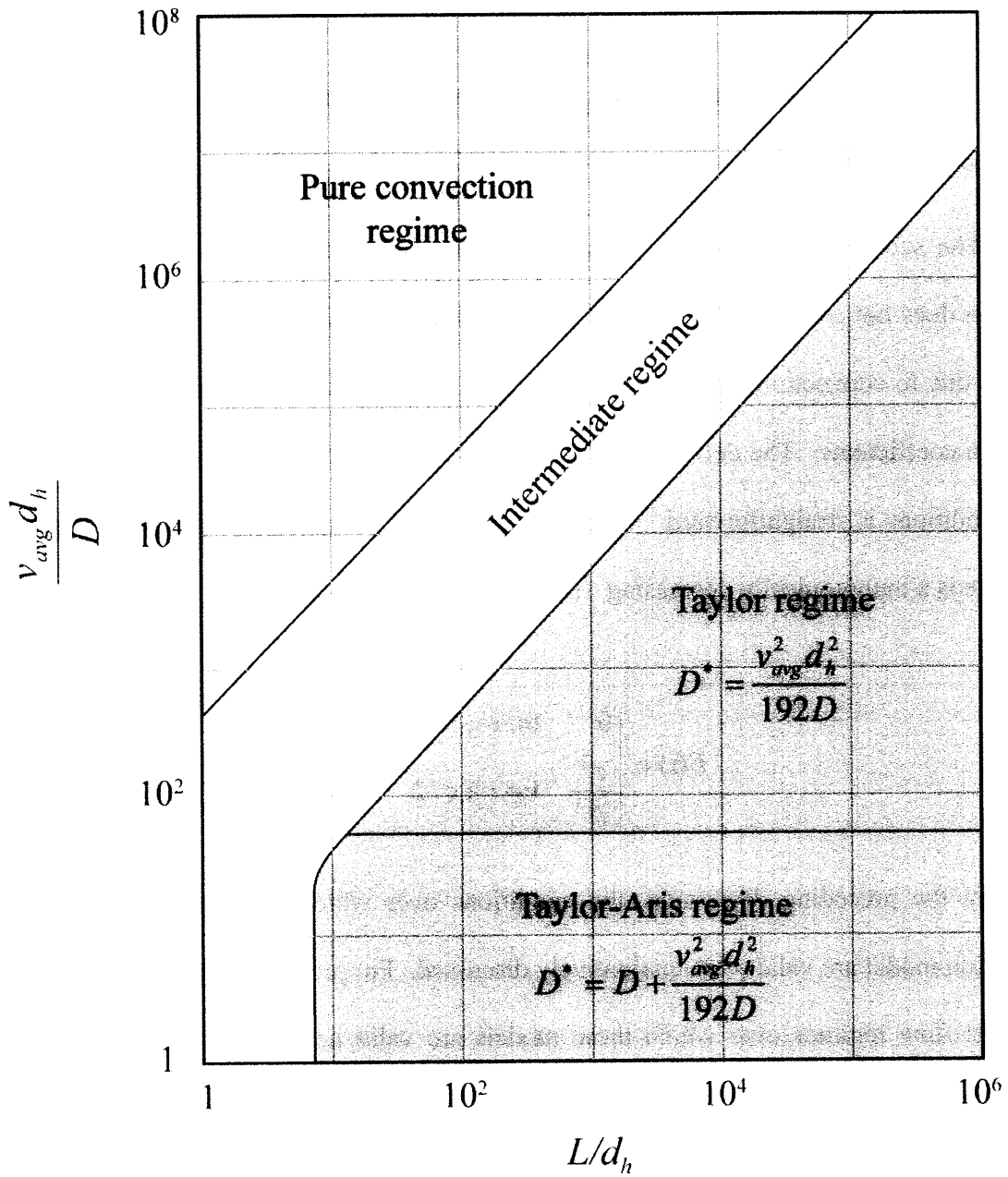


**Figure 3.6:** Regime diagram showing regions of validity for the dispersion model and pure convection model. The hydraulic diameter  $d_h$  is used rather than tube diameter for generality. Adapted from references 11 and 15.

### 3.2.3 Influence of RTD on Size Distribution

As stated in the previous chapter, the RTD contributes significantly to the overall size distribution produced in the reactor. This detrimental effect on the sample quality is due to the flow maldistribution and diffusion, independent of the underlying NC nucleation and growth chemistry. The extent of the RTD contribution can be estimated using the results from section 3.2.2. For a given flow condition (residence time) in the reactor, the width of the residence time dispersion  $dt$  can be estimated either from equations 3.25-3.27 for the dispersion regime or from equation 3.28 for flow in the convection regime. The dispersion in time  $dt$  can then be converted into dispersion in NC radius  $dr$  from the growth curves. The procedure is shown in figure 3.7.

For the shortest times, the RTD effect is more pronounced and the growth curve is steepest. As described in the previous chapter, the RTD accounts for the majority of the observed width of the size distribution (~60%). At the longest times, where the RTD curve becomes narrower and the growth curve flattens out, the RTD contribution decreases until it accounts for a small fraction of the overall size distribution (<5%) at the longest residence times. It should be noted that depending on the NC size (diffusion coefficient) and flow rate, some of the experimental values fell within the intermediate regime in figure 3.6. In these cases, RTD dispersion values were calculated based on the two neighboring regimes (convection model and Taylor/Taylor-Aris) and averaged.

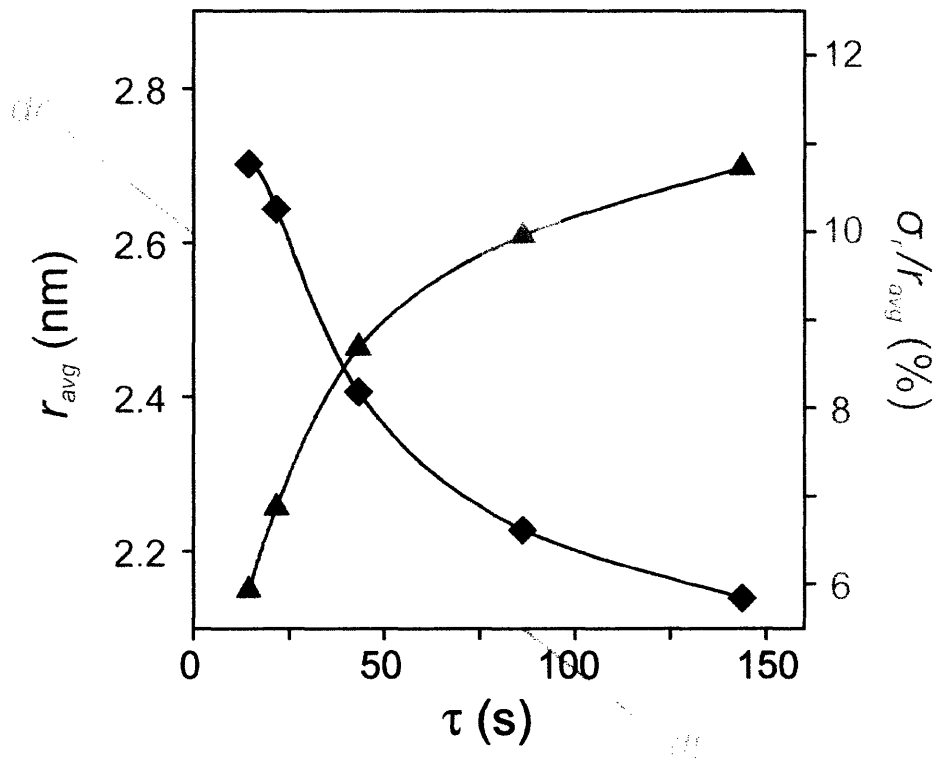


**Figure 3.7:** Method of estimating the RTD contribution to the overall NC size distribution.

### 3.3 Single and Two Phase Flow

As stated in the previous chapter and more fully developed in this chapter, mass transfer effects place a fundamental limit on the utility of single-phase reactors for particle synthesis. The slow diffusive mixing for single-phase flow was avoided by placing a small convective mixer in-line with the flow. However, some NC chemistries (eg. PbSe NCs) occur very rapidly even at room temperature, and premixing the precursors in this manner would cause reaction and nucleation prior to the heated entrance, leading to irreproducibility and poor size distributions. Secondly, the influence of axial dispersion, which is more pronounced at short times, places a limit on the range of reaction times which can be studied using single-phase flow. A method for overcoming both of these limitations is to perform reactions in a gas-liquid segmented flow regime. Compared to the single-phase case, a segmented flow simultaneously increases mixing and reduces the dispersion in residence times. The details and implementation of such two phase flow designs will be discussed in the following chapters.

### 3.4 References

1. Bird, B. B.; Stewart, W. E.; Lightfoot, E. N., *Transport Phenomena*; 2nd ed.; Wiley: New York, 2002.
2. Ebdian, M. A.; Dong, Z. F.; "Forced convection, internal flow in ducts." In *Handbook of Heat Transfer*; Rohsenow, W. M.; Hartnett, J. P.; Cho, Y. I., Eds.; McGraw-Hill: New York, 1998.
3. Shah, R. K.; Bhatti, M. S.; "Laminar convective heat transfer in ducts." In *Handbook of Single-Phase Convective Heat Transfer*; Kakaç, S.; Shah, R. K.; Aung, W., Eds.; Wiley: New York, 1987.
4. Sellars, J. R.; Tribus, M.; Klein, J. S.; "Heat transfer to laminar flow in a round tube or flat conduit – the Graetz problem extended." *Transactions of the ASME* **1956**, *78*, 441-448.

5. Jamieson, D. T.; Irving, J. B.; Tudhope, J. S., *Liquid Thermal Conductivity, a Data Survey to 1973*; National Engineering Laboratory and Her Majesty's Stationery Office: Edinburgh, 1975.
6. Vargaftik, N. B.; Filippov, L. P.; Tarzimanov, A. A.; Totskii, E. E., *Handbook of Thermal Conductivity of Liquids and Gases*; CRC Press: Ann Arbor, 1994.
7. Yaws, C. L. *Yaws' Handbook of Thermodynamic and Physical Properties of Chemical Compounds (Electronic Edition)*; Knovel: Norwich, NY, 2003. This is an electronic compilation of several handbooks and references on properties of compounds. Available at <http://www.knovel.com/knovel2/Toc.jsp?BookID=667&VerticalID=0>.
8. Atkins, P. A., *Physical Chemistry*; 5th ed.; W. H. Freeman and Company: New York, 1994.
9. Krahn, U. G.; Luft, G.; "Viscosity of several liquid hydrocarbons in the temperature range 298-453 K at pressures up to 200 MPa." *Journal of Chemical & Engineering Data* **1994**, *39*, 670-672.
10. Fogler, H. S., *Elements of Chemical Reaction Engineering*; 4th ed.; Prentice Hall: New York, 2006.
11. Levenspiel, O., *Chemical Reaction Engineering*; 3rd ed.; Wiley: New York, 1998.
12. Levenspiel, O.; Smith, W. K.; "Notes on the diffusion-type model for the longitudinal mixing of fluids in flow." *Chemical Engineering Science* **1957**, *6*, 227-233.
13. Taylor, G.; "Dispersion of soluble matter in solvent flowing slowly through a tube." *Proceedings of the Royal Society of London A* **1953**, *219*, 186-203.
14. Aris, R.; "On the dispersion of a solute in a fluid flowing through a tube." *Proceedings of the Royal Society of London A* **1956**, *235*, 67-77.
15. Ananthkrishnan, V.; Gill, W. N.; Barduhn, A. J.; "Laminar dispersion in capillaries: Part I. Mathematical analysis." *AIChE Journal* **1965**, *11*, 1063-1072.



## Chapter 4

# Design, Fabrication, and Packaging of a Gas-Liquid Segmented Flow Microreactor

### 4.1 Introduction to Segmented Flow

Simple single-phase laminar flow reactors such as the one described in Chapter 2 suffer from slow diffusive mixing and broad residence time distributions, characteristics which are detrimental to the quality of NCs produced. Several strategies have been employed to improve the mixing and RTDs in liquid-phase microreactors. One method of reducing the reactor mixing time is to reduce the distance for diffusive mixing by splitting each feed stream into multiple streams and then interdigitating the sets of streams<sup>1,2</sup> (figure 4.1a). Mixing times as fast as tens of milliseconds have been achieved with this method. However, these single-phase designs still exhibit large extents of axial dispersion due to the nonuniform velocity profile across the channel. A second method of improving the mass transport characteristics involves inducing chaotic advection in a single-phase flow. In such a flow, velocity components normal to the wall are induced. As a result, material is transported between the sidewall and channel center, thereby reducing axial dispersion and improving mixing. These flows have been achieved by either fabricating a three-dimensional channel path<sup>3</sup> or by patterning the channel walls<sup>4,5</sup> (figure 4.1b).

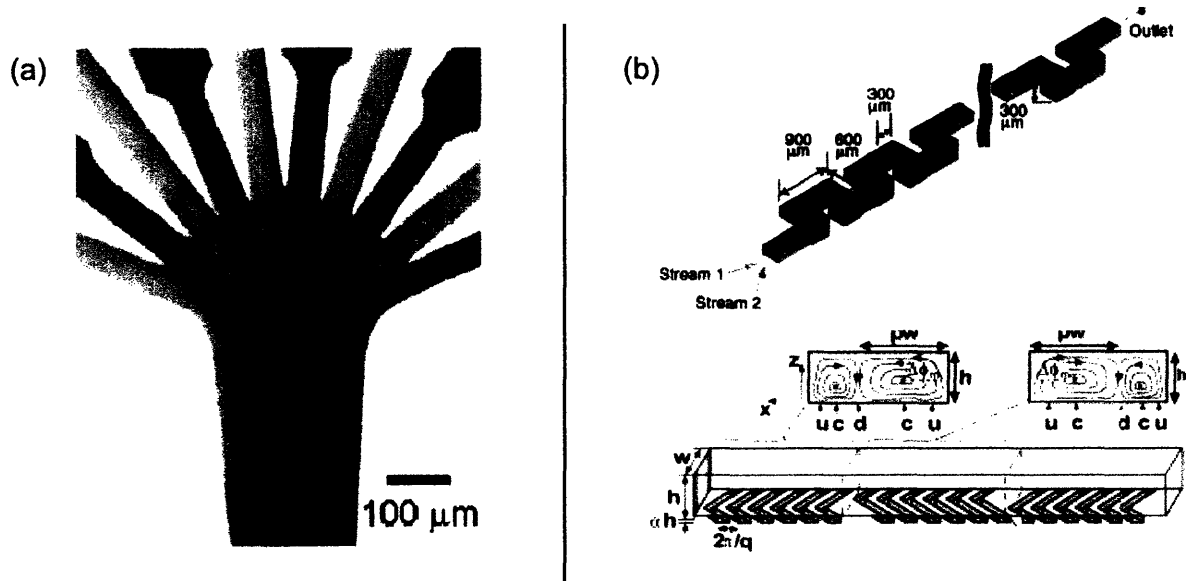


**Figure 4.1:** Previously employed strategies for improving liquid mixing in laminar flow in microchannels. (a) Reducing diffusion distance by interleaving streams of two different solutions.<sup>2</sup> (b) Introducing chaotic advection by either fabricating a three-dimensional flow path (top)<sup>3</sup> or patterning the channel walls (bottom).<sup>4</sup>

A superior method for improving reactor mass transport characteristics is to use a segmented two-phase flow rather than single-phase flow. This is accomplished by introducing an immiscible liquid or gas into the reactant flow. Such a flow consists of alternating slugs of liquid and gas (or immiscible liquid). Similar to the principle shown in figure 4.1b, recirculatory motion within the fluid slugs exchanges material between the wall and center of the channel.<sup>6</sup> In this way, mixing is greatly enhanced and axial dispersion reduced in comparison to single-phase flow. Figure 4.2 shows the liquid velocity field and streamlines for a gas-liquid flow in two types of microfluidic channels fabricated from polydimethyl siloxane (PDMS).<sup>7</sup> The average velocity has been subtracted out in the figure to emphasize the recirculation in the liquid slugs. The segmented flow approach has two main advantages over the chaotic advection in single-phase flow shown in figure 4.1b. First, the excellent mixing characteristics can be maintained over a wide range of flow conditions (reaction times) by independently varying the gas and liquid flow rates. In contrast, a patterned channel or specialized channel geometry is restricted to a relatively narrow range of optimal flow rates. Accessing a different reaction timescale would require fabrication of a new device with modified channel geometry. The second advantage is that for a comparable residence time and channel cross section, the recirculatory motion induced by segmentation is much more vigorous than that induced by specialized channel geometries in single-phase flow. In other words, much shorter mixing times and narrower RTDs can be achieved using segmented flow (discussed below).

The streamline patterns shown in figure 4.2 highlight a principle of practical importance to channel design. In a straight channel, the symmetry of the flow streamlines in each slug is

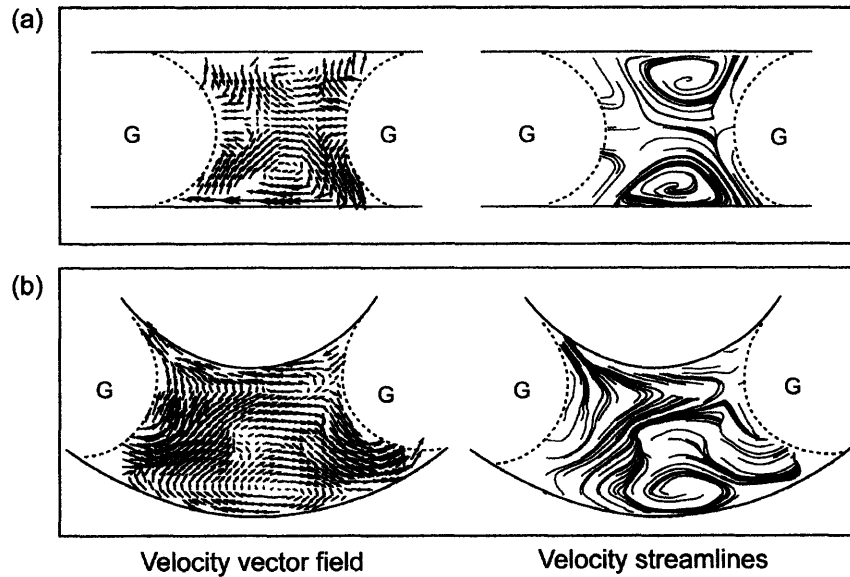


**Figure 4.2:** Liquid velocity vectors and streamlines in gas-liquid segmented flow obtained by particle imaging velocimetry. (a) straight channel and (b) curved channel geometries are shown. The width of the channel is  $400\mu\text{m}$ , and G = gas in the figure. Adapted from reference 7.

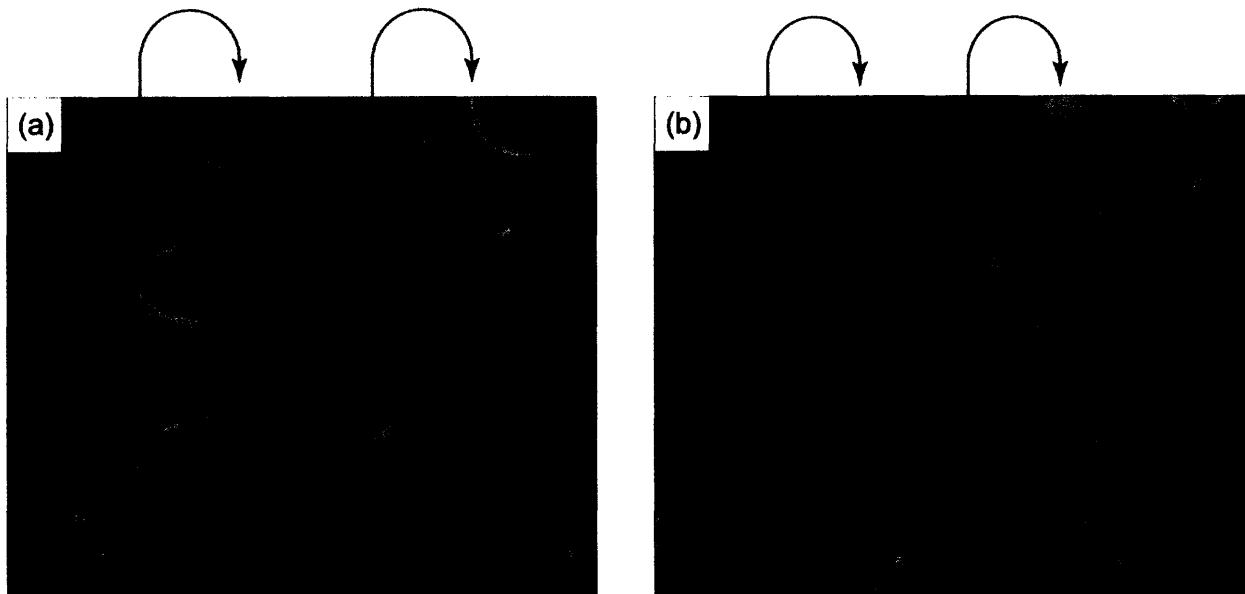


**Figure 4.3:** Fluorescence images of flows in a microchannel ( $d_h = 400\mu\text{m}$ ) fabricated from silicon. A hexane stream under (a) single-phase or (b) gas-liquid segmented flow conditions is present in the long meandering channel. A fluorescent solution is continuously introduced into the stream at several positions (bottom).

such that there is little to no mixing across the centerline (figure 4.2a). By introducing periodic bends in the channel wall, efficient fluid exchange across the center can be accomplished (figure 4.2b), and this has been shown in both gas-liquid<sup>7</sup> and liquid-liquid<sup>8</sup> segmented flow. The combination of segmented flow and a periodic modulation of the channel path results in both rapid mixing and a uniform concentration distribution across the entire channel cross-section. This is shown in figure 4.3. Fluorescence images of a meandering microfluidic channel are shown under different flow regimes. A fluorescently doped liquid stream is continually introduced at multiple positions along one side of the main channel. During liquid phase operation of the main channel (figure 4.3a), most of the injected solution remains on one half of the channel since mixing is limited by diffusion. When the main channel is operated under gas-liquid segmented flow conditions (figure 4.3b), the fluorescent solution is rapidly mixed and uniformly distributed across the entire channel width.

Quantitatively, the difference in mixing performance between segmented flow and single-phase chaotic advection is shown in figure 4.4. The channel length required to achieve 90% of complete mixing of two miscible liquids is used as the figure of merit. This value is normalized to channel width to facilitate comparison between different reactor designs. In the figure, the mixing length is plotted against various flow conditions (Péclet number). The shortest mixing lengths (i.e. fastest mixing) were achieved using gas-liquid and liquid-liquid segmented flow designs. With these designs, mixing can be achieved within ~10 channel diameters, which is several times shorter than mixing lengths reported in designs based on single-phase chaotic advection.

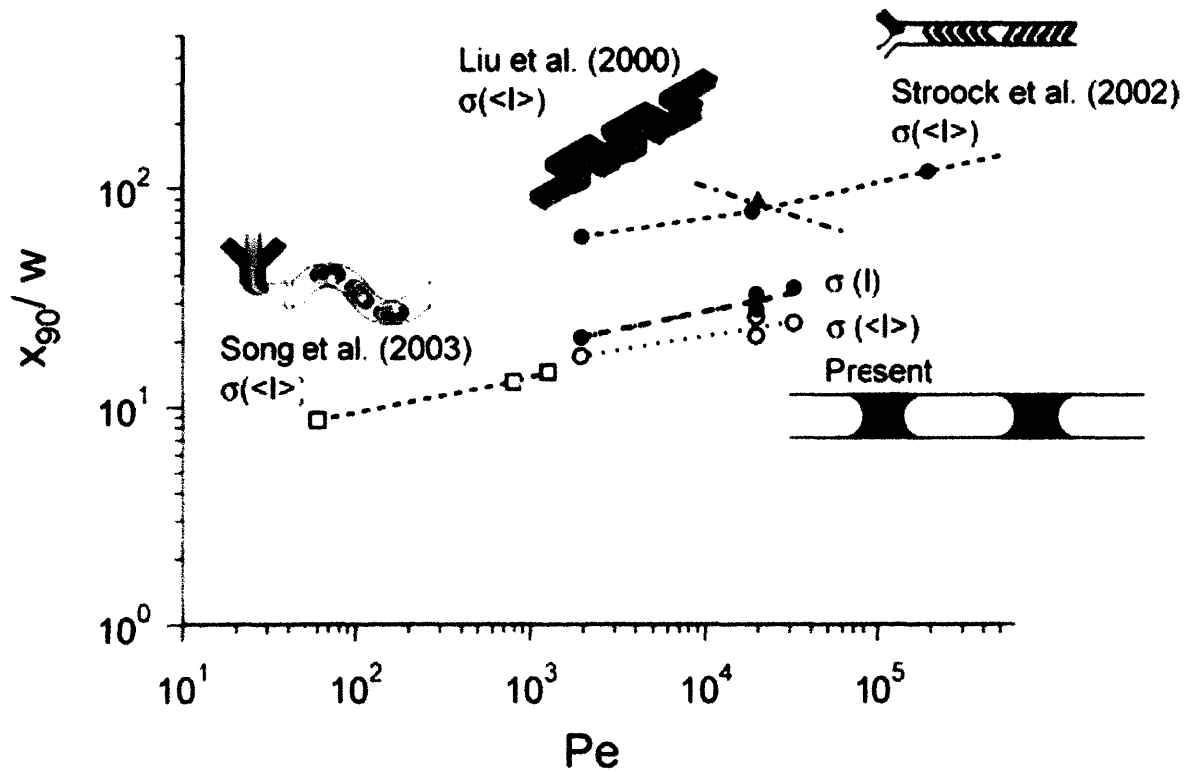


**Figure 4.4:** Comparison of mixing efficiency for gas-liquid segmented flow, liquid-liquid segmented flow, and single-phase chaotic advection (the latter is shown in figure 4.1b). The figure of merit used is the channel length required to achieve an extent of mixing of 90% normalized to the channel width.  $Pe$  is the Péclet number. From reference 7.

In addition to superior mixing, the effective fluid transfer between the channel wall and center achievable using segmented flow also translates to narrower residence time distributions. The low dispersion in segmented flow is shown in the experimentally measured curves shown in figure 4.5. The  $E$ -curve for a tracer pulse was measured within a PDMS microchannel under both single-phase and two-phase flow conditions. The average residence time is approximately the same for the two curves in the figure. Introduction of gas segmentation dramatically improves the dispersion within the channel. As stressed in the previous chapters, the influence of the RTD on the NC size distribution is significant. In contrast to the single-phase flow design described in Chapter 2, a segmented flow approach exchanges NCs across the channel and should result in narrower size distributions. This effect is illustrated schematically in figure 4.6. Improving size distributions with segmented flow has been demonstrated for sol-gel particles produced in both macroscale<sup>9</sup> and microfluidic<sup>10</sup> continuous flow reactors.

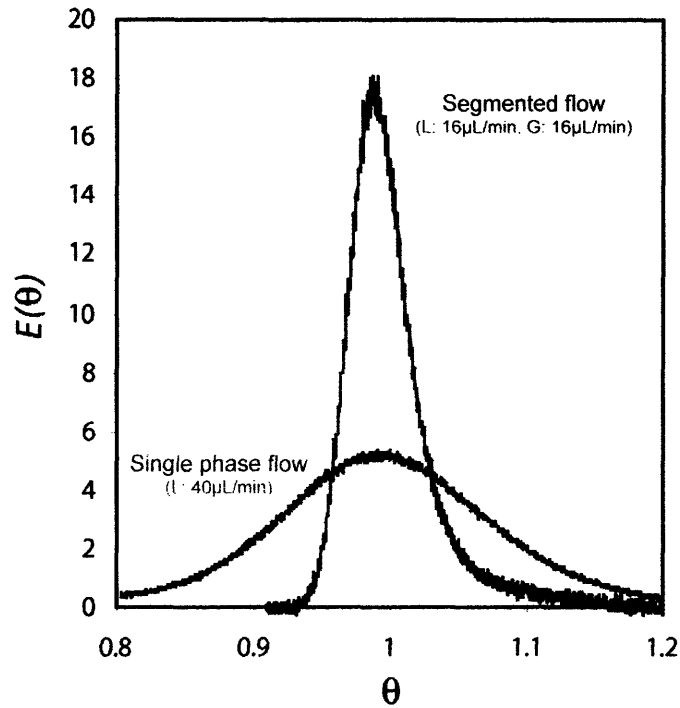


**Figure 4.5:** Experimentally measured  $E$ -curve for single-phase and gas-liquid segmented flow in a microchannel ( $d_h \sim 250\mu\text{m}$ ). The residence times for the two cases are approximately equal. Figure courtesy of A. Günther and M. Kreutzer.

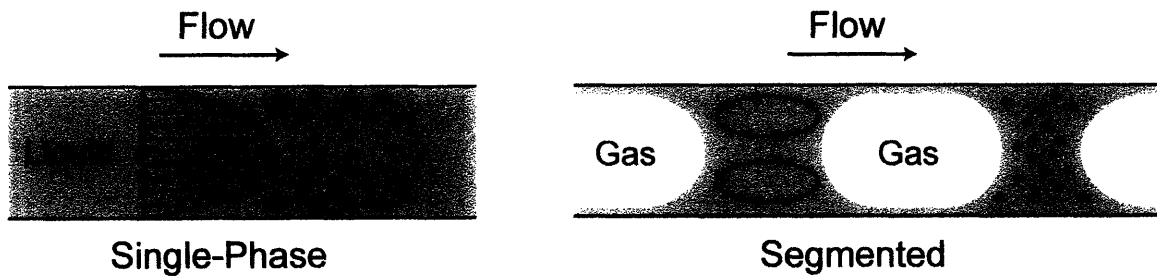


**Figure 4.6:** Schematic illustrating effect of mixing and axial dispersion on size distribution. In the single-phase laminar flow, diffusion is the only means of mixing. Also, because of the parabolic fluid velocity profile, particles near the wall to spend more time in the reactor than those in the center, resulting in broad RTDs. In the two-phase case, recirculation within each liquid slug brings material from the wall to the center of the channel, enhancing mixing, narrowing the RTD, and resulting in narrower size distributions.



## 4.2 Reactor Design Considerations

This section highlights the numerous design parameters involved in applying microscale segmented flow to NC synthesis. To begin with, gas-liquid rather than liquid-liquid segmented flow offers the most versatility in terms of the range of chemistries that can be performed in a microfluidic system. Increasing miscibility of most solvents with temperature implies that gas-liquid flow is preferable for performing reactions at elevated temperatures. Moreover, it is possible to achieve uniform segmentation in gas-liquid flows over a very large range (over two orders of magnitude) of bubble velocities and therefore reaction timescales.<sup>7,11</sup> Liquid-liquid segmented flow systems are operated over a much narrower range with typical droplet velocities varying over an order of magnitude.<sup>8</sup> Finally, in gas-liquid segmented flow, the reaction solution exists as a continuous liquid phase within the channel (figure 4.6) so that it is possible to inject additional reactants or withdraw reaction aliquots in a continuous, controllable manner. In liquid-liquid segmented flow, the reaction solution is usually the dispersed (droplet) phase, so that subsequent reactant addition is challenging because it requires synchronized merging of discrete droplets,<sup>12</sup> and withdrawing small aliquots is difficult without disturbing the flow.

Gas-liquid segmentation is very sensitive to the inlet geometry as well as any large changes in fluid properties. For instance, temperature-induced changes in viscosity and surface tension can severely destabilize the segmentation, resulting in long, nonuniform segments. Therefore, the gas must be introduced at the reaction conditions rather than further upstream before the fluid reaches the heated section of the device. A reactor based on capillaries and standard fluidic fittings cannot meet these requirements. On the other hand, microfabricated device can be designed such that segmentation is initiated on-chip at a well-defined inlet geometry. The temperature and solvent compatibility requirement means that the reactor must

be fabricated from silicon or glass rather than through soft lithography of polymers (eg. PDMS). Silicon is a particularly attractive material choice since well-established fabrication methods developed for microelectronics can be used.

A unique feature of the NC chemistry poses a design challenge in terms of quenching the reaction. Rapid dilution of the reaction mixture will not arrest the growth process since the NCs can still undergo Ostwald ripening at sufficiently high temperatures. Effective quenching of the reaction can only be accomplished by bringing the temperature below  $\sim 100^{\circ}\text{C}$ , and this thermal quenching must be accomplished on-chip. Otherwise, the solution will continue to react after leaving the device within the tubing and packaging regions of the system since these regions contain a significant volume relative to that of the channel. Maintaining a  $\sim 200^{\circ}\text{C}$  gradient on a single device is a challenge and requires some care during the design stage. Since the thermal conductivity of silicon is fairly high, it is useful to estimate the length required to maintain such a large temperature gradient. Figure 4.7 shows the results of a finite-element calculation (FEMLAB) for the temperature profile on a silicon-glass slab with two constant-temperature boundary condition blocks. The calculation shows that at least  $\sim 8\text{mm}$  of space should be placed between the heated and cooled sections of the device in order to maintain the required temperature gradient.

Such a large thermal gradient may introduce considerable mechanical stresses within the reactor chip. Stresses tend to concentrate near sharp corners so the region separating two temperature zones in the reactor should be designed to minimize the occurrence of such features. An estimate of the stress field in the device was calculated using a 2-D finite element (FEMLAB). Figure 4.8 shows the result of the calculation for two silicon-based geometries.

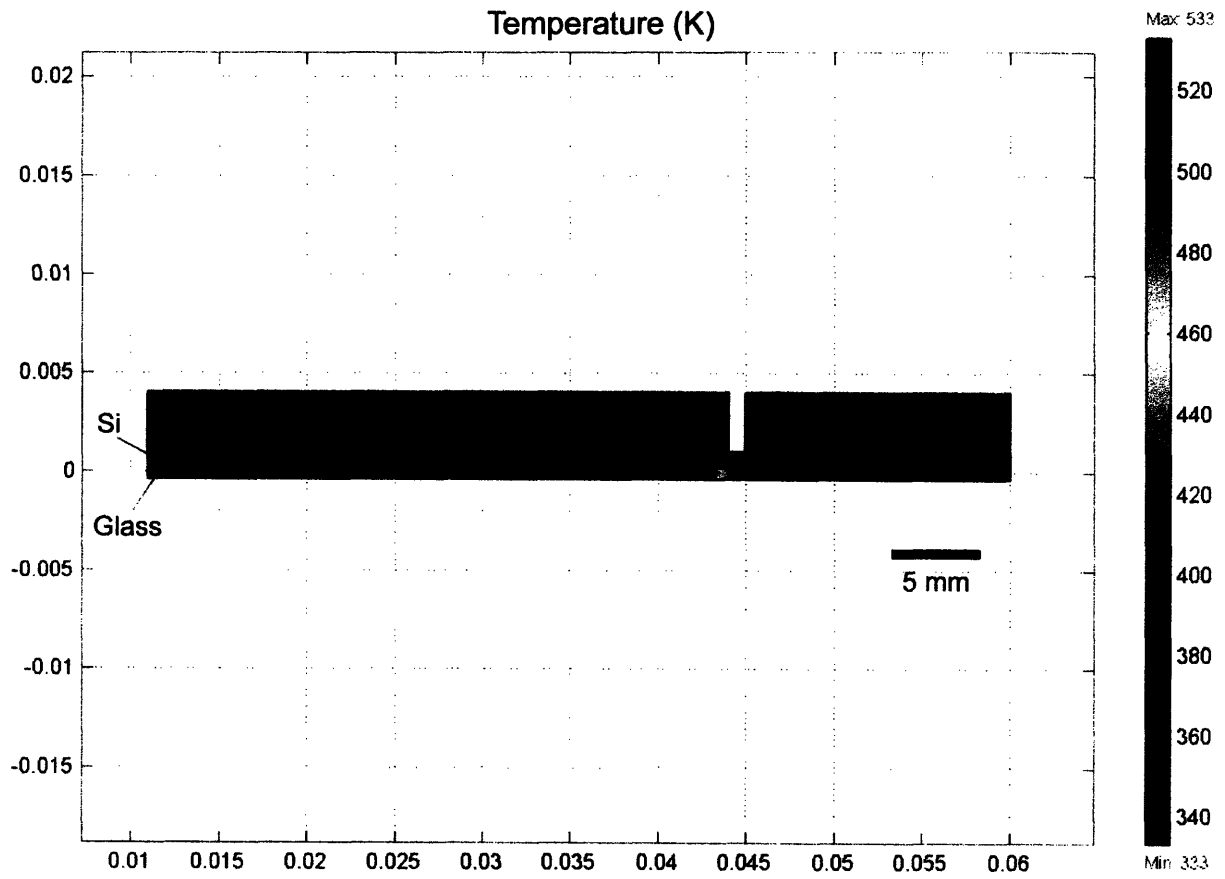


**Figure 4.7:** Calculated temperature profile for a silicon-glass slab. Temperature scale is in Kelvin. Constant temperature boundary conditions are imposed on the two larger blocks. The temperature of the two blocks differ by 200°C.

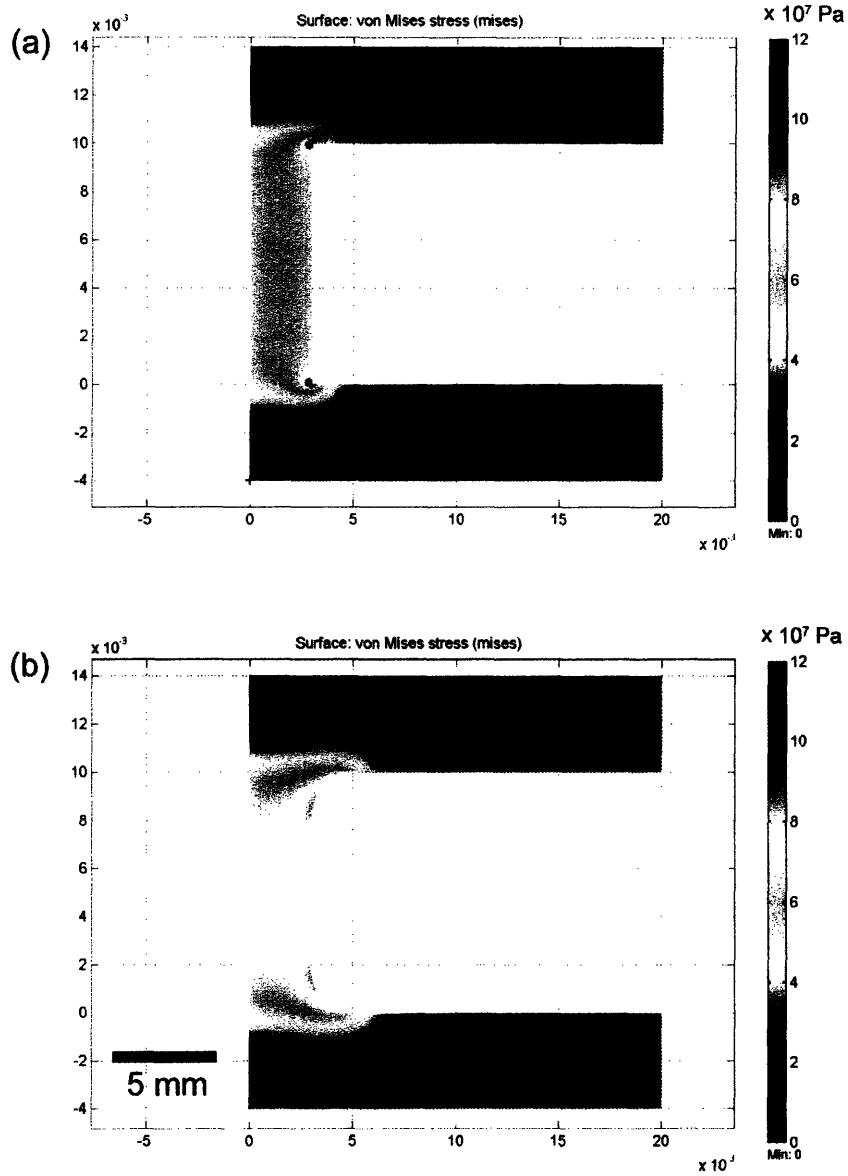


**Figure 4.8:** Calculated stress field in silicon for region separating the two temperature zones. (a) Sharp and (b) rounded device geometries are shown. For each figure, the top portion is cold and the bottom portion is the hot region (though by symmetry the magnitude of the stress is independent of the polarity of the temperature gradient). Based on the thermal expansion coefficient of silicon and a 200°C temperature difference, a total displacement of 30 $\mu$ m in vertical direction was imposed on one side, and the resulting Von Mises stress (Pa) field was calculated.

The choice of the dimensions and U-shaped design separating the two temperature regions will become apparent in the next section. For dimensions shown in the figure, a temperature difference of 200°C in silicon corresponds to a total expansion difference of 30µm in the vertical direction. From this value and suitable boundary conditions, the stress field was determined. For complicated geometries, it is useful to calculate an effective stress magnitude (a scalar quantity), rather than the components of the overall stress tensor. This quantity, called the von Mises stress, is given by:<sup>13</sup>

$$\sigma_v = \sqrt{\frac{1}{2}[(\sigma_1 - \sigma_2)^2 + (\sigma_1 - \sigma_3)^2 + (\sigma_2 - \sigma_3)^2]} \quad \text{Eq. 4.1}$$

where  $\sigma_i$  are the principle stresses. In two dimensions,  $\sigma_3 = 0$  so the von Mises stress is given by:

$$\sigma_v = \sigma_1^2 - \sigma_1\sigma_2 + \sigma_2^2 \quad \text{Eq. 4.2}$$

Empirically, it has been shown that failure occurs once the von Mises stress is larger than the tensile strength of the material. It is clear from figure 4.8 that eliminating sharp corners in the region between temperature sections greatly reduces thermally induced stresses on the device. The tensile strength of silicon has been reported to be anywhere between  $3 \times 10^9$  and  $7 \times 10^9$  Pa, which is more than an order of magnitude larger than the maximum stress in even the sharp-cornered design (figure 4.8a). Thus, the more conservative design shown in figure 4.8b should provide a large margin of safety during regular operating conditions.

### 4.3 Incorporating the Design Criteria

The considerations described in the previous section were incorporated into the segmented flow reactor design shown in figure 4.9. The reactor consists of a 1-m long reaction channel with  $400 \times 400\mu\text{m}$  cross-sectional dimensions. Shallow side channels (40µm deep) at

two different streamwise positions are also available for drawing out reaction aliquots. The long length of the channel was chosen so that suitably long reaction times could be studied (up to ~10 min.) under flow conditions amenable to uniform segmented flow (tens of  $\mu\text{L}$ 's per minute). Shorter reaction times are quite compatible with such devices since the segment uniformity usually improves with increasing flow rate. Two temperature regions are maintained on the chip, a heated reaction section and a cooled quench section. Liquid precursors are delivered separately into two inlets at the bottom of the diagram. An inert gas stream is then introduced further downstream to initiate segmented flow. Nucleation and growth of NCs proceeds as the precursors flow through the long heated section. The reaction is rapidly quenched once the fluid reaches the cooled outlet region at the top of the figure.

The main reaction channel is divided into two sections, a short meandering portion (near the inlets) and a much longer straight portion where the majority of the NC growth occurs. The meandering geometry near inlets in figure 4.9 was implemented to make sure that as the precursors enter the device they are evenly mixed across the entire channel. The performance data in figure 4.4 provide guidance in designing this section of the chip. From the figure, the mixing length for the segmented flow designs was ~10 channel diameters, and the meandering section shown in figure 4.9 was made to be somewhat longer than this value. Importantly, the mixing length shown in figure 4.4 is approximately constant, being only weakly dependent on flow rate (Péclet number). Thus, the length of the meandering section should be sufficient over a realistic range of flow rates and reaction times.

The design of the region between the two temperature zones was based on the results shown in figure 4.8. The rounded through-etch feature was chosen to minimize concentrated

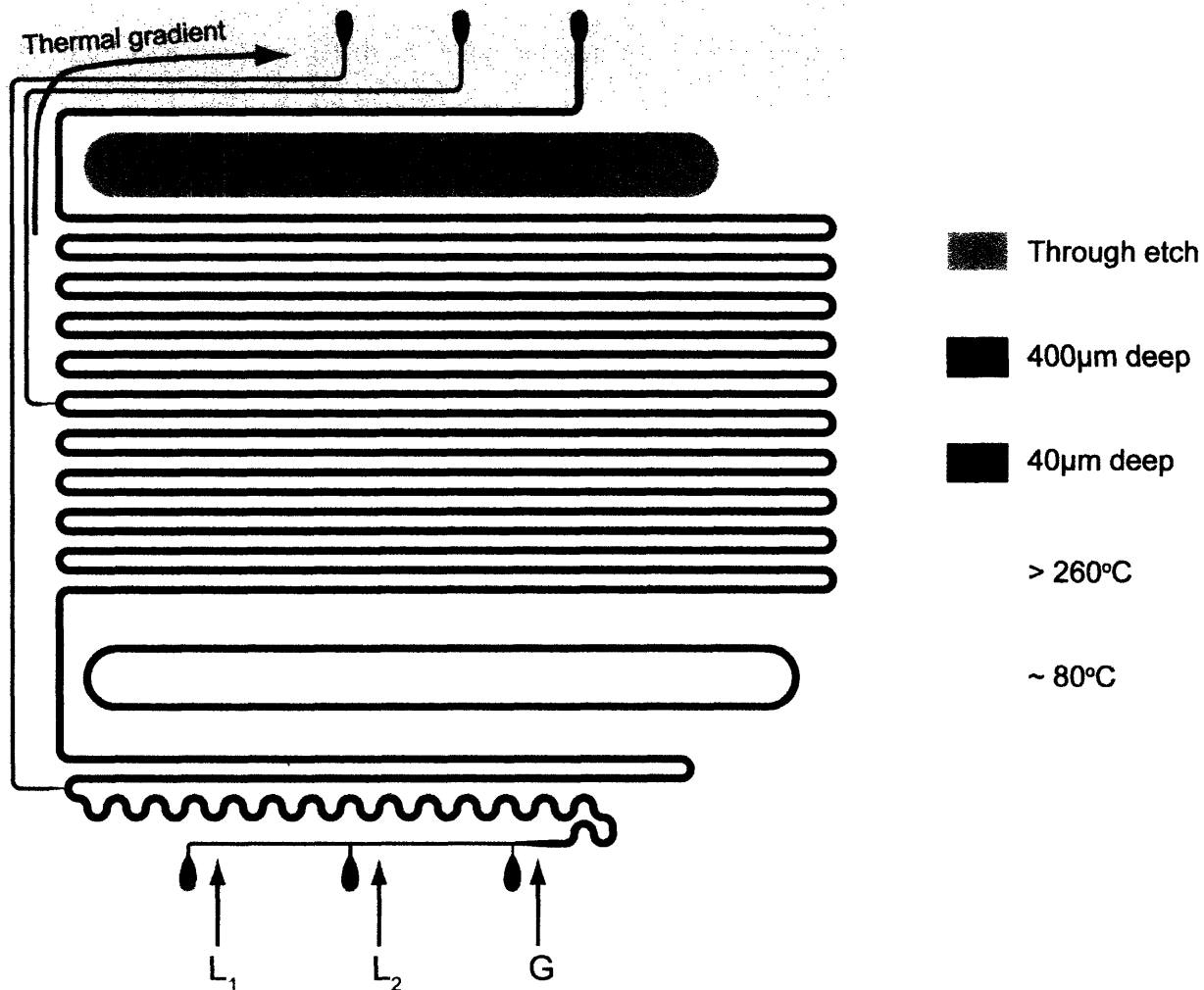


**Figure 4.9:** Gas-liquid segmented flow microreactor design. The main channel (black) is 1 m long and 400 μm wide. The entire device area is  $\sim 5 \times 5$  cm. Precursor solutions and segmenting gas enter at the bottom of the diagram and flow through the long heated section. The halo etch region (gray) keeps the two regions on the device thermally isolated. The path of the temperature gradient is shown by the red arrow.

stresses at corners. This gap is necessary to eliminate direct heat transfer between the two temperature zones. The heat transfer is forced to take a much longer path between the heated section and reactor outlets as indicated by the arrow in the diagram. In this way, it is possible to both minimize the overall device footprint and accommodate the distance necessary (greater than ~8 mm) to maintain the large temperature gradient.

## **4.4 Wafer Fabrication**

### **4.4.1 Process Summary**

The segmented flow reactor was fabricated from silicon wafers using conventional micromachining methods. The process first involves etching inlet holes and the halo pattern (for isolating the two temperature zones) from the back side of the wafer to a depth of ~350 $\mu\text{m}$ . The reactor channel pattern, which is aligned with the inlet and halo underneath, is then etched from the front side of the wafer to the desired channel depth. A nested mask of patterned oxide under patterned photoresist is used so that two different channel depths are possible, ~400 $\mu\text{m}$  for the main channel and ~40 $\mu\text{m}$  for the side channels. During the front side etch, the inlet and halo patterns become connected to the back side pattern (through etch). Finally, the entire device is passivated with a layer of thermal oxide and the channels side is sealed with an anodically bonded pyrex wafer. Fluidic inlets are accessed from the back side. A summary of the required process steps is given below:

Photolithography, 3 layers  
Deep reactive ion etching (DRIE), 3 layers  
Thermal oxidation, 3 steps  
Pyrex-to-silicon anodic bonding, wafer level  
Multiple wet etches and resist removal steps



The details of the process flow are given in the next section and shown in figure 4.10. The pattern shown in the figure is for illustrative purposes only. The actual mask patterns used are shown in figure 4.9.

#### **4.4.2 Detailed Process Flow**

The process begins with growth of 0.5 $\mu\text{m}$  oxide layer on a RCA-cleaned silicon wafer (6-in. diameter, 650 $\mu\text{m}$  thick) and patterning of the back side features. In general, four devices could be patterned on each wafer. A 10 $\mu\text{m}$  layer of positive photoresist (AZ9620, Clariant) was spin-coated on the back side of the wafer and then soft-baked at 95°C. The photoresist layer is exposed using a mask for the inlet holes and halo feature. The pattern was developed and the wafers hard-baked at 95°C. The front side of the wafer was protected with a layer of photoresist before the wafers were subjected to a wet oxide etch with a buffered hydrofluoric acid solution (BOE). The inlets and halo feature, now exposed due to the BOE solution, were then etched to a depth of 350-360 $\mu\text{m}$  using DRIE. Next, the photoresist was removed using a piranha solution (sulfuric acid and hydrogen peroxide), followed by complete removal of the oxide layer with BOE. A fresh 1.0 $\mu\text{m}$  thick oxide was then grown on the wafers in preparation for front side processing. A 1 $\mu\text{m}$  layer of photoresist (OCG825, Shipley) was spin-coated on the front side of the wafers and soft-baked at 120°C. The photoresist was exposed, developed, and hard-baked using the shallow side channel pattern. Next, the back sides of the wafers were protected with a layer of photoresist before the side channel layer was etched using BOE. The photoresist was removed with piranha, leaving wafers patterned in the oxide layer. Next, a 10 $\mu\text{m}$  layer of photoresist was spin-coated on the front sides of the wafer. The main channel layer was aligned and patterned on this using the same exposure, development, and oxide etch as before.

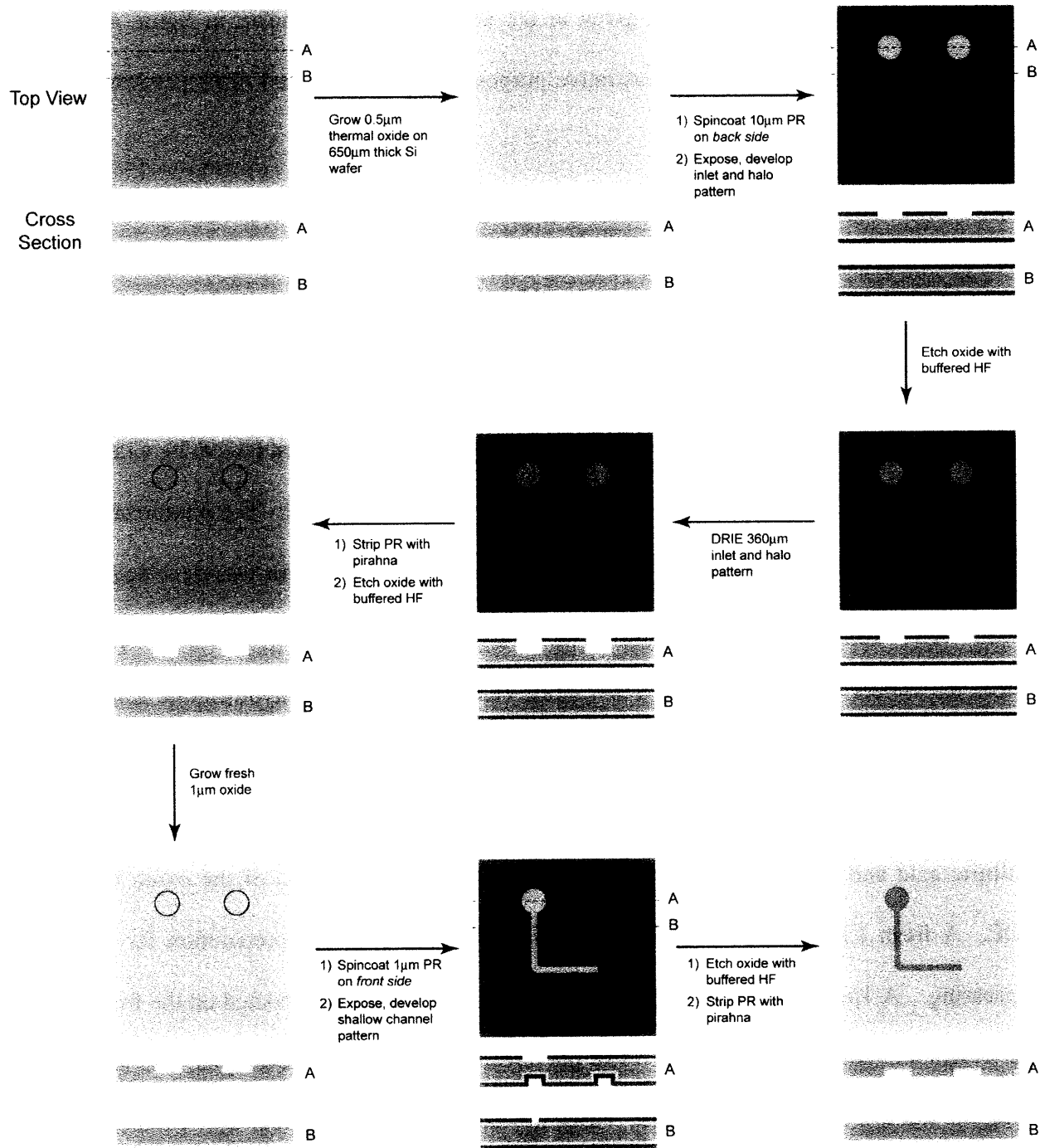
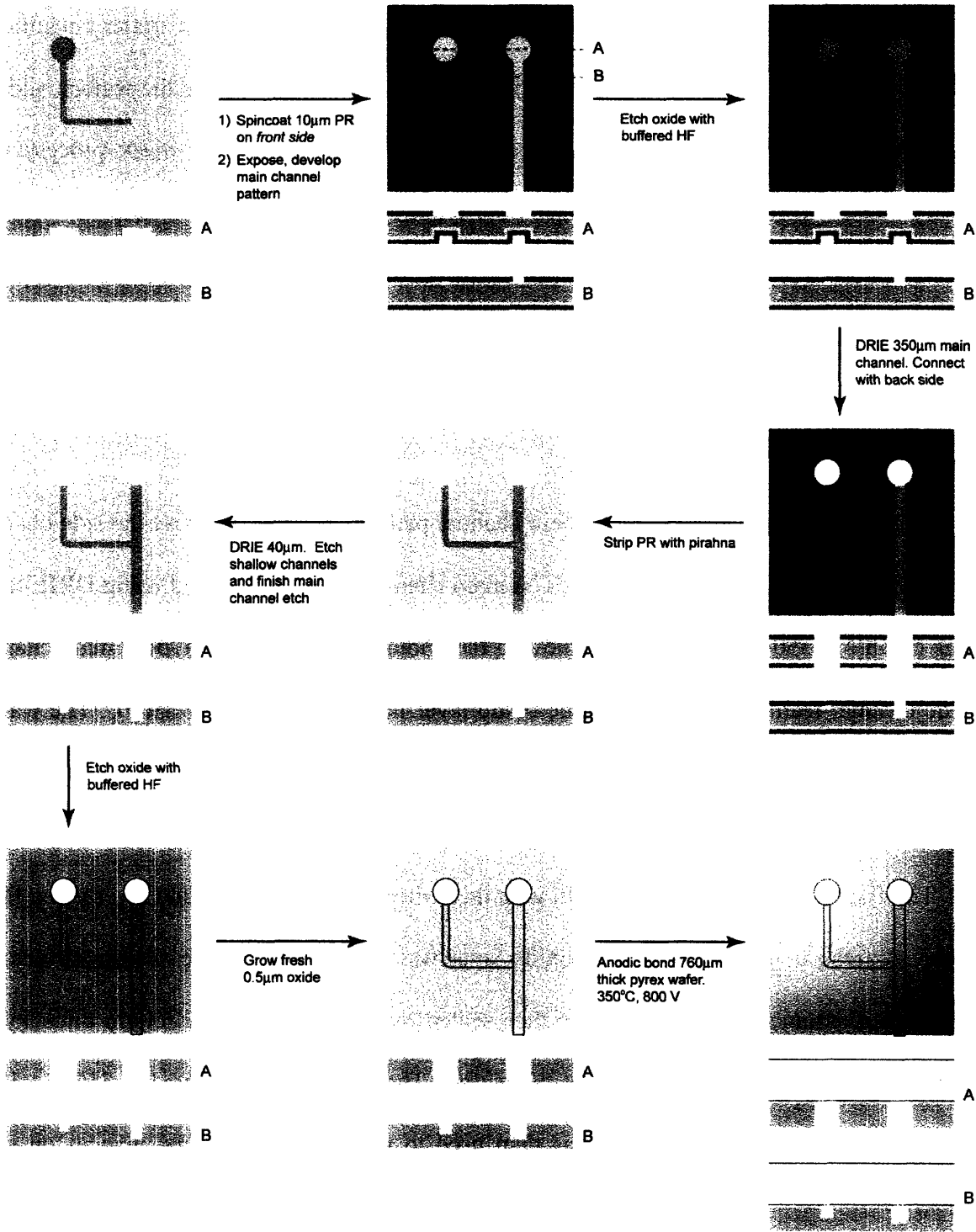


**Figure 4.10:** Wafer process flow. The actual design that was fabricated is shown in figure 4.9.



DRIE = Deep reactive ion etch      PR = Photoresist

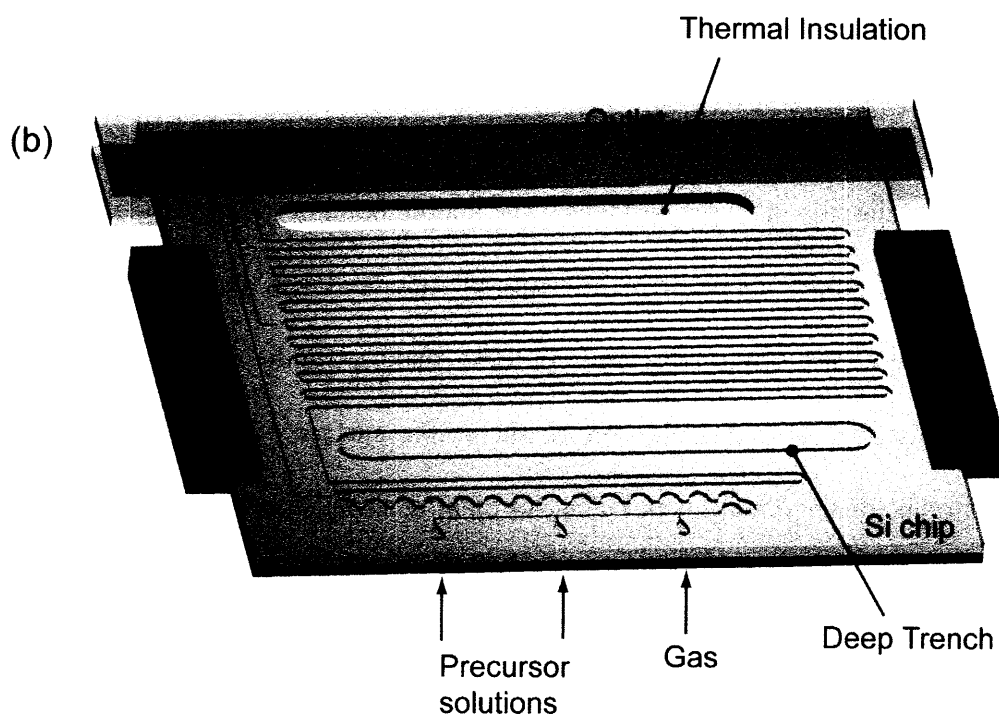
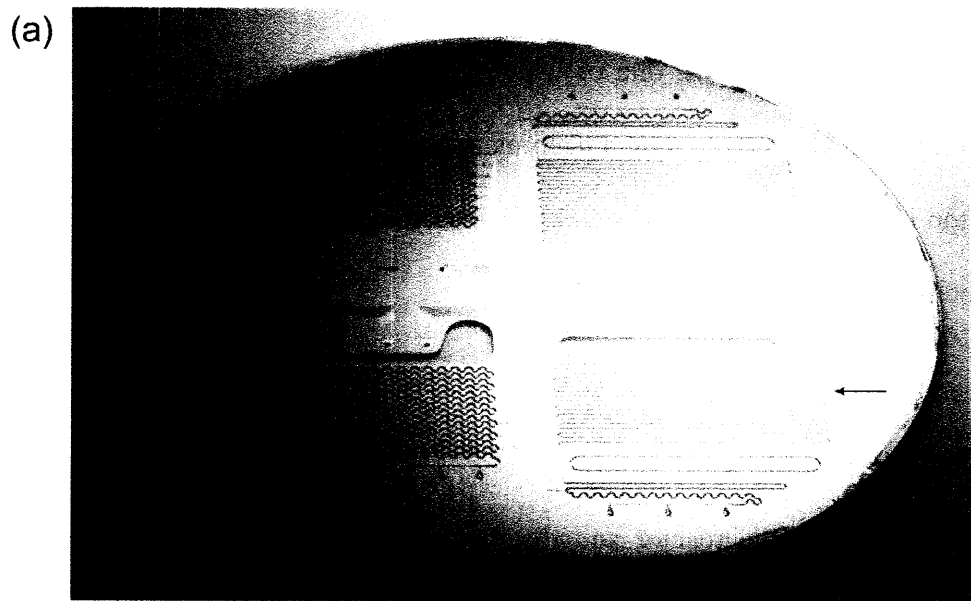
■ Silicon      ○ Silicon dioxide      ■ Thick PR      ■ Thin PR

Figure 4.10 (cont'd): Wafer process flow. The actual design that was fabricated is shown in figure 4.9.

The previous series of photolithography steps on the front side of the wafer constitute a nested mask. The side channels were patterned directly in the oxide layer on the wafers, and the main channel were patterned in the photoresist layer above. A nested mask process was necessary since two different DRIE depths were required in the reactor – a deep etch for the main channel and a shallow etch for the side channels. Without a nested mask, DRIE would be performed for the two depths with intermediate photolithography steps. This would be problematic because it is difficult to deposit a uniform layer of photoresist on a surface containing deeply-etched features.

At this point in the process, the main channel pattern was exposed, and the side channel features were protected with photoresist. The main channel was then formed using DRIE to an average depth of  $\sim 350\text{-}360\mu\text{m}$ . Upon removing the photoresist with piranha, both main channel and side channel features are exposed (the oxide layer now acts as the etch stop). The wafers were then etched a final  $\sim 40\mu\text{m}$  etch with DRIE. Thus, the side channels were at this point  $\sim 40\mu\text{m}$  deep, and the main channel was  $\sim 400\mu\text{m}$  deep ( $360 + 40\mu\text{m}$ ).

The final steps in the process begin with the removal of the entire oxide layer using BOE solution. A fresh  $0.5\mu\text{m}$  thick thermal oxide layer was then grown on the silicon surface for chemical passivation. The channels were then sealed by anodic bonding a  $760\mu\text{m}$  thick Pyrex (Corning 7740) wafer to the front side of the wafer. The bond was performed at  $350^\circ\text{C}$  with a bonding voltage of  $800\text{V}$ . A diesaw was then used to release the individual devices on each wafer.



**Figure 4.11:** (a) Photograph of the silicon wafer with a bonded pyrex top at the end of the process. (b) Three dimensional drawing of device indicated by the arrow in (a).

A representative wafer at the end of the process is shown in figure 4.11a. The wafer accommodated four reactor designs, one of which is the one described in section 4.3. A 3D rendered image of the reactor containing a deep main channel, two shallow side channels, and a bonded pyrex top is shown in figure 4.11b. Fluids enter the device through the inlet holes on the underside of the figure.

## 4.5 Packaging and Sealing

Interfacing between the reactor and the external fluid delivery system is particularly challenging due to the high temperatures and organic solvents present during device operation. The standard tubing and fittings (eg. HPLC components), which are used to deliver the fluid streams, are both quite resistant to a variety of chemicals at room temperature and hermetic up to high pressures. The reactor chip itself is also very chemically compatible since the fluids will only contact silicon dioxide or Pyrex surfaces. The anodic bond between the glass and silicon is extremely strong and poses no problem in terms of maintaining a seal at high temperatures. However, due to the nature of the fabrication process, making fluidic connections to the reactor is restricted to interfacing with holes on a flat wafer surface. Unlike standard threaded compression fittings, this geometry is not ideal for making a robust, hermetic seal. The difficulty is exacerbated by the fact that the packaging will be in constant contact with a stream of NC reaction solution at high temperatures (up to 300°C).

Common sealing methods for microfluidic devices usually involve either using a polymer-based adhesive (eg. epoxies) or making a compression seal with an elastomeric gasket. Unfortunately, these methods are incompatible with the operating requirements of the NC microreactor. A sealing method which can withstand the aggressive conditions of the NC

synthesis is based on glass brazing. Glass braze (or solder) materials are chemically inert, maintain a seal at high temperatures, and can form an extremely strong bond to metal oxides, glasses, and ceramics. However, glass brazing possesses some undesirable properties such as high sealing temperatures, mechanical brittleness, and irreversibility of the brazed joint. A fair amount of optimization and compromise must be made with respect to joint design and material choice.

In terms of joint design, direct brazing of tubing to the flat device surface is undesirable for a number of reasons. The resulting joint is extremely delicate, and mechanical strain on the tubing can easily lead to failure of the seal. Furthermore, alignment of the multiple tubes, glass braze, and inlet holes during the sealing process can be extremely challenging. Therefore, an improved joint design was implemented in which the tubing slides into a Pyrex (Corning 7740) interface plate bonded to the device inlet region (figure 4.12). The interface plate was fashioned by first ultrasonically drilling it with port holes (Ferro-Ceramic Grinding, Inc), each to a diameter large enough to accommodate standard 1/16-in. tubing. The piece was then aligned with the device inlet holes on a custom-built bonding chuck. The assembly was heated to  $\sim 300^{\circ}\text{C}$  in an oven, and the Pyrex was anodically bonded to the silicon at 1000V using an external power supply. Very thick Pyrex pieces could be bonded using such a method without any visible defects and strong adhesion. For instance, figure 4.13 shows a device bonded to a 1 cm thick pre-drilled Pyrex piece. The presence of the interface plate serves two purposes. First, it reduces mechanical strain on the tubing-braze joint especially during handling. Secondly, alignment of the tubing and braze material with the underlying inlet pattern is greatly simplified since it does not require the use of a specialized jig or chuck.

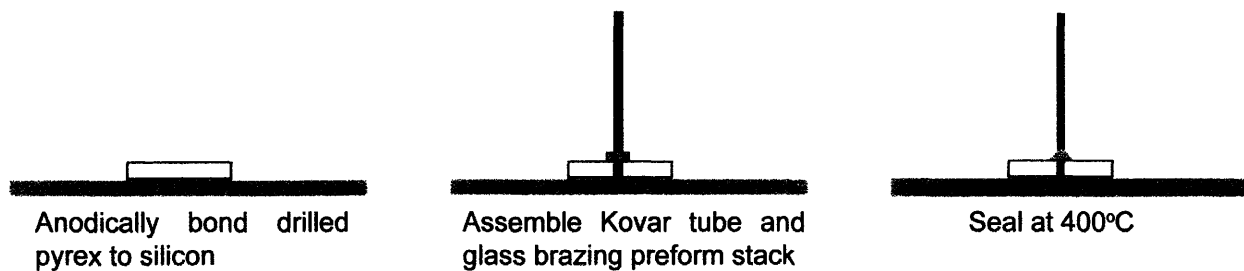


**Figure 4.12:** Glass brazing process for making fluidic seals.



**Figure 4.13:** A drilled Pyrex piece (1 cm thick) anodically bonded to a silicon microreactor.



The choice of materials for tubing and glass braze is a result of compromise between mechanical strength and thermal expansion mismatches. Since the sealing process must be performed at high temperature, differential expansion can result in large stresses at the joint and ultimately failure. Ideally, borosilicate glass (eg. Pyrex) tubing would be used as the fluid lines since the thermal expansion coefficient of this material class is very well matched to that of the underlying substrate. However, the thin tubing required is extremely delicate toward handling, a particularly undesirable quality since brazed joints are difficult to repair and practically irreversible. Therefore, low-expansion metal (eg. Kovar) was used instead for the tubing. This material has a reasonably low thermal expansion coefficient mismatch and its ductility imparts much more mechanical strength compared to glass tubing.

The choice of glass brazing material is similarly driven by a balance between several conflicting material properties. Figure 4.14 provides some guidance in choosing the appropriate braze material. The figure shows the thermal expansion curves of a glass braze and metal during the sealing process. At the sealing temperature (above  $T_{set}$  in the figure), the glass is soft enough for any residual stresses to be quickly dissipated. Once the system is cooled to  $T_{set}$ , the glass “sets up,” meaning that it hardens enough so that any stresses are not dissipated over a practical timescale. As the system is cooled to room temperature, differential thermal expansion between the different materials results in stresses which remain in the joint. Thus, the dashed line in the figure from the set point down to room temperature represents the thermal contraction trajectory of the glass as it cools, and the solid line represents contraction of the metal. The total strain in the final joint is the difference shown as  $\delta$  in the figure. Based on the principle illustrated in the figure, the ideal glass braze would have both a low coefficient of thermal expansion (matched

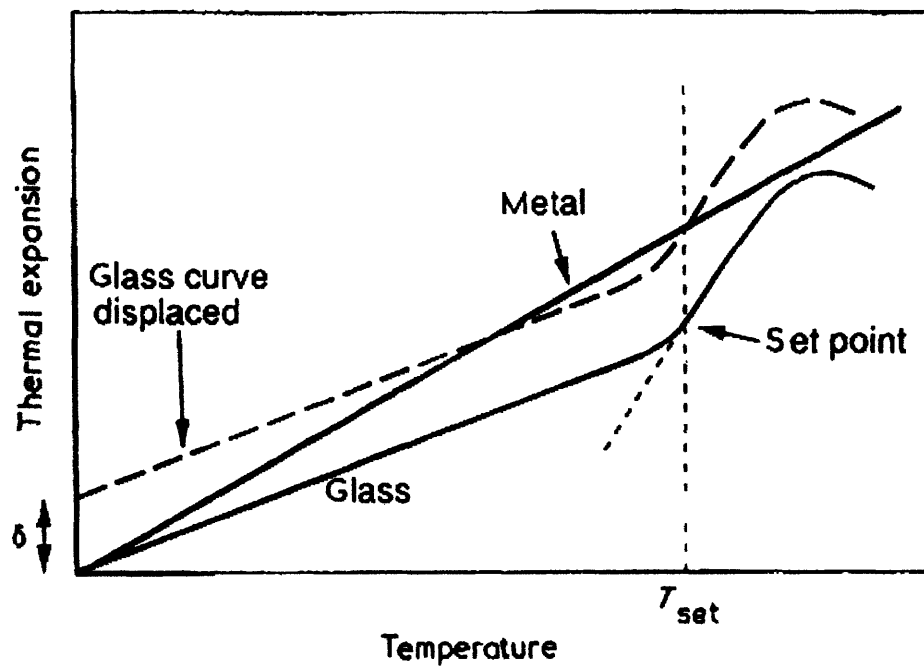


**Figure 4.14:** Thermal expansion curves used to estimate stress in a glass-metal seal. The quantity  $\delta$  is the total strain left in the joint after brazing. From reference 14.

with silicon/Pyrex) and the lowest possible sealing temperature so long as it is still above the reactor operating temperature. For most glasses, however, the required sealing temperature varies inversely with thermal expansion coefficient.<sup>14</sup> The potential strain-reducing benefit gained from choosing a glass with a low thermal expansion coefficient will often be more than offset by the high temperatures required for sealing. Also, typical sealing glasses vary greatly in terms of wetting and flow properties. A large number of glasses were tested for making the microreactor seals, and the one that represented the best compromise between all of these conflicting material parameters was Diemat 2760 (Diemat, Inc.). This brazing material produced the most reproducible and robust reactor packaging. The required sealing temperature, 400°C, is relatively low, and the thermal expansion mismatch at the joint was tolerable (Table 4.1).

**Table 4.1:** Thermal Expansion Coefficients at 20°C

<b>Material</b>	<b>Exp. Coef. (ppm / °C)</b>
Silicon	2.5
Pyrex	3.3
Kovar	5-6
Steel	11-19
DM2760 glass	7.5

Figure 4.15 shows the final reactor assembly including the anodically bonded interface plate and brazed Kovar tubes. The overall process can be reproducibly performed on multiple inlets as shown in the image with six simultaneously brazed connections.

Later reactor designs placed all of the inlet holes on the cooled side of the device so that the seals could be operated at relatively low temperatures (less than 100°C). In these cases, the packaging method was capable of maintaining good seals at pressures up to ~60 atm. Chapter 7 discusses the advantages of performing NC synthesis under high pressures.



**Figure 4.15:** Photographs of brazed fluidic connections.

## 4.6 References

1. Ehrfeld, W.; Golbig, K.; Hessel, V.; Löwe, H.; Richter, T.; "Characterization of mixing in micromixers by a test reaction: single mixing units and mixer arrays." *Industrial and Engineering Chemistry Research* **1999**, *38*, 1075-1082.
2. Floyd, T. M.; Schmidt, M. A.; Jensen, K. F.; "Silicon micromixers with infrared detection for studies of liquid-phase reactions." *Industrial and Engineering Chemistry Research* **2005**, *44*, 2351-2358.
3. Liu, R. H.; Stremmer, M. A.; Sharp, K. V.; Olsen, M. G.; Santiago, J. G.; Adrian, R. J.; Aref, H.; Beebe, D. J.; "Passive mixing in a three-dimensional serpentine microchannel." *Journal of Micromechanical Systems* **2000**, *9*, 190-197.
4. Stroock, A. D.; Dertinger, S. K. W.; Ajdari, A.; Mezic, I.; Stone, H. A.; Whitesides, G. M.; "Chaotic mixer for microchannels." *Science* **2002**, *295*, 647-651.
5. Stroock, A. D.; Dertinger, S. K.; Whitesides, G. M.; Ajdari, A.; "Patterning flows using grooved surfaces." *Analytical Chemistry* **2002**, *74*, 5306-5312.
6. Duda, J. L.; Vrentas, J. S.; "Steady flow in the region of closed streamlines in a cylindrical cavity." *Journal of Fluid Mechanics* **1971**, *45*, 247-260.
7. Günther, A.; Jhunjhunwala, M.; Thalmann, M.; Schmidt, M. A.; Jensen, K. F.; "Micromixing of miscible liquids in segmented gas-liquid flow." *Langmuir* **2005**, *21*, 1547-1555.
8. Song, H.; Tice, J. D.; Ismagilov, R. F.; "A microfluidic system for controlling reaction networks in time." *Angewandte Chemie International Edition* **2003**, *75*, 768-771.
9. Yonemoto, T.; Kubo, M.; Doi, T.; Tadaki, T.; "Continuous synthesis of titanium dioxide fine particles using a slug flow ageing tube reactor." *Transactions of the IChemE* **1997**, *75*, 413-419.
10. Khan, S. A.; Günther, A.; Schmidt, M. A.; Jensen, K. F.; "Microfluidic synthesis of colloidal silica." *Langmuir* **2004**, *20*, 8604-8611.
11. Günther, A.; Khan, S. A.; Thalmann, M.; Tröschel, F.; Jensen, K. F.; "Transport and reaction in microscale segmented gas-liquid flow." *Lab on a Chip* **2004**, *4*, 278-286.
12. Shestopalov, I.; Tice, J. D.; Ismagilov, R. F.; "Multi-step synthesis of nanoparticles performed on the millisecond time scale in a microfluidic droplet-based system." *Lab on a Chip* **2004**, *4*, 316-321.
13. Roylance, D., *Mechanics of Materials*; Wiley: New York, 1996.

14. Donald, I. W.; "Preparation, properties, and chemistry of glass- and glass-ceramic-to-metal seals and coatings." *Journal of Materials Science* **1993**, *28*, 2841-2886. An excellent review on glass brazing with a great deal of practical information and references.

## Chapter 5

# Application of the Segmented Flow Microreactor to the Preparation of CdSe Nanocrystals<sup>†</sup>

### 5.1 Introduction

The reactor design discussed in Chapter 4 is applied to the synthesis of CdSe NCs in this chapter, and the results are compared to those obtained using single-phase flow. Incidentally, beyond NC synthesis, the reactor represents a general platform for high temperature synthesis at very well defined reaction conditions (mixing times and narrow RTD). It has been challenging to adapt the II-VI NC chemistry to a chip-based segmented flow system owing mainly to the reaction temperatures required (>250°C). Liquid-liquid segmented flow has been used to prepare NCs at room temperature in a polydimethylsiloxane device,<sup>1</sup> but solvent miscibility and polymer degradation at high temperatures make it difficult to use this approach to prepare monodisperse, luminescent particles. As mentioned in Chapter 1, the introduction of segmenting gas into heated capillaries has also been implemented, but the uniformity of such gas-liquid flows and their effect on NCs formation were not extensively characterized.<sup>2,3</sup> It should be noted that after the publication of the results in this chapter, researchers did report the successful application of liquid-liquid segmented flow to NC synthesis at high temperature.<sup>4</sup>

In this chapter, it will be shown that the reactor design is capable of rapid mixing and extremely uniform segmentation behavior at the high temperatures required for CdSe NC

---

<sup>†</sup>Much of this chapter has appeared in print: B. K. H. Yen, A. Günther, M. A. Schmidt, K. F. Jensen, M. G. Bawendi, *Angew. Chem. Int. Ed.* **2005**, *44*, 5447-5451.

synthesis. The sample size distributions and reaction yields are superior to those attainable in single-phase flow, with the improvement significantly more pronounced at short times. Since the improvement is a direct consequence of the rapid mixing and narrow RTD features of segmented-flow, the reactor provides a means of greatly reducing the time required to produce high-quality particles compared to existing single-phase approaches. Also, the reactor is applicable to a variety of nanoparticle chemistries because it offers access to a wide range of reaction timescales without compromising acceptable size distributions.

## **5.2 Experimental Details**

### **5.2.1 Segmented Flow Reactor Setup**

The details of the reactor design and fabrication were presented in the previous chapter, so only some specific points will be summarized in this section. Standard 1/16-inch chromatography fittings (Upchurch) were used to connect the brazed Kovar tubing to gas and liquid lines. Syringe pumps (Harvard PHD 2000 and KD Scientific 210) were used to deliver both precursor solutions and segmenting gas. Heating was provided by contacting the reaction section of the device with a heated aluminum block. A molten indium layer was present between the block and device to ensure good thermal conductivity. Cooling of the inlet and quenching regions was accomplished with water-chilled aluminum blocks. Heat transfer paste (Omega) was used to ensure good contact with the cooling blocks. Images of the reactor channel were taken with a consumer digital camera equipped with a macro lens and flash. Figure 5.1 shows photographs of the experimental setup.



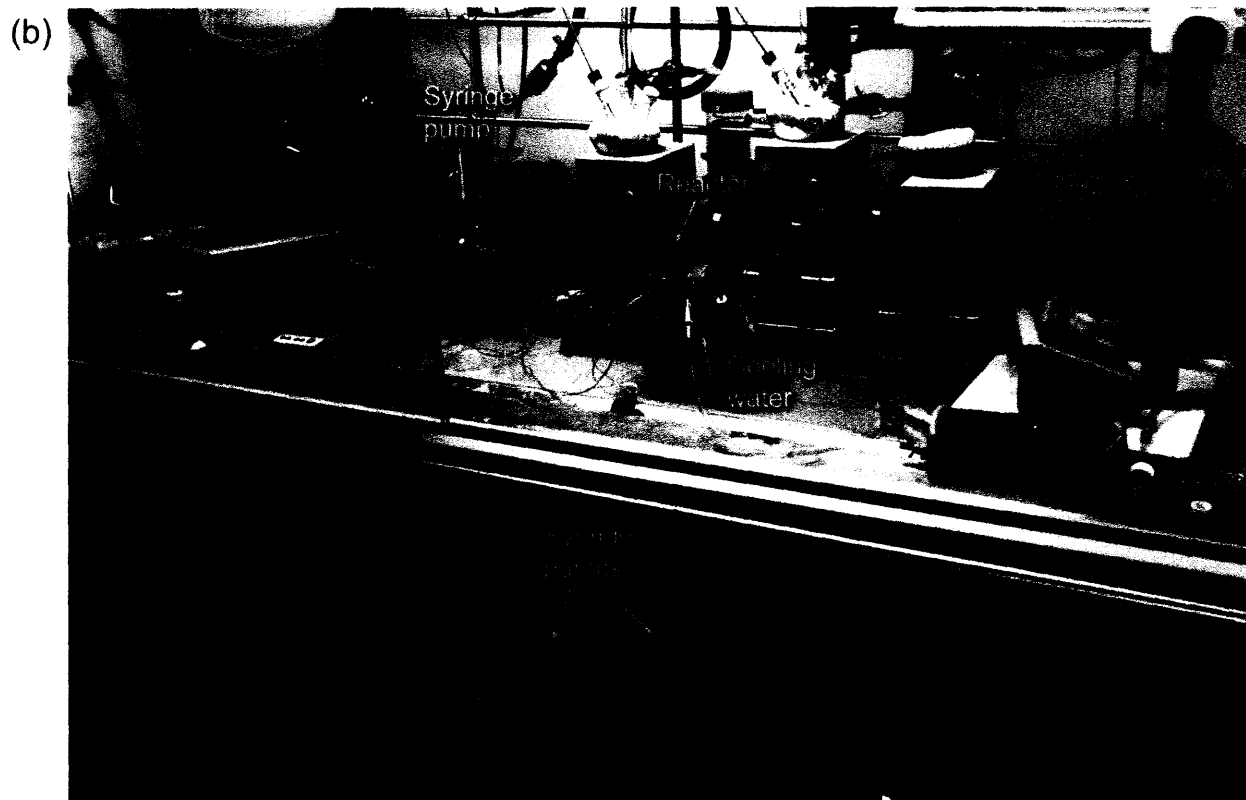
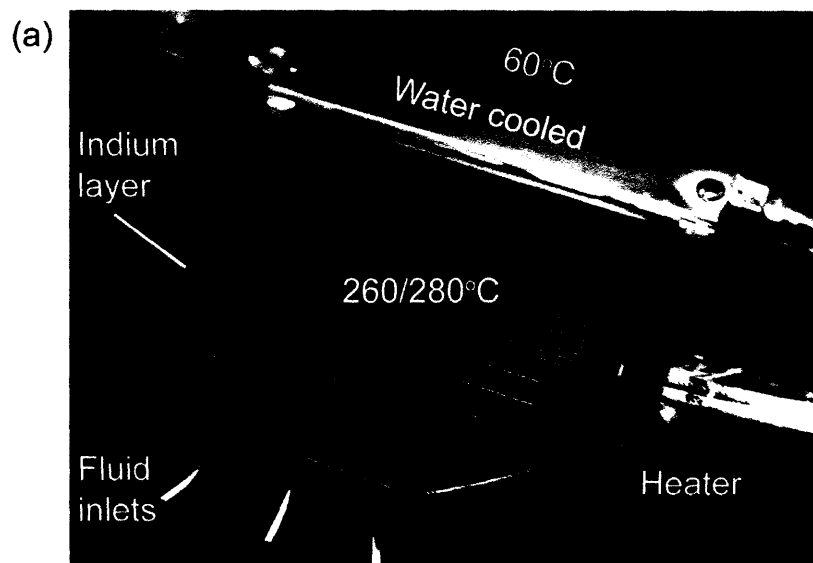


**Figure 5.1:** (a) Photograph of the reactor with heated reaction and cooled outlet regions. A through-etch section ensures that the two regions are thermally isolated. (b) Photograph of experimental setup.

### 5.2.2 Segment Measurement Method

For each flow condition, several hundred individual slug (segment) lengths were measured. The liquid fraction (volume of liquid/total channel volume) was determined from the average slug lengths, and the mean residence time was calculated from the fraction and syringe pump flow rates. Since the end of each slug has appreciable curvature, measured slug lengths were defined in the following manner. The measured gas and liquid slug length ( $l_{gas}$ ,  $l_{liq}$ ) were defined such that 1) the sum  $l_{gas} + l_{liq}$  is equal to one period of the alternating gas-liquid pattern, and 2) the ratio involving average lengths  $l_{liq} / (l_{gas} + l_{liq})$  is proportional to the liquid volume fraction in the channel. The measurement method did not account for the thin liquid film which exists between the channel wall and each gas slug. However, since the film accounts for a small fraction of the total cross section,<sup>5</sup> the error introduced into the calculation of liquid volume fraction is small.

### 5.2.3 Synthetic and Characterization Methods

The Cd and Se precursors were prepared as described in Chapter 2 with a few minor modifications. All manipulations were performed under air-free conditions. Briefly, the Cd precursor was prepared by heating a suspension of 1 mmol cadmium 2,4-pentanedionate (98%, Alfa) in 9 mL squalane (98%, Alfa) and 2.2 mmol oleic acid (99%+, Alfa) at 150°C for 10 min. The optically clear solution was then placed under vacuum at 100°C for ~1.5 hours before the addition of 4 mL oleylamine (Pfaltz and Bauer, 97%). A stock solution of 1.5 M tri-*n*-octylphosphine selenide (TOPSe) was prepared by dissolving an appropriate amount of selenium shot (99.999%, Alfa) in tri-*n*-octylphosphine (TOP, 97%, Strem). The Se precursor solution

consisted of the suitable amount of 1.5 M TOPSe diluted in squalane. The two precursor solutions were degassed thoroughly at 90°C before being loaded into separate syringes.

Samples for measurement of absorbance and PL spectra were prepared by diluting the raw QD solutions in hexanes. Optical absorption spectra were acquired with a Hewlett-Packard 8452 diode array spectrometer. Photoluminescence spectra were acquired using an Ocean Optics SD2000 fiber-optic spectrometer and a handheld UV lamp as an excitation source. Reaction yields were determined from the optical density at 350 nm and the measured absorbance cross-section for CdSe QDs.<sup>6</sup>

## **5.3 Results**

### **5.3.1 Reactor Performance**

The reactor shown in figure 5.1 allows for rapid initial mixing of the precursors, controlled NC growth, and on-chip quenching of the reaction. Precursor solutions were delivered separately into the heated section and an argon stream introduced further downstream results in a segmented gas-liquid flow. Recirculation within the liquid slugs rapidly mixes the heated precursors, thereby initiating the reaction. The fluids initially pass through a meandering section to induce good mixing across the channel before reaching a longer straight-channel section where the majority of the particle growth occurs. The reaction is stopped when the fluids enter the cooled outlet region of the device. The segment lengths are very uniform during conditions of a typical QD synthesis (figures 5.2a,b). Figure 5.2c is a time-averaged image of the cooled outlet region of the device under continuous UV excitation. At the high reaction temperatures, the NC photoluminescence (PL) is completely quenched<sup>7</sup> (bottom portion of

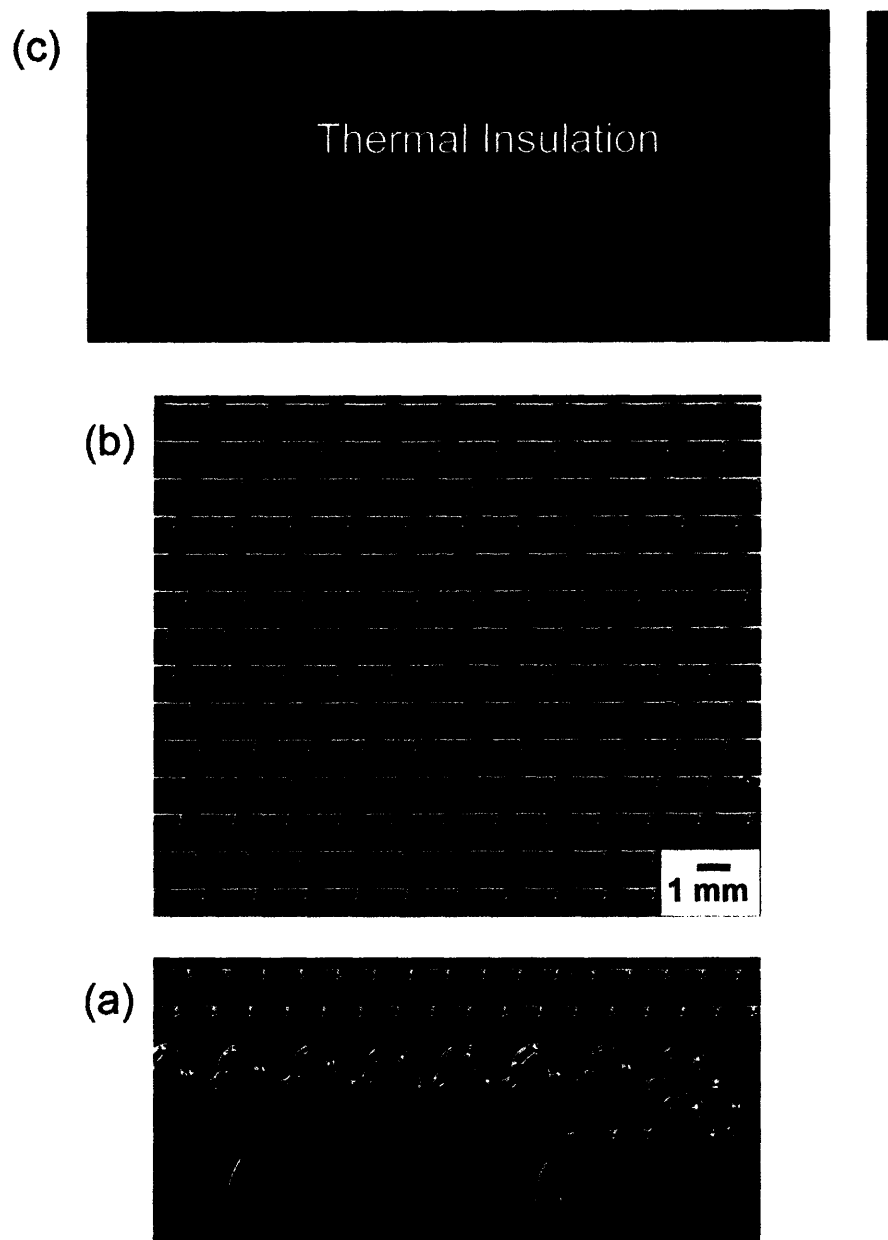


**Figure 5.2:** (a),(b) Images of the heated inlet and main channel section of device. Red segments: NC reaction solution. Dark segments: Ar gas. (c) Time-exposure image of the cooled outlet region under UV irradiation.  $T = 260^{\circ}\text{C}$ , gas =  $60\mu\text{L}/\text{min}$ , liquid =  $30\mu\text{L}/\text{min}$ , Se/Cd = 5.0.

figure 5.2c), but once the fluid reaches the cooled region (<70°C), yellow PL is observed. The image illustrates the ability to maintain the required ~200°C temperature gradient within a single reactor chip.

### 5.3.2 Segmentation Analysis

In general, the residence time depends on the liquid volume fraction in the reactor and the liquid flow rate. The former is controlled by varying the relative gas-to-liquid feed rates. Figure 5.3 shows the liquid volume fraction for a number of flow conditions. Two sets of conditions are shown: 1) variable total fluid flow rate with the ratio of gas-to-liquid flow rates (G/L) kept constant and 2) constant liquid flow rate and variable gas flow rate. For the constant ratio conditions, the liquid volume fraction stays relatively constant over the entire range. For the second case, the liquid fraction decreases steadily as a larger proportion of gas is introduced into the reactor.

The quality of the segmentation shown in figures 5.2a,b deserves further discussion since the slug length distribution can contribute to the RTD and therefore the ultimate NC size distribution. The liquid volume fractions and flow conditions used in figure 5.3 were converted to residence times and the slug statistics for each time was examined. The liquid slug length distributions over this range of residence times are shown in figure 5.4a. The liquid lengths are on the order of the channel hydraulic diameter and typically have a relative standard deviation of ≤10%. The standard deviation of the mean (rather than the standard deviation) of the liquid slug length is directly related to an uncertainty in the residence time:

$$\frac{\sigma_{t_r}}{t_r} = \frac{\sigma_l}{l_{avg} \sqrt{N}} \quad \text{Eq. 5.1}$$

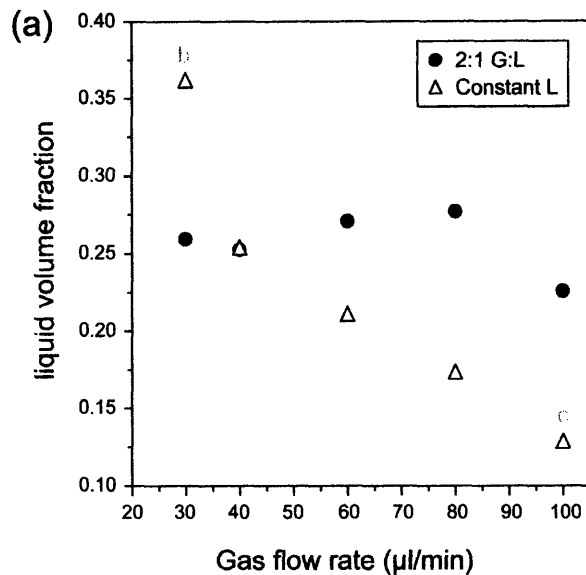


**Figure 5.3:** (a) Liquid volume fraction for various flow conditions at  $260^\circ\text{C}$ . Circles represent varying the total flow rate while maintaining a constant ratio of gas/liquid flow equal to 2. Triangles indicate varying the gas flow rate while keeping the liquid flow rate constant at  $20\mu\text{L}/\text{min}$ . (b), (c) Segmented flow images for conditions corresponding to two extremes in liquid volume fraction.

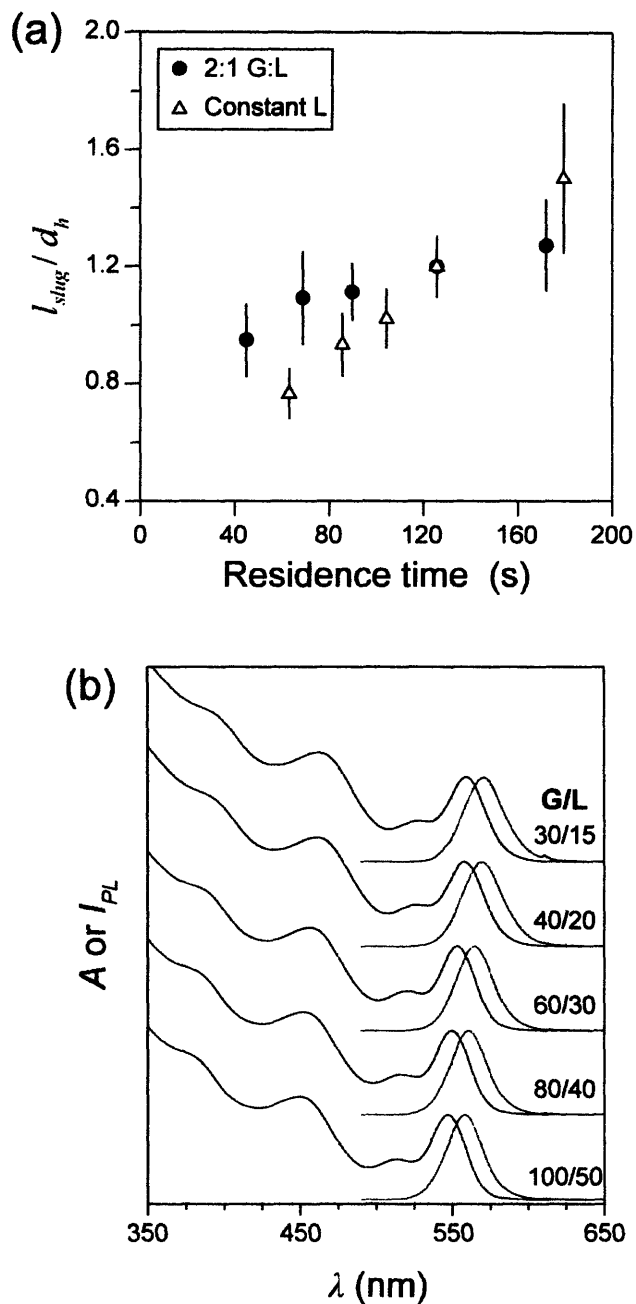


**Figure 5.4:** (a) Ratio of average liquid slug length to hydraulic diameter ( $\sim 400\mu\text{m}$ ) over a range of residence times at  $260^\circ\text{C}$ . Flow conditions correspond to those shown in figure 5.3. Error bars indicate the standard deviation of the liquid slug length for a given flow condition. Circles represent the following gas/liquid flow rates (ratio kept equal to 2): 100/50, 80/40, 60/30, 40/20, and 30/15  $\mu\text{L}/\text{min}$ . Triangles represent the following flow rates (liquid flow rate kept at 20  $\mu\text{L}/\text{min}$ ): 100/20, 80/20, 60/20, 40/20, and 30/20  $\mu\text{L}/\text{min}$ . (b) Absorbance (blue) and PL (red) spectra for CdSe NCs prepared under the flow conditions represented by the circles.

where  $t_r$  is the residence time,  $l$  is the length of an individual slug, and  $N$  is the number of liquid slugs in the reactor (typically  $\sim 300$ ). Since  $\sigma_l/l_{avg} \sim 10\%$ ,  $\sigma_{t_r}/t_r < 0.6\%$ . In other words, this dispersion in the slug lengths is small enough so that its contribution to the overall RTD is negligible. It should be noted that the reported gas flow rates do not include the significant, although steady, gas leakage from the syringe and tubing fittings leading up to the reactor. This was the case even with nominally gas-tight syringes. However, the slug lengths were measured directly from images taken of the reactor channel so the reported mean residence times are accurate.

### 5.3.3 Results for CdSe NCs

The spectra of the resulting NC samples indicate narrow size distributions (figure 5.4b) and are comparable to the best samples achieved in the batch process. The band-edge absorbance and several higher transitions are clearly resolved, and the PL line-widths remain narrow over the entire range of flow rates. In the figure, the PL full-width-at-half-maximum (FWHM) varies between 28 and 31 nm (112 and 119 meV depending on wavelength).

In figure 5.4b, the NCs were prepared with a constant precursor composition and represent a fairly limited spectral range ( $< 10$  nm variation in band-edge position). As discussed in Chapter 2, size tuning is better achieved by varying the ratio Se/Cd rather than reaction time. In figure 5.5, such an effect is demonstrated by varying the Cd and Se precursor flow rates while keeping the total liquid and gas flow rates constant (20 and 40  $\mu\text{L}/\text{min.}$ , respectively). In contrast to figure 5.4b, varying the molar ratio of Se/Cd from 15 to 1.7 made it possible to tune the effective band-gap of the QDs over a much larger spectral range of  $\sim 40$  nm while



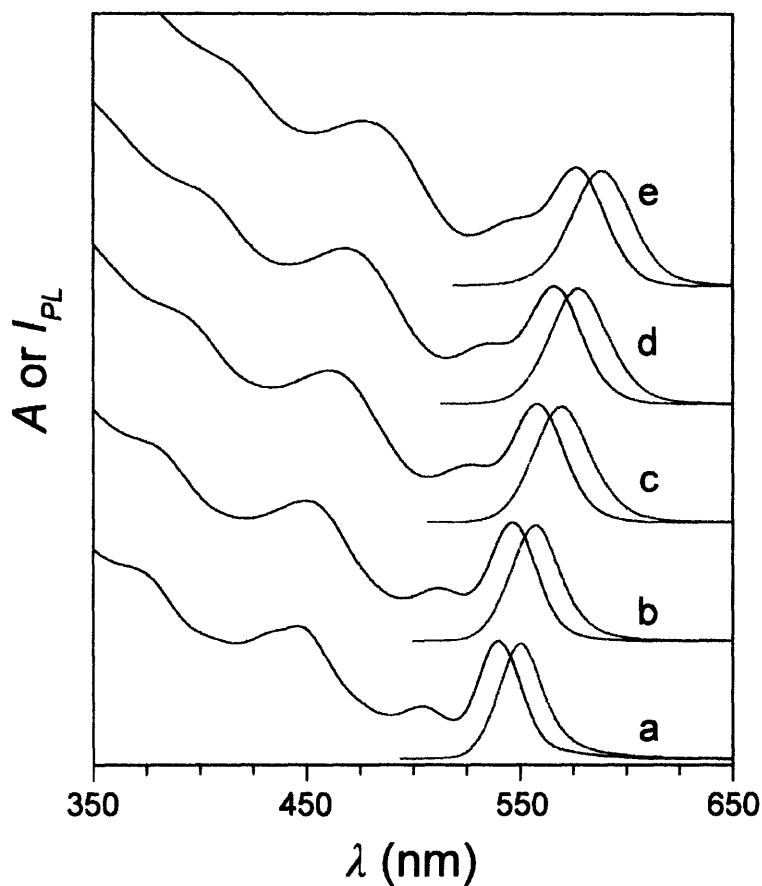


**Figure 5.5:** NC spectra obtained by varying the precursor feed ratio ( $T = 260^{\circ}\text{C}$ ). The total gas and liquid flow rates were kept constant ( $L_{\text{Se}} + L_{\text{Cd}} = 20\mu\text{L}/\text{min}$ ,  $G = 40\mu\text{L}/\text{min}$ ). Spectra correspond to the flow rates ( $L_{\text{Se}}/L_{\text{Cd}}$ ) and resulting molar ratios (Se/Cd) of (a) 3.0 and 15, (b) 1.67 and 8.3, (c) 1.0 and 5.0, (d) 0.60 and 3.0, (e) 0.33 and 1.7.

maintaining narrow size distributions. The average NC radius decreases with increasing Se/Cd owing to the strong dependence of the nucleation rate on the precursor ratio. The samples represented in figure 5.5 were produced using the same temperature (260°C) and mean residence time (~140 s). By varying the temperature and reaction time in addition to the precursor feed ratios, it would be possible to tune the effective band-gap over an even larger spectral window as demonstrated in Chapter 2.

#### **5.3.4 Comparison with Single-Phase Flow**

In general, the spectra of NCs produced in single-phase operation ( $G = 0$ ) were significantly broader than those obtained using gas-liquid flow. The poorer performance observed in the single-phase case is primarily due to the combination of two effects: initial mixing and broad RTD. In single-phase flow, the two precursor streams combine slowly by diffusion in contrast to the convective mixing induced by the introduction of a segmenting gas. Based on reference 8 (figure 4.4 in Chapter 4), the mixing length of the reactor under segmented flow conditions can be conservatively estimated to be ~30 channel widths. This corresponds to a mixing time of <1% of the average residence time. For the single-phase case, the diffusive mixing time can be >50% of the average residence time depending on the flow rate (Chapter 3). Slow initial mixing makes it difficult to realize a rapid nucleation burst, and the resulting NC samples are polydisperse. Once the reagents are completely mixed, the influence of axial dispersion is still present so that NCs near the channel wall spend a longer time in the reactor than those in the center. In segmented flow, recirculation within the liquid brings fluid from the channel wall to the center, making it possible to realize rapid mixing, lower dispersion in residence times, and therefore narrower QD size distributions (figure 4.6 in Chapter 4).

In order to isolate the RTD contribution from the effects of initial mixing, the inlet region of the reactor was cooled and the precursors were pre-mixed with a miniature convective mixer (figure 5.6). A deep trench feature made it possible to keep the inlets thermally isolated from the main reaction channel. Cooling the inlets ensures that the pre-mixed precursors did not react until they reached the heated reaction section. In this way, the influence of initial reagent homogenization was eliminated and it was possible to directly observe the RTD effect on the NC size distribution. The spectra in figure 5.7a illustrate the improvement of the size distribution resulting from segmentation. Figure 5.7b is a plot of the full-width-at-half-maximum (FWHM) of the PL peak for samples prepared at several flow conditions (mean residence times). For reaction times shown in figure 5.7b, the PL FWHM varies between 28 and 32 nm (99-128 meV) for segmented flow, and 29 and 39 nm (104-158 meV) for single-phase flow. In both plots in Figure 5.7b, the PL peak width decreases with time, and this general trend (size distribution focusing) has been explained as evidence of the presence of a mass-transfer component in the particle growth rate (Chapters 1 and 2). However, the absorbance and PL spectra of NCs produced in gas-liquid flow are generally sharper in comparison to the single-phase case, and the difference in figures 5.7a,b between single and two phase operation becomes more pronounced at shorter timescales. This behavior at short times results from the fact that the RTD broadens significantly with flow rate in single phase flow (Chapter 2 and 3), while the RTD does not have such a strong flow rate dependence in the segmented case. It should be noted that cooling the inlets is not the normal mode of operation for the device. When the gas is introduced at low temperature, the slug uniformity is substantially poorer than the very uniform segments shown in figures 5.2a,b. This flow destabilization primarily results from rapid expansion of gas and the

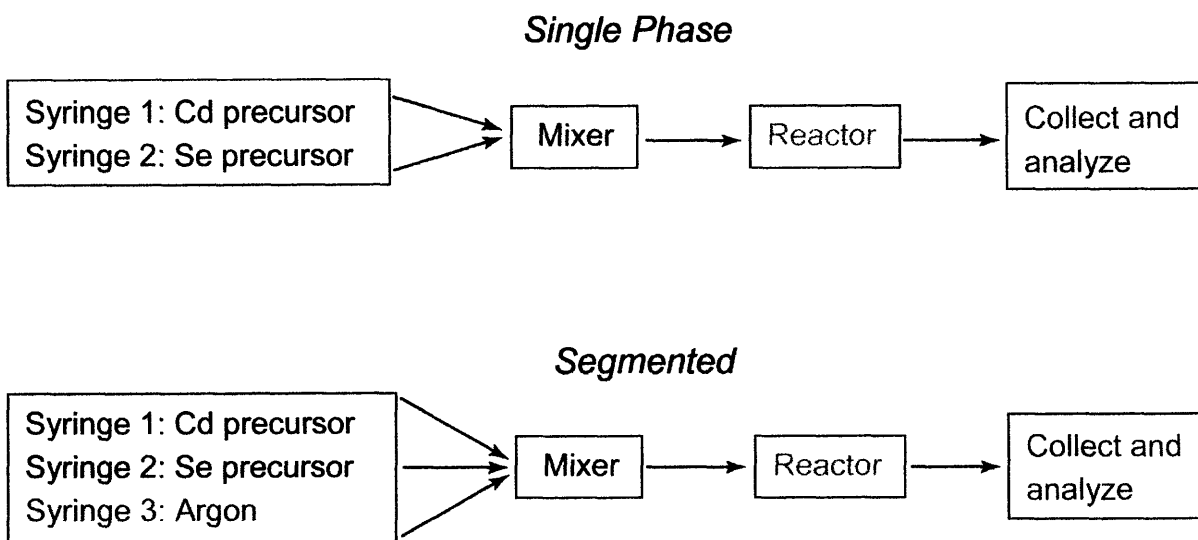


**Figure 5.6:** Experimental setup used to compare single-phase and segmented flow. Inlet region is cooled and precursors are pre-mixed in order to eliminate the effects of initial mixing.

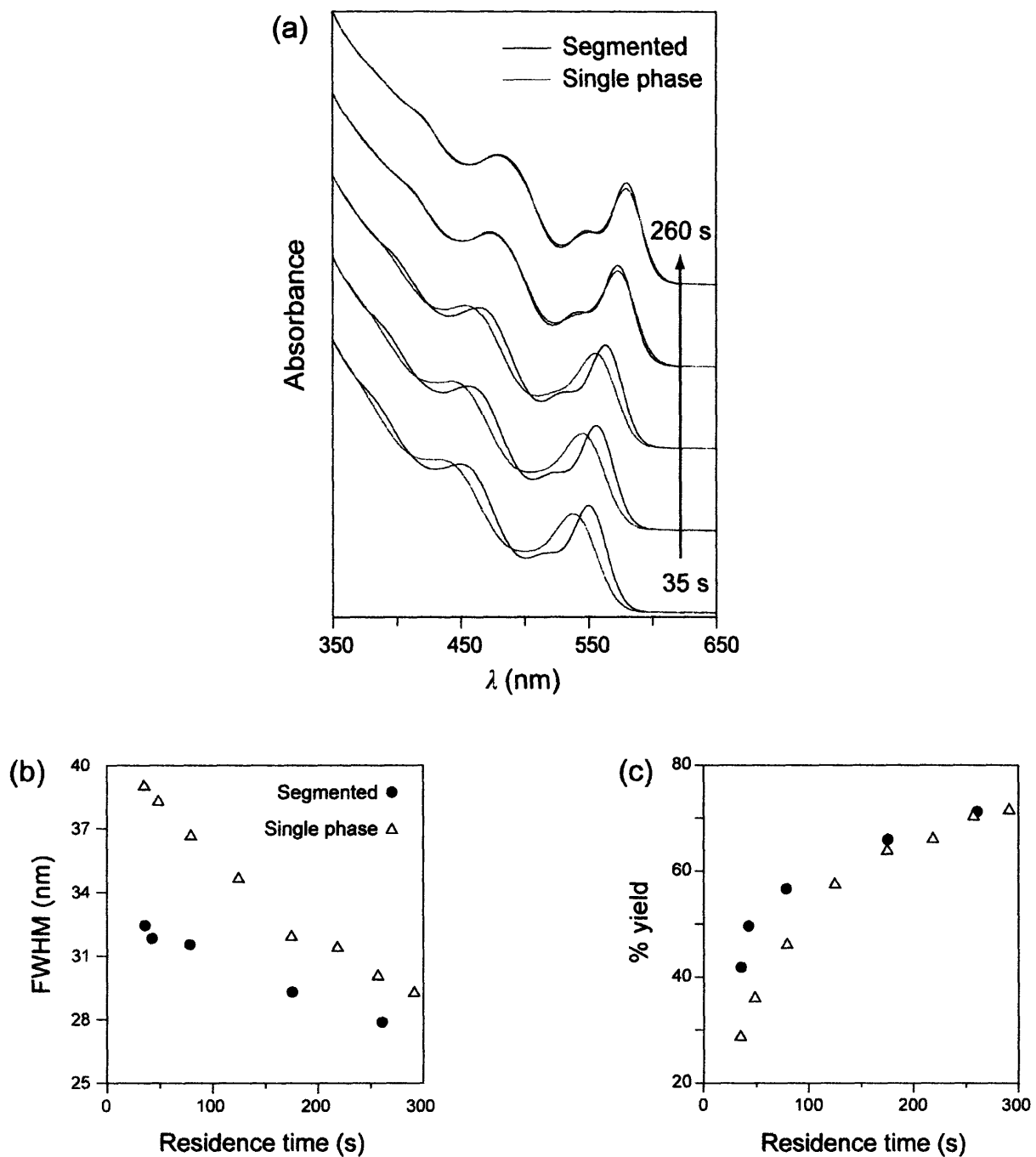


**Figure 5.7:** (a) Absorbance spectra of QDs prepared with segmented (blue) and single phase (red) flow. Each pair of spectra corresponds to approximately the same mean residence time. (b),(c) PL full-width-at-half-maximum and reaction yield of NC samples prepared in segmented (circles) and single phase (triangles) flow. For segmented flow, G/L was varied between 15/10 and 100/40 $\mu$ L/min. For single phase flow, L was varied between 34 and 250 $\mu$ L/min. T = 280°C, [Se]/[Cd] = 1.0.

large change in liquid viscosity when the fluids reach the heated section. In spite of such non-uniform segmentation, we still observe a significant improvement in QD size distribution. Incidentally, the observed deterioration of slug uniformity underscores the importance of introducing the segmentation on-chip at the reaction conditions rather than farther upstream before the fluids enter the reactor.

Figure 5.7c reveals an additional reason for the larger improvement in size distribution at shorter reaction times. In segmented flow, the mixing timescale that is governed by recirculation within liquid slugs decreases almost linearly with flow rate.<sup>8</sup> Thus, a shorter reaction time (faster flow rate) is compensated by more intense stirring, and vice versa. The inverse relationship between stirring intensity and reaction time is manifested in the reaction yield curves shown in figure 5.7c. At shorter times (high flow rates), the NC reaction is driven to higher yields compared to single-phase operation. The more rapid growth causes the QD population distribution to focus more quickly than the single-phase case, and consequently, the difference in the two curves in figure 5.7b becomes larger at short times. At lower flow rates, the recirculatory stirring is slower, but the reaction time is longer so the yield curve converges with the curve for single-phase flow. Even at the longest times (when the yields are comparable for the two cases), the PL spectra for gas-liquid flow is still somewhat narrower, indicating that the improved RTD effect on size distribution is still present.

## **5.4 Conclusions**

In summary, synthesis of acceptable NC samples by the single-phase approach requires long reaction times so that size distribution focusing and narrowing of the RTD have time to fully develop. In segmented flow, the enhanced mixing accelerates the growth process, thereby

reducing the time required for focusing of the size distribution, and a narrow RTD is sustained even at high flow rates. For example, from figure 5.7b, the narrow size distribution achieved in 42 sec. with segmented flow requires over four times longer (~175 sec.) to achieve using single phase flow.

The reactor design presented in this chapter is applicable to a range of chemistries because it is possible to operate at high temperatures while maintaining excellent mixing characteristics and small extents of axial dispersion. To illustrate the unique features of the design, it was applied to the synthesis of CdSe NCs. Under reaction conditions, the segmentation is very uniform, and the resulting monodisperse samples exhibit excellent optical properties. Compared to single-phase flow, the enhanced mixing and narrow RTD characteristics of the reactor result in a significant improvement in reaction yield and size distribution, especially at short times. Such attributes are highly desirable from the standpoint of chemical production since it is possible to increase throughput without sacrificing narrow size distributions. Also, the reactor is applicable to particle systems in which the optimal reaction timescales are shorter than that of CdSe NC, in contrast to single-phase devices which are limited to long times. In addition to being a synthesis tool, varying the mean slug velocity and length in the reactor channel provides a means of reproducibly controlling the mass transfer rate during particle growth, which is not possible in single-phase flow or the conventional batch method. This makes the reactor design ideally suited for the systematic study of the mechanism of NC formation.

## 5.5 References

1. Shestopalov, I.; Tice, J. D.; Ismagilov, R. F.; "Multi-step synthesis of nanoparticles performed on the millisecond time scale in a microfluidic drople-based system." *Lab on a Chip* **2004**, *4*, 316-321.
2. Nakamura, H.; Yamaguchi, Y.; Miyazaki, M.; Maeda, H.; Uehara, M.; Mulvaney, P.; "Preparation of CdSe nanocrystals in a micro-flow reactor." *Chemical Communications* **2002**, 2844-2845.
3. Yen, B. K. H.; Stott, N. E.; Jensen, K. F.; Bawendi, M. G.; "A continuous-flow microcapillary reactor for the preparation of a size series of CdSe nanocrystals." *Advanced Materials* **2003**, *15*, 1858-1862.
4. Chan, E. M.; Alivisatos, A. P.; Mathies, R. A.; "High-temperature microfluidic synthesis of CdSe nanocrystals in nanoliter droplets." *Journal of the American Chemical Society* **2005**, *127*, 13854-13861.
5. Wong, H.; Morris, S.; Radke, C. J.; "Three-dimensional menisci in polygonal capillaries." *Journal of Colloid and Interface Science* **1992**, *148*, 317-336.
6. Leatherdale, C. A.; Woo, W.-K.; Mikulec, F. V.; Bawendi, M. G.; "On the absorption cross section of CdSe nanocrystal quantum dots." *Journal of Physical Chemistry B* **2002**, *106*, 7619-7622.
7. Walker, G. W.; Sundar, V. C.; Rudzinski, C. M.; Wun, A. W.; Bawendi, M. G.; Nocera, D. G.; "Quantum-dot optical temperature probes." *Applied Physics Letters* **2003**, *83*, 3555-3557.
8. Günther, A.; Jhunjhunwala, M.; Thalmann, M.; Schmidt, M. A.; Jensen, K. F.; "Micromixing of miscible liquids in segmented gas-liquid flow." *Langmuir* **2005**, *21*, 1547-1555.



## **Chapter 6**

# **Extending the Gas-Liquid Segmented Flow Approach: Continuous Injection of Multiple Precursor Streams**

### **6.1 Introduction**

In the previous chapters, the microreactors were designed so that precursors were initially mixed (either by mixing off chip or by segmentation) and subsequently allowed to react within a heated zone. In this way, these microfluidic approaches are similar to single injection batch preparations of NCs. The monomer concentration initially increases as the precursors decompose and then continuously decreases with time as these species are depleted by the nucleation and growth process. As demonstrated in chapters 2 and 6, varying parameters such as the initial concentration, temperature and flow rate (total reaction time) made it possible to control the temporal evolution of monomer concentration so that monodisperse spherical particles could be produced over a significant range of average sizes. However, the synthesis of other types of NCs requires an additional level of control that is not possible with the heretofore described reactor designs. In particular, the synthesis of two broad classes of NCs, anisotropic particles and heterostructures, require a high or constant level of precursor concentration throughout the reaction.

The monomer concentration profiles during the formation of anisotropic NCs, growth of heterostructured NCs, and spherical NCs are shown schematically in figure 6.1. The curve for

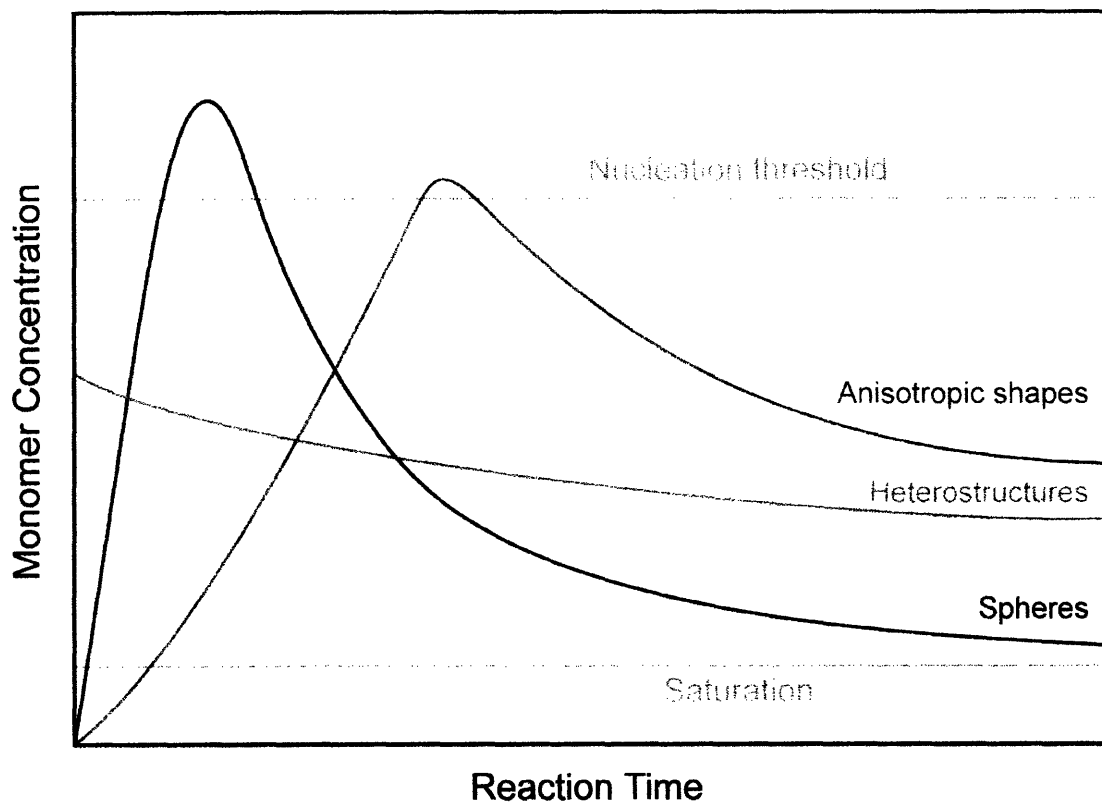


**Figure 6.1:** Depiction of the monomer concentration profile during the formation of three types of NCs.

the spherical case was described in Chapter 1. Briefly, thermal decomposition of the precursors causes the monomer concentration to increase beyond the nucleation threshold. Formation of nuclei quickly depletes the concentration below the threshold. The solution is still supersaturated so growth on the existing nuclei is thermodynamically favored, and the monomer species is slowly depleted as this process proceeds. The curve for anisotropic growth (eg. growth of rods or wires) differs in that a smaller amount of the precursors is consumed during the nucleation stage. This leaves a generally higher concentration of monomers or precursors during the growth stage. A higher concentration of these species biases the growth toward a kinetic-controlled regime. In this regime, the more reactive crystal surfaces will grow faster than less reactive ones, leading to an anisotropic particle. This is in contrast to the diffusion-controlled regime wherein the growth rate on a given facet is dictated by the equilibrium solubility of the facet. For II-VI semiconductors in particular, rod or tetrapod shaped NCs are obtained under conditions of high precursor concentrations.<sup>1-5</sup> It has been shown that the long axis of the rods or tetrapod arms lie along the [001] direction. This is consistent with kinetic-controlled growth since the corresponding (001) and (00 $\bar{1}$ ) crystal faces contain more dangling bonds compared to the other exposed surfaces on the NC, and growth would be expected to proceed fastest upon these more energetic facets.

In practice, scaling up the concentrations used in the chemistry described in Chapters 2 and 6 (or other standard CdSe NC preparations) does not, on its own, lead to the production of appreciably anisotropic particles. This is because a higher initial concentration will greatly increase the rate and extent of the nucleation burst, leaving an insufficient concentration of species to drive the growth stage into the kinetic control regime. A strongly binding ligand is

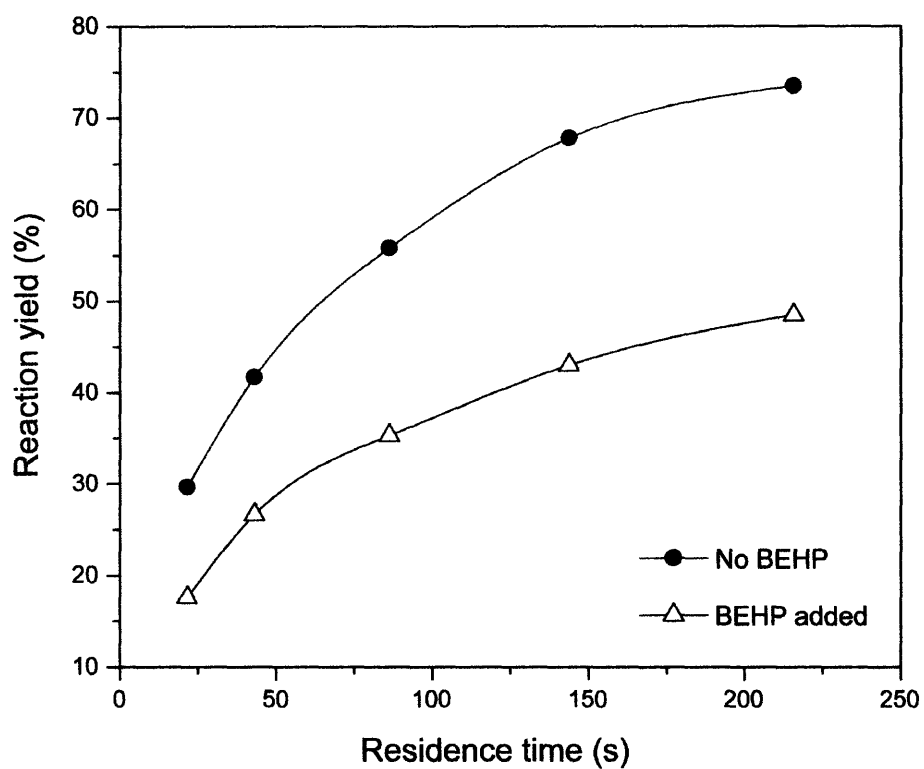


**Figure 6.2:** Effect of BEHP ligand on the synthesis of CdSe NCs. The red curve corresponds to a CdSe NC preparation using a 5:1 Se:Cd initial precursor ratio. The blue curve resulted from adding an equimolar amount of BEHP relative to Cd to the reaction mixture. For both cases, the reaction temperature was 240°C, and the data were acquired using the capillary reactor described in Chapter 2.

usually introduced during the synthesis in combination with a high initial precursor concentration. Phosphonic acids are used in the case of CdSe<sup>3</sup> and carboxylic acids have been used in the case of CdTe<sup>2</sup>. The ligands bind strongly to the precursor metal center and any nascent monomer cluster species. This serves to greatly reduce the rate and extent of nucleation so that the remaining monomer concentration is still sufficiently high for growth to proceed under kinetic control. The inhibiting effect of phosphonic acids in the CdSe system is shown in figure 6.2. In the figure, a phosphonic acid analogue, bis(2-ethylhexyl)phosphate was introduced into the chemistry used in Chapter 2. The reaction yield curves shown were obtained using the single-phase capillary system. The strong-binding of the BEHP ligand greatly slows the NC formation process in comparison to reactions performed in the absence of BEHP. In the case of CdSe, the presence of phosphonic acids has an added benefit in that these ligands appear to preferentially bind to crystal {100} planes which further biases growth along the c-axis. A second method of promoting anisotropic growth during batch syntheses is by performing additional injections of precursor solutions during the growth stage.<sup>2,5</sup> The amount of each injection is judiciously chosen so that the kinetic control of the growth is favored but the monomer concentration does not become so high as to promote further nucleation.

Growth of NC heterostructures is also shown in figure 6.1. Bandgap engineering by growing a different semiconductor material on an existing NC has proven to be a versatile method of further tailoring the properties of these materials. For instance, adding a layer of higher bandgap material on an existing semiconductor NC (CdSe/ZnS core shell NCs) imparts greater stability and increases the overall brightness.<sup>6-11</sup> Growth of a material with an appropriate band offset to the underlying core material results in a type II heterostructure in which the effective bandgap of the composite NC is much lower in energy than either of the two

component semiconductors.<sup>12,13</sup> The synthetic procedure for growing a second material involves continuously adding precursors to a solution containing the NC cores. The concentration and addition rate are chosen so that the monomer concentration maintains an approximately steady level which never exceeds the nucleation threshold (figure 6.1). In this way, homogeneous nucleation of the second material is avoided and controlled growth to a desired shell thickness can be achieved. Incidentally, the secondary injection or continuous addition methods can be applied to grow NC cores to larger sizes while keeping the growth in the size distribution focusing regime.<sup>14</sup>

By performing multiple injections or continuous precursor additions, it is possible to more effectively decouple nucleation and growth in contrast to the single injection method used to prepare NC cores. This principle can be transferred to the segmented flow microfluidic regime as shown in figure 6.3. In a gas-liquid segmented flow, the gas is the dispersed phase, and the liquid comprises a continuous phase. This enables the controllable and continuous addition of a second liquid stream into the main flow as shown in the figure. The added precursors are then rapidly mixed due to the segmentation. This chapter describes the implementation of such a principle in a microreactor for the synthesis of anisotropic and heterostructured NCs.



**Figure 6.3:** Continuous addition of a second stream (red) into a gas-liquid segmented flow (blue). This is possible because the liquid exists as a continuous phase in the two phase flow. In practice, bends will be introduced into the channel to encourage mixing across the center line.

## 6.2 Reactor Design

### 6.2.1 Analysis of Flow Uniformity in Feeder Channels

The addition of extra feeder channels to a design based on the one shown in Chapters 4 and 5 is described in this section. Seven side channels were added at equally spaced intervals along the long main. Continuous operation of these feeder channels should make it possible to maintain a high and steady concentration of precursor within the main reaction channel. For practical purposes, the seven channels will originate from a common inlet manifold. A schematic of the fluidic network to be implemented is shown in figure 6.4.

Since the side channel flows begin from a common inlet, these channel dimensions must be designed correctly. Generally speaking, the side channels should be long and narrow so that the resulting pressure drop across them is much larger than the drop across the main reaction channel. This ensures that the flow coming into the inlet is evenly distributed to the seven feeder channels. Each channel should have a hydraulic diameter of at least  $\sim 50\mu\text{m}$  since anything narrower could encourage clogging during operation. The main reaction channel is similar in dimensions to the one described in Chapters 4 and 5 (1 meter in length with a hydraulic diameter of  $400\mu\text{m}$ ). In order to determine the required length of the side channels, the fluid network shown in figure 6.4 should be solved for a segmented flow in the main channel. Determining the pressure drop in gas-liquid segmented flow is challenging, but solving the fluid network using a single-phase liquid flow should be sufficiently accurate to provide guidance on the required length of the pressure drop channels.



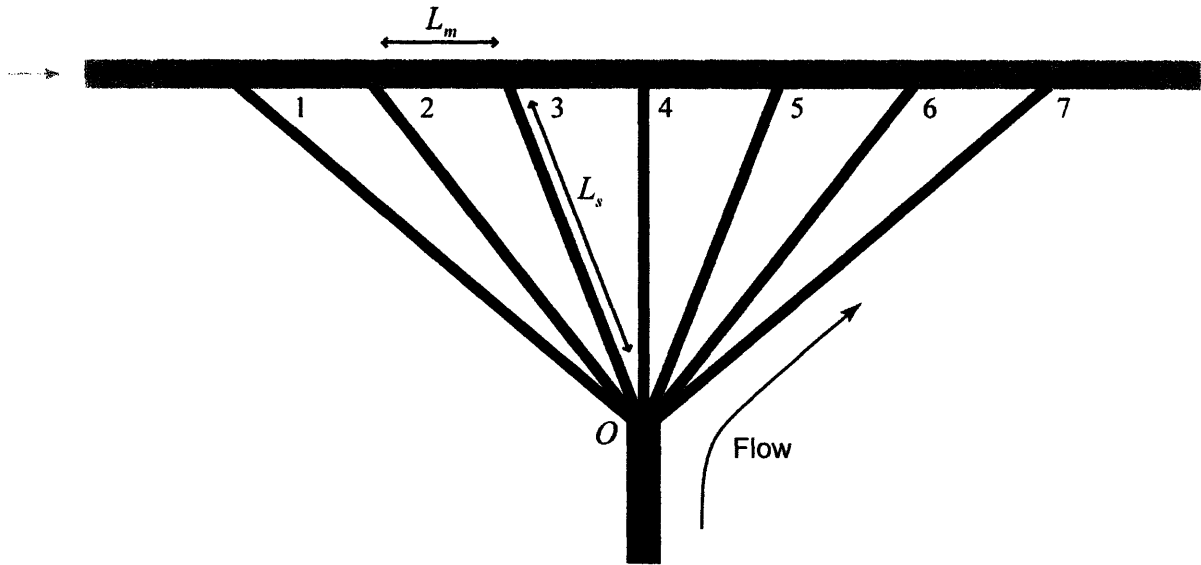


**Figure 6.4:** Channel network used in the flow distribution calculation. A flow from a common inlet is distributed at point  $O$  into seven feeder channels (blue), where it combines with flow in the main channel (gray). The channel length ( $L_s$ ) is the same for all seven side channels even though this does not appear to be the case in the diagram.

For a single-phase laminar flow, the relationship between the pressure drop  $\Delta P$  and volumetric flow rate  $F$  is given approximately by:<sup>15</sup>

$$\Delta P = \left( \frac{8\mu L}{\pi r_h^4} \right) F = \alpha F, \quad \text{with } \alpha = \left( \frac{8\mu L}{\pi r_h^4} \right) \quad \text{Eq. 6.1}$$

where  $\mu$  is the fluid viscosity,  $L$  is the channel length, and  $r_h$  is the hydraulic radius of the channel. In figure 6.4,  $L_s$  and  $r_s$  are the length and hydraulic radius of each side channel, respectively.  $L_m$  and  $r_m$  are the length of the main channel between two feeder positions and  $r_m$  is the hydraulic radius of the main channel (200 $\mu$ m). Using equation 6.1,  $\alpha_s$  and  $\alpha_m$  are defined in terms of the geometry of the two types of channels:

$$\alpha_s = \left( \frac{8\mu L_s}{\pi r_s^4} \right) \quad \alpha_m = \left( \frac{8\mu L_m}{\pi r_m^4} \right) \quad \text{Eqs. 6.2a,b}$$

Given a main channel flow rate of  $F_m$  (does not including the aggregate feeder channel flows), the fluid network is solved by tracing the pressure drop between O and 7 along different paths in figure 6.4. For instance, the pressure drop taking the direct path O-7 is found by using equation 6.1:

$$\Delta P_{O7} = \alpha_s F_7 \quad \text{Eq. 6.3}$$

where  $F_i$  is the flow rate in the  $i^{\text{th}}$  side channel. The pressure drop  $\Delta P_{O7}$  is also given by taking the path O-6-7:

$$\Delta P_{O7} = \Delta P_{O6} + \Delta P_{67} = \alpha_s F_6 + \alpha_m (F_1 + F_2 + \dots + F_6 + F_m) \quad \text{Eq. 6.4}$$

Continuing by taking the path O-5-6-7 results in:

$$\begin{aligned} \Delta P_{O7} &= \Delta P_{O5} + \Delta P_{56} + \Delta P_{67} = \alpha_s F_5 + \alpha_m (F_1 + F_2 + \dots + F_5 + F_m) + \alpha_m (F_1 + F_2 + \dots + F_6 + F_m) \\ &= \alpha_s F_5 + \alpha_m (2F_1 + 2F_2 + 2F_3 + 2F_4 + 2F_5 + F_6 + F_m) \end{aligned} \quad \text{Eq. 6.5}$$

Exhausting all seven paths in this manner results in seven equations and eight unknowns ( $F_i$ 's and  $\Delta P_{07}$ ). The eighth equation is given by mass balance:

$$F_m + \sum_{i=1}^7 F_i = F_{tot} \quad \text{Eq. 6.6}$$

The system of equations is most conveniently solved by first expressing them in matrix format:

$$\mathbf{Ax} = \mathbf{c} \quad \text{Eq. 6.7}$$

where  $\mathbf{A}$  is a coefficient matrix,  $\mathbf{x}$  is the vector of unknowns, and  $\mathbf{c}$  is the vector of constants.

The ordering of variables within  $\mathbf{x}$  and the constants within  $\mathbf{c}$  are given below:

$$\mathbf{x} = \begin{pmatrix} F_1 \\ F_2 \\ F_3 \\ F_4 \\ F_5 \\ F_6 \\ F_7 \\ \Delta P_{07} \end{pmatrix} \quad \mathbf{c} = \begin{pmatrix} -6\alpha_m F_m \\ -5\alpha_m F_m \\ -4\alpha_m F_m \\ -3\alpha_m F_m \\ -2\alpha_m F_m \\ -\alpha_m F_m \\ 0 \\ F_{tot} - F_m \end{pmatrix} \quad \text{Eq. 6.8a,b}$$

The coefficient matrix is given below with the columns labeled with variable names and rows labeled by equation number:

	$F_1$	$F_2$	$F_3$	$F_4$	$F_5$	$F_6$	$F_7$	$\Delta P_{07}$
1	$\alpha_s + 6\alpha_m$	$5\alpha_m$	$4\alpha_m$	$3\alpha_m$	$2\alpha_m$	$\alpha_m$	0	-1
2	$5\alpha_m$	$\alpha_s + 5\alpha_m$	$4\alpha_m$	$3\alpha_m$	$2\alpha_m$	$\alpha_m$	0	-1
3	$4\alpha_m$	$4\alpha_m$	$\alpha_s + 4\alpha_m$	$3\alpha_m$	$2\alpha_m$	$\alpha_m$	0	-1
4	$3\alpha_m$	$3\alpha_m$	$3\alpha_m$	$\alpha_s + 3\alpha_m$	$2\alpha_m$	$\alpha_m$	0	-1
5	$2\alpha_m$	$2\alpha_m$	$2\alpha_m$	$2\alpha_m$	$\alpha_s + 2\alpha_m$	$\alpha_m$	0	-1
6	$\alpha_m$	$\alpha_m$	$\alpha_m$	$\alpha_m$	$\alpha_m$	$\alpha_s + \alpha_m$	0	-1
7	0	0	0	0	0	0	$\alpha_s$	-1
8	1	1	1	1	1	1	1	0

The matrix equation was solved analytically by standard Gauss-Jordon reduction resulting in the flow distribution  $\{F_i\}$ .

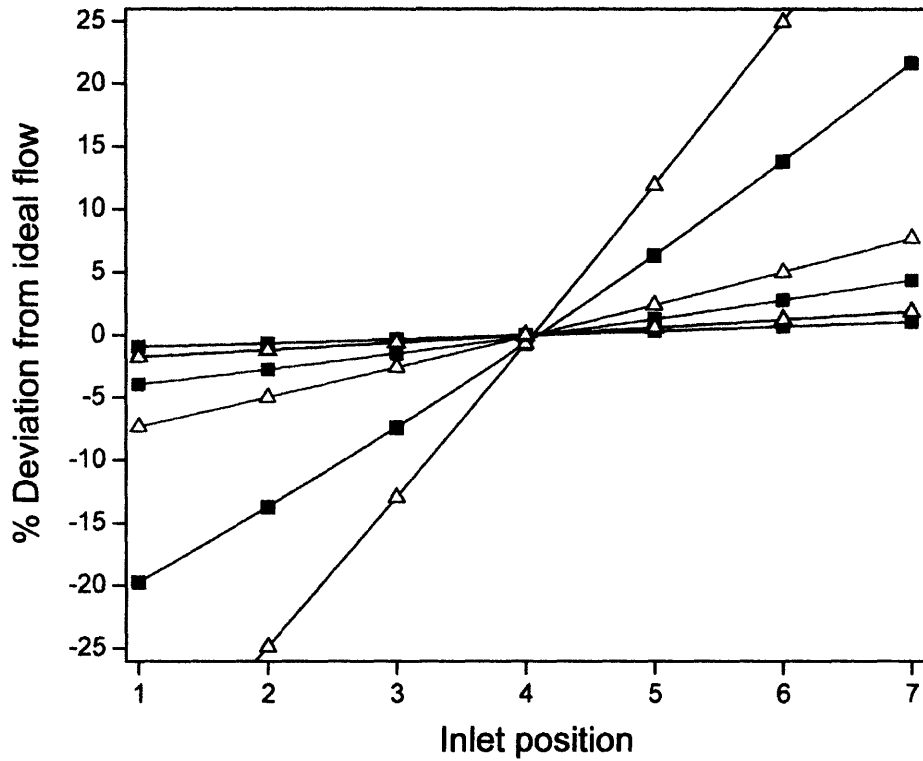
Though the flow rate distribution was already calculated above, it may also be of interest to compare the actual pressure drop across each of the side channels (Recall that a uniform flow distribution results from designing a high pressure drop across the side manifold relative to the drop across the main channel). The pressure drop across a given side channel from point  $O$  to point  $i$  ( $i = 1, 2, 3, \dots, 7$ ) is given directly by:

$$\Delta P_{O_i} = \alpha_s F_i \quad \text{Eq. 6.9}$$

( $\Delta P_{O7}$  was already found by solving the matrix equation). The pressure drop across the main channel from point 1 to 7 is most conveniently found by tracing the path  $I-O-7$ :

$$\Delta P_{17} = \Delta P_{1O} + \Delta P_{O7} = -\alpha_s F_1 + \alpha_s F_7 \quad \text{Eq. 6.10}$$

Based on the dimensions of the main channel from Chapter 4 (1m long,  $d_h = 400\mu\text{m}$ ), the flow distribution for some typical flow rates and channel geometries was calculated and presented in figure 6.5. The corresponding side channel pressure drops ( $\Delta P_{i7}$ ) relative to the main channel drop ( $\Delta P_{17}$ ) are shown in table 6.1. Based on the figure and table values, a feeder channel length of  $\sim 14$  cm and  $d_h$  of  $\sim 50\mu\text{m}$  will maintain a pressure drop over an order of magnitude larger than the drop over the main channel even at low flow rates. The resulting flow distribution deviates by only a few percent from perfectly uniform distribution. These dimensions are implemented in the reactor design described in the next section.



<u><math>L_s, d_h</math></u>	<u><math>\Sigma F_n</math></u>
— 7 cm, 90 μm	Δ 7 μL/min
— 7 cm, 60 μm	■ 14 μL/min
— 14 cm, 50 μm	

**Figure 6.5:** Calculated flow distributions for a 30 μL/min main channel feed rate. The deviation from ideal uniform flow is shown for each of the seven side channels. Several possible pressure-drop channel lengths ( $L_s$ ), hydraulic diameters ( $d_h$ ), and total feed rates ( $\Sigma F_n$ ) are shown.

**Table 6.1: Side Channel Pressure Drops<sup>†</sup>**

$L_s$	$d_h$	$\sum F_n$	$\frac{\Delta P_{O1}}{\Delta P_{17}}$	$\frac{\Delta P_{O2}}{\Delta P_{17}}$	$\frac{\Delta P_{O3}}{\Delta P_{17}}$	$\frac{\Delta P_{O4}}{\Delta P_{17}}$	$\frac{\Delta P_{O5}}{\Delta P_{17}}$	$\frac{\Delta P_{O6}}{\Delta P_{17}}$	$\frac{\Delta P_{O7}}{\Delta P_{17}}$
7	90	14	1.94	2.08	2.23	2.39	2.57	2.75	2.94
7	90	7	0.846	1.00	1.16	1.32	1.49	1.67	1.85
7	60	14	11.6	11.7	11.9	12.0	12.2	12.38	12.58
7	60	7	6.16	6.32	6.48	6.64	6.81	6.99	7.17
14	50	14	49.4	49.5	49.67	49.8	50.0	50.2	50.4
14	50	7	27.0	27.2	27.4	27.5	27.7	27.9	28.0

<sup>†</sup>Reported relative to main channel pressure drop ( $\Delta P_{17}$ ). Channel length  $L_s$  is in cm, channel hydraulic diameter  $d_h$  is in  $\mu\text{m}$ , and total side channel flow rate is in  $\mu\text{L}/\text{min}$ . Flow distributions for each case are shown in figure 6.5. Initial main channel flow rate is  $30\mu\text{L}/\text{min}$  in all cases.

### 6.2.2 Reactor Characteristics

The microreactor design incorporating multiple feeder channels is shown in figure 6.6. The reactor was fabricated using the same process outlined in Chapter 4, and the device is similarly divided into two temperature zones for reaction and quench. Unlike the design discussed in Chapters 4 and 5, fresh precursors are added at several streamwise positions along the entire length of the main channel. Therefore, periodic bends are present throughout the entire length of the reaction channel to ensure that the freshly injected precursor streams are well mixed across the entire cross section. Two side channel manifolds (blue in the diagram) are present, one on each side of the main channel, to allow for different reactants to be added at different rates. As prescribed by the results of the previous section, each side channel is 140 cm in length and has a hydraulic diameter of  $50\mu\text{m}$ . The length of the side channels was accommodated on the device through the use of multiple windings as shown in the photographs.

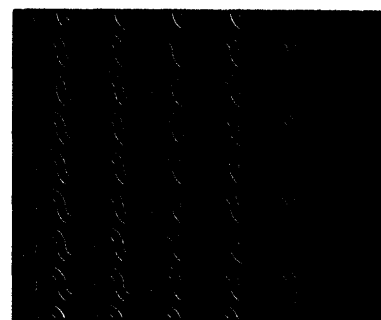
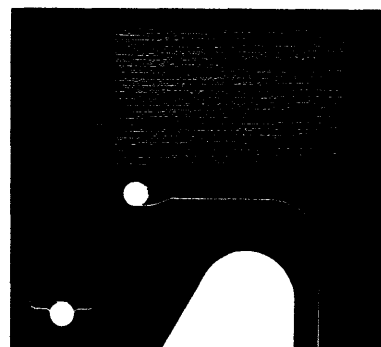
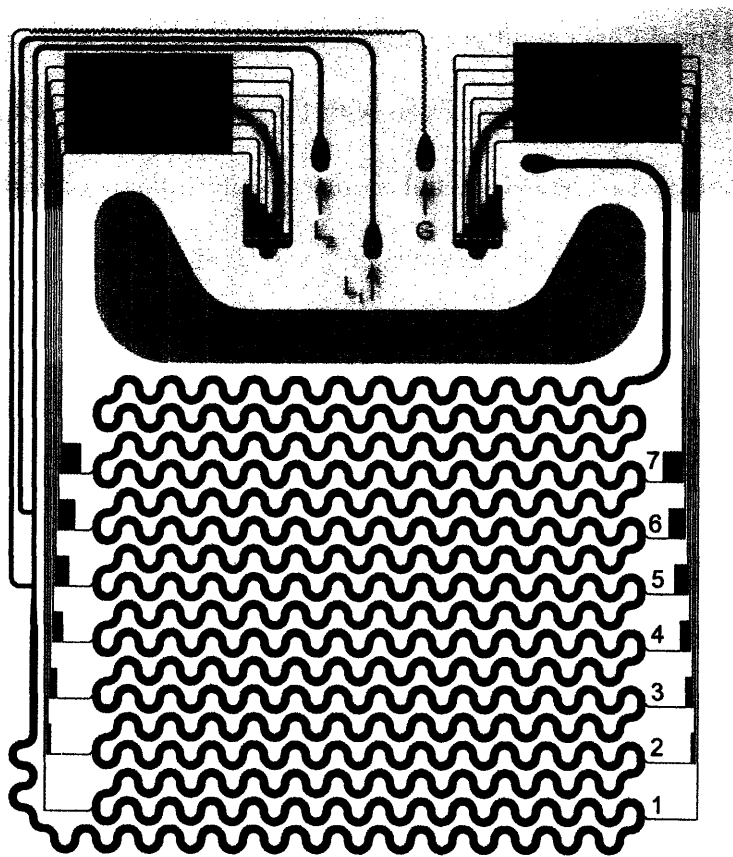


**Figure 6.6:** Microreactor design with two feeder channels manifolds (blue) for adding precursors into the main stream. Each channel has a length of 14 cm and hydraulic diameter of  $\sim 50\mu\text{m}$ . The main reaction channel (black) is  $\sim 1\text{m}$  long and has a hydraulic diameter of  $\sim 400\mu\text{m}$ . Akin to the design used in Chapters 4 and 5, two temperature regions (orange and blue) are maintained on the chip. A through etch region (gray) provides insulation between the two regions. The inlet numbering shown is used in the flow distributions measurement in Section 6.2.3.

### 6.2.3 Design Validation: Measuring the Flow Distribution

The performance of the side channel manifolds were validated by flowing a tracer solution in the channels and then measuring the concentration at various positions along the main channel. However, under actual segmented flow conditions, simply imaging a single fluorescent tracer is insufficient for extracting flow uniformity data. Even with time-averaging, the spatial and temporal variations in signal intensity can be substantial as the gas and liquid slugs pass through the field of view. Therefore, a two color measurement was used in which a red-fluorescing dye was present in both the main and side channel streams and served as an internal standard. The internal standard also helps to reduce the influence of spatial nonuniformity in the excitation spot and the channel depth (which results from the DRIE process). A green dye was added to the side channel stream, and the ratio of green-to-red emission intensity served as the analytical signal. For the green and red dyes, CdSe NCs of the appropriate size were used (prepared in the batch process). The optical densities of the final tracer solutions were low enough so that the measured analytical signal would be proportional to the concentration. The NCs were excited using a 514 Ar<sup>+</sup> laser defocused to a ~3 cm wide spot on the device. The fluorescence then passed through a filter to remove either green or red emission before being imaged onto a TE-cooled CCD camera (Micromax). For all of the measurements, either hexane or ethanol was used as the solvent for the NCs, and air used as the segmenting gas. A representative image of the green fluorescence during device operation is shown in figure 6.7.

The image processing steps required to extract the ratio signal at each of the seven streamwise positions are summarized in figure 6.8. Figures 6.8a and 6.8b show time-averaged fluorescence from the green and red NCs, respectively. After subtracting the background and



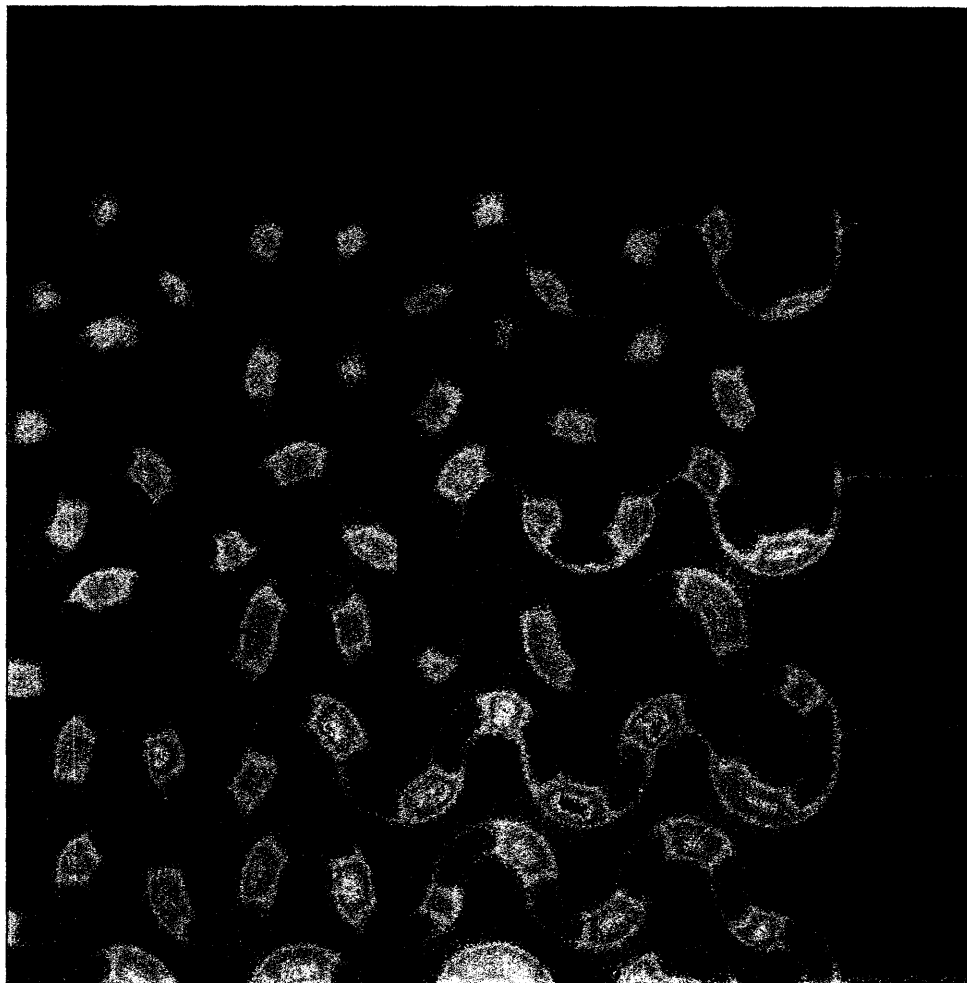


**Figure 6.7:** False-color fluorescence image used for measuring the flow distribution. Red-emitting NCs serve as an internal standard and are present in the gas-ethanol segmented flow in the main channel and in the feeder streams on the right. Green-emitting NCs are continuously injected into the main stream from the right. For this image, a filter was present so that only fluorescence from the green NCs in solution is observed.

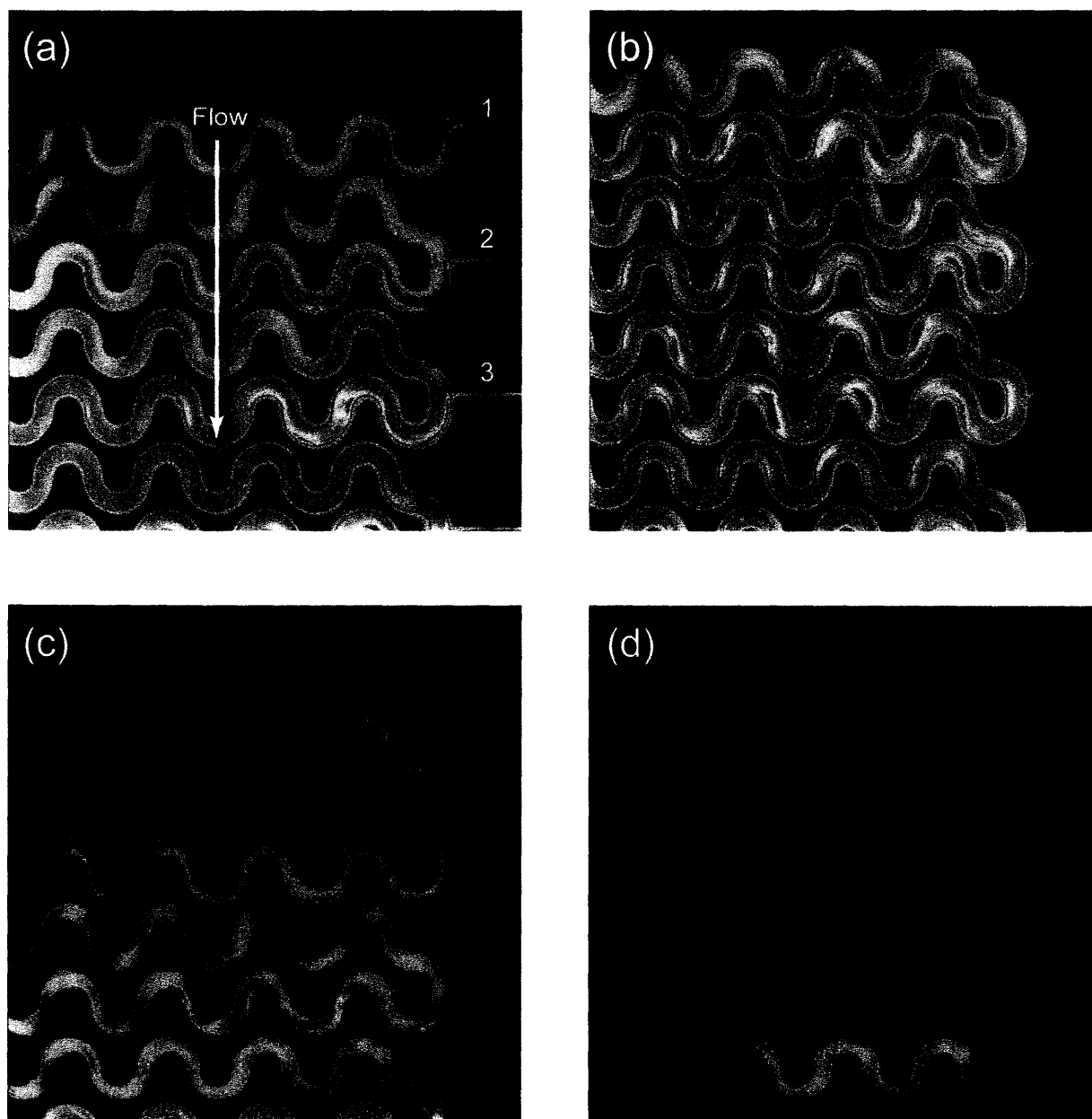


**Figure 6.8:** Sequence of image analysis steps used to determine the flow distribution. (a) Time-averaged green fluorescence image of the reactor. (b) Time-averaged red fluorescence image. After background subtraction and alignment, the ratio of green to red was taken and shown in (c). The main channel region downstream from inlet 3 was extracted from (c) and another filtering step was performed. The average intensity in this region (d) is proportional to the aggregate green tracer concentration resulting from the upstream feeder channels (inlet 1, 2, and 3).

aligning the two images, the green image was divided by the red one. Regions which were not part of the reaction channel were removed, and the ratio image is shown in figure 6.8c. Then, the region of interest (ROI) was extracted, and a final filtering step was performed to remove optical artifacts at the channel borders. In figure 6.8d, the ROI shown is the section of the main channel downstream from the feeder channel 3. Finally, the average fluorescence intensity in this ROI was calculated. It should be noted that this experimentally measurable signal does not directly correspond to the side channel flow rate. Instead, the average intensity is proportional to the *aggregate* tracer concentration resulting from the upstream feeder channels (inlet 1, 2, and 3). This procedure was repeated for regions downstream from the other six side channels under several flow conditions. Representative results of the flow distribution measurement are shown in figure 6.9. The corresponding curves for an ideal distribution (equal flow rate in each channel) are also plotted. Within the error of the measurement, the side manifold design shown in figure 6.6 results in a very uniform distribution even at very low nominal flow rates (1.14 $\mu$ L/min per channel).

For comparison purposes and further validation of the measurement method, the results from a device with insufficiently long and narrow pressure-drop features are presented in figure 6.10. The reactor design (not shown) was similar to the one in figure 6.6 except each of the feeder channels was  $\sim 2.3$  times shorter and had larger a cross-sectional area  $\sim 3.2$  times higher. As expected, a disproportionate amount of the total side channel flow rate is distributed to the feeder channels closest to the reactor outlet. In fact, at lower flow rates, the two feeder channels closest to the main channel entrance (inlets 1 and 2) exhibited back flow *out* of the main channel and into the manifold inlet.

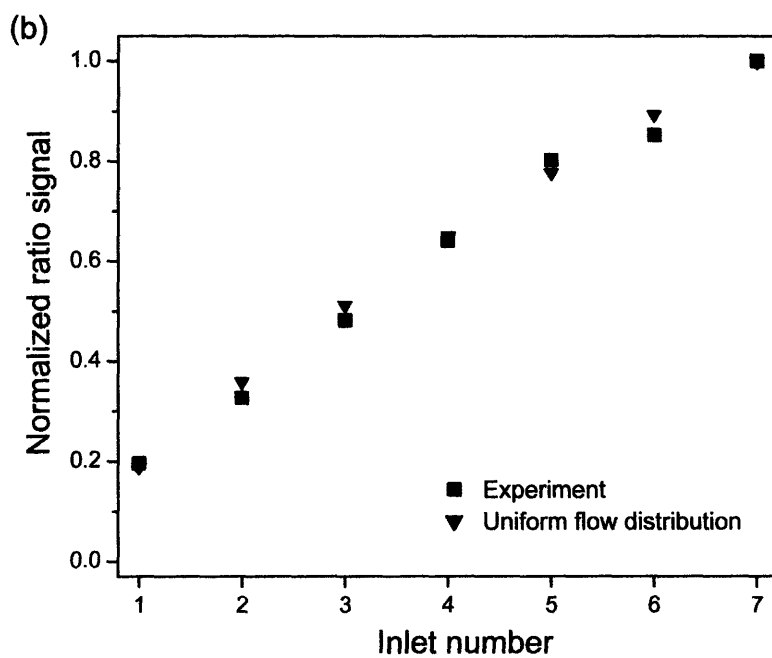
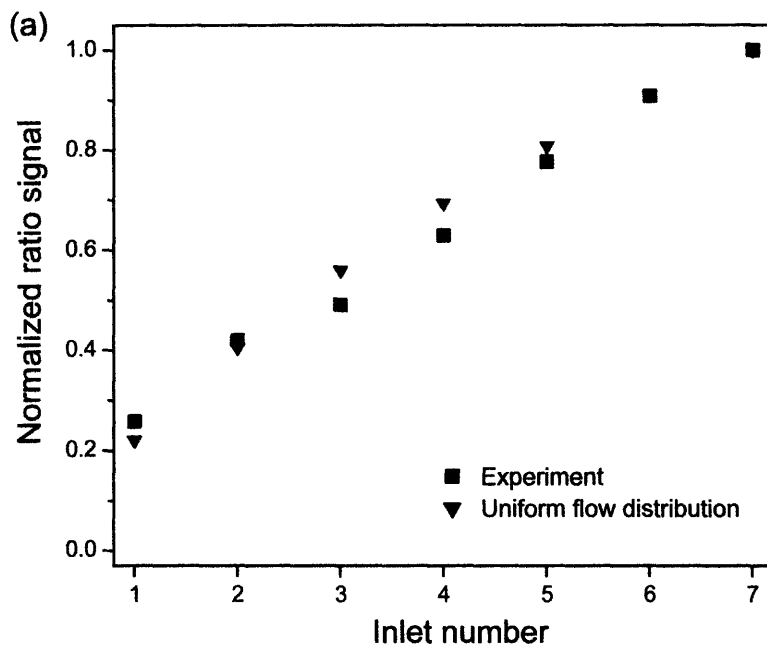


**Figure 6.9:** Comparison of measured flow results in the seven inlets with the case of ideal uniform flow distribution. The main channel feed rate was  $60\mu\text{L}/\text{min}$  for the gas and  $20\mu\text{L}/\text{min}$  in all cases. (a) Results for a total side manifold flow rate of  $14\mu\text{L}/\text{min}$  (nominally  $2\mu\text{L}/\text{min}$  per channel). (b) Results for a total side manifold flow rate of  $8\mu\text{L}/\text{min}$  (nominally  $1.14\mu\text{L}/\text{min}$  per channel).

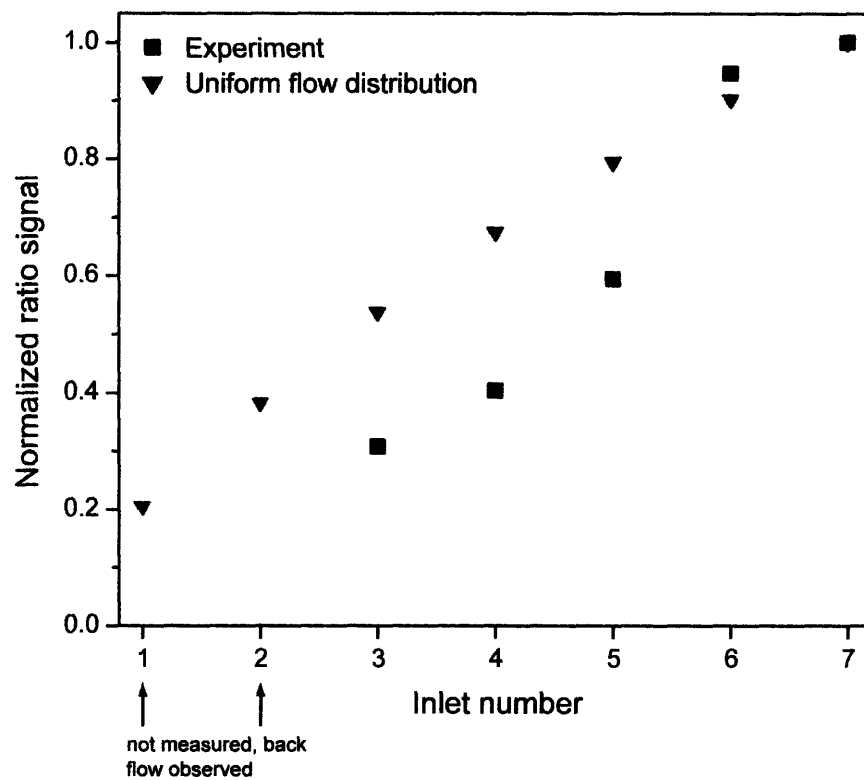


**Figure 6.10:** Flow measurement results for a device with insufficient pressure-drop features. In this device, each feeder channel was ~6 cm in length with a hydraulic diameter of ~90 $\mu$ m. The initial main channel flow rate was 50 $\mu$ L/min for the gas and 20 $\mu$ L/min for the liquid. The total flow rate in the side channels was 11 $\mu$ L/min (nominally 1.57 $\mu$ L/min per channel).

## 6.3 Application of the Design

### 6.3.1 Synthesis of Core/Shell Nanocrystals

The microreactor presented in the previous section was used to perform overcoating of CdSe NCs with a layer of a II-VI semiconductor of higher bandgap. It has been shown using batch processes that coating CdSe NCs with semiconductors such as ZnS or ZnSe results in both improved stability and increased quantum yield.<sup>6,7,9</sup> Furthermore, alloying the shell material with excess Cd during synthesis appears to reduce the lattice mismatch between the core and shell materials, enabling growth of a thicker epitaxial layer and resulting in increased sample brightness.<sup>10,16</sup> Guided by the results of such batch syntheses of heterostructured NCs, three types of core/shell materials were synthesized in the reactor: CdSe/ZnS, CdSe/ZnSe, and CdSe/Cd<sub>x</sub>Zn<sub>1-x</sub>Se.

### 6.3.2 Experimental Details

In general, the overcoating was performed by flowing a CdSe NC solution within the long meandering channel of the reactor under gas-liquid segmented flow conditions. Precursor solutions for the overcoating material were continuously delivered into the side channel manifold where they eventually mix with the main reaction stream. In performing the reactions, the concentration of the CdSe NC cores and overcoating solutions were chosen so that a reasonable range of flow rates would correspond to tuning the *nominal* overlayer thickness between ~2 to 5 monolayers of material. The nominal thickness was calculated based on the lattice parameter of the substrate (CdSe) and assumes complete reaction of the overcoating precursor solutions. In reality, the average lattice parameter of the shell probably lies between that of CdSe and the pure overcoating material, and the reaction yield is far from quantitative. The reactor was maintained

at two temperatures (reaction and quench) using a chuck similar to the one described in Chapter 5. For all of the overcoating reactions, CdSe NC cores were prepared in the batch process using the Cd(oleate)<sub>2</sub> chemistry described in Chapters 2 and 5.

For the preparation of a ZnS shell, the CdSe NC cores were first purified of excess precursor and ligands. The NCs were precipitated from growth solution by addition of acetone and the solid was isolated by centrifugation at 3900rpm. The NCs were redispersed in a minimal amount of hexane, subjected to a second acetone precipitation/centrifugation step, and finally dried under vacuum. The solution used for overcoating was prepared by dissolving a certain amount of NC solid corresponding to ~0.1mmol Cd in a solvent consisting of 5 mL squalane, 2 mL oleylamine, and 0.35 mL oleic acid. The Zn and S precursors, diethylzinc and bis-trimethylsilylsulfide, were each dissolved in a solvent consisting of 9:1 squalane:TOP (v/v). The separate Et<sub>2</sub>Zn and (TMS<sub>2</sub>)S solution streams were combined with a tee before they reached one of the side channel inlets on the device.

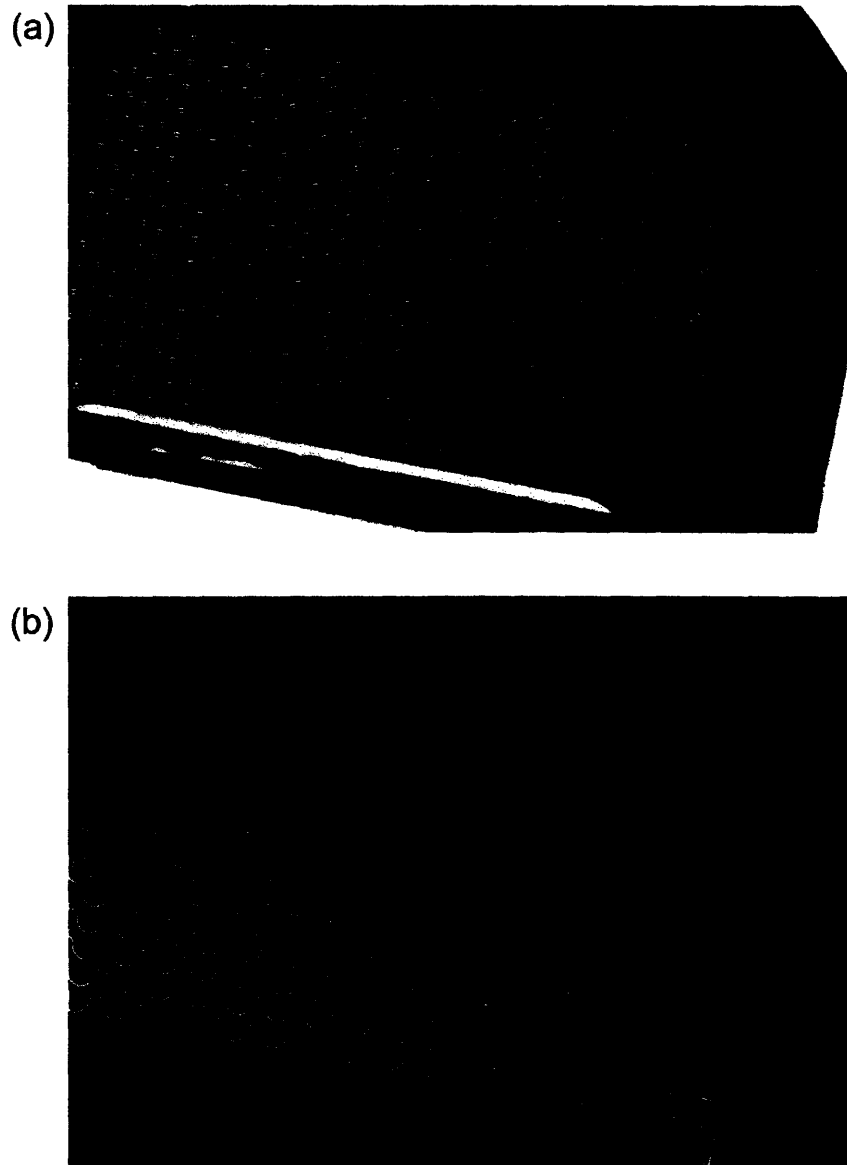
The growth of ZnSe and Cd<sub>x</sub>Zn<sub>1-x</sub>Se layers was performed using 1-octadecene (ODE) rather than squalane as the solvent. The CdSe NC cores were not processed prior to their introduction into the reactor. Instead, the raw NC growth solution was combined with excess TOPSe and ODE, and this solution was directly introduced into the main channel inlet. For the overcoating solutions, the group II precursors consisted of Zn(oleate)<sub>2</sub> and Cd(oleate)<sub>2</sub>, each dissolved in 10:3 ODE:TOP (v/v). For ZnSe overcoating, the Zn solution was delivered into one of the feeder channel manifolds where it eventually reacted with excess TOPSe in the main reaction stream. For growth of the alloyed shell, the Cd and Zn streams were combined into one before they reached one of the feeder inlets on the reactor.

### 6.3.3 Results

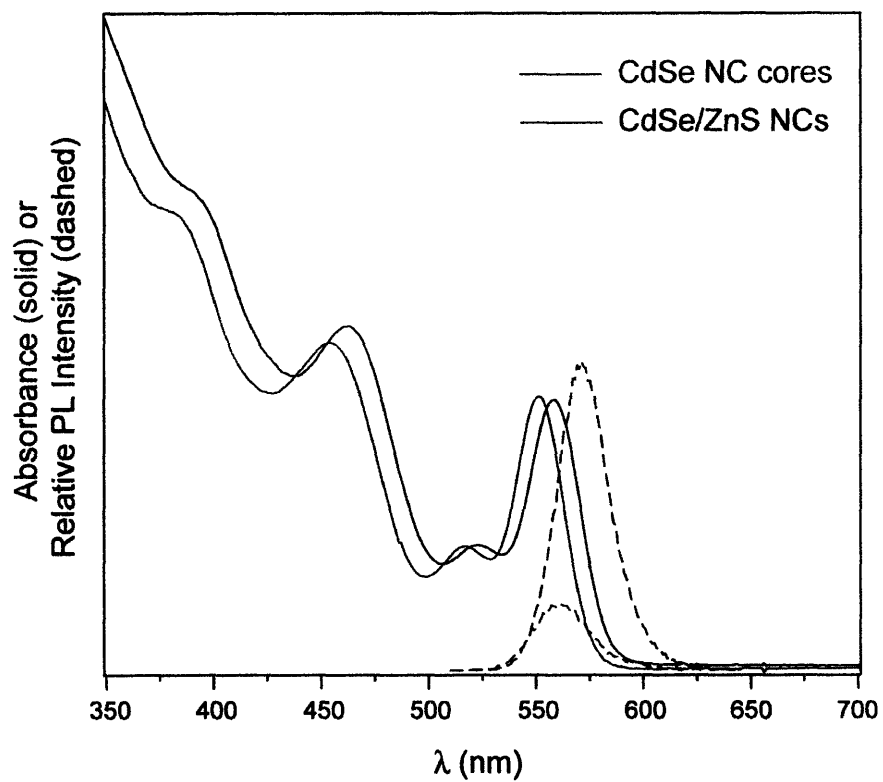
The growth of a ZnS shell on CdSe NC cores under typical flow conditions and reaction temperature is shown in figure 6.11. At the reaction temperature shown, 140°C, the NCs are still visibly fluorescent. Figure 6.11b shows the time-averaged fluorescence from the flowing reaction solution and was acquired with the reactor under continuous UV illumination. The flow rates correspond to the growth of a nominal ZnS thickness of four monolayers upon the NC surface. The solution in the channel increases with brightness as sequential layers of passivating ZnS are grown on the NCs. Figure 6.12 shows absorbance and fluorescence spectra of the cores and core/shell NCs. The spectra of the NC cores was sampled from the reactor under conditions where the side channel flows (Zn and S precursors) were turned off. The large increase in brightness in the CdSe/ZnS core/shell sample confirms that the CdSe NCs are well passivated with a layer of ZnS. Also the small red shift of the absorbance spectrum (~5 nm) is consistent with leakage of the electronic wavefunction out of the core caused by a lower potential barrier provided by the ZnS layer.

Though the microfluidic overcoating with ZnS was successful, it was found that the use of very reactive Zn and S precursors,  $\text{Et}_2\text{Zn}$  and  $(\text{TMS})_2\text{S}$ , would lead to deposition and clogging in the narrow feeder channels over time. Therefore, a more compatible chemistry for growing the shell material was implemented. Instead of diethylzinc, the less reactive zinc oleate salt was used as the Zn source. Also, TOPSe was used as the chalcogenide source rather than  $(\text{TMS})_2\text{S}$ . Zinc selenide, like ZnS, has a wider bandgap than CdSe, and overcoating with this material should provide similar results in terms of increased sample brightness and stability.





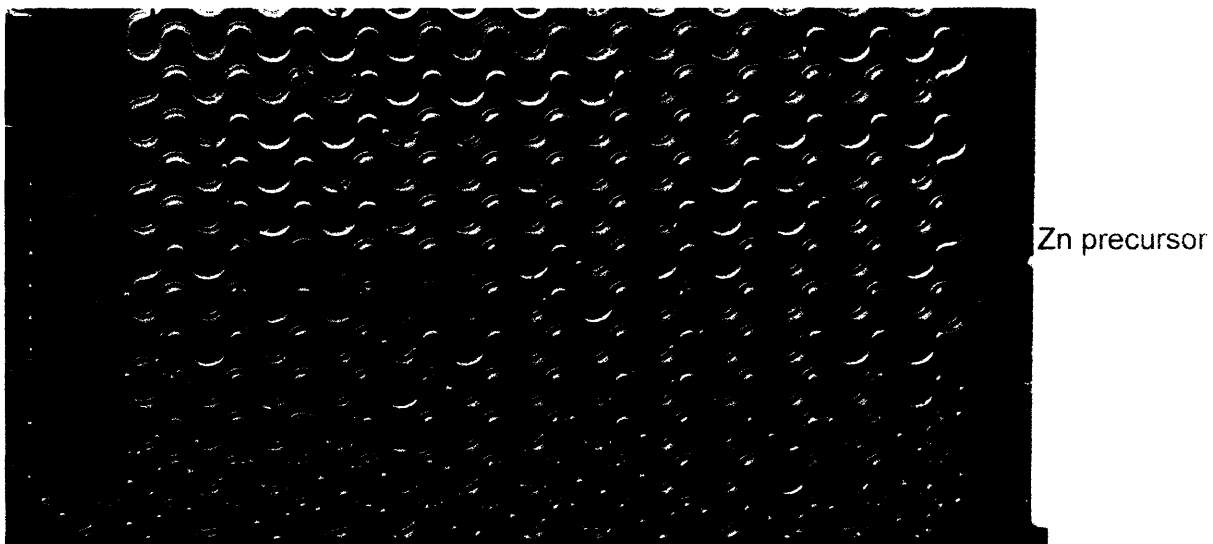
**Figure 6.11:** Synthesis of CdSe/ZnS core/shell NCs. (a) Photograph of the reactor during the overcoating reaction. Zn and S precursors enter from the right (other side manifold not used). Total reaction time was  $\sim 4$  min. Gas flow rate =  $60\mu\text{L}/\text{min}$ , Zn + S flow rate =  $8\mu\text{L}/\text{min}$ , NC cores flow rate =  $16\mu\text{L}/\text{min}$ ,  $T = 140^\circ\text{C}$ . Flow conditions correspond to growth of a nominal ZnS thickness of  $\sim 3.5$  monolayers. (b) Time-averaged image of the reactor under UV illumination showing the increasing PL as the growth of the passivating ZnS layer progresses.



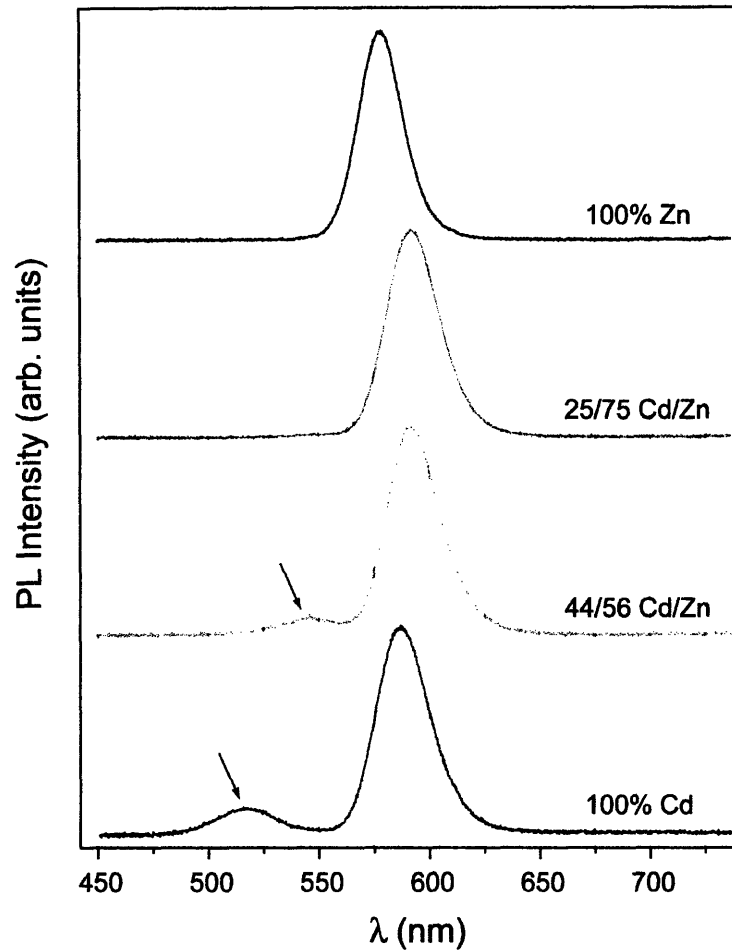
**Figure 6.12:** Absorbance and PL spectra of CdSe NC cores and CdSe/ZnS core/shell NCs in hexane.

Figure 6.13 shows a typical ZnSe overcoating performed using the microreactor. A fluorescence image of the device could not be taken due to the higher temperature required to drive the growth (240°C). The growth of an alloyed shell upon the NC cores was also performed using the reactor by addition of a Cd precursor stream to the overcoating solution. The addition of extra Cd should result in the growth of an alloyed shell ( $\text{Cd}_x\text{Zn}_{1-x}\text{Se}$ ) on the NC cores. In comparison to growth of a pure ZnSe layer, lattice strain between CdSe and the alloy should be significantly reduced. This should make it possible to grow a thicker shell with a more uniform morphology. The Cd precursor was much more reactive than the Zn precursor, and homogeneous nucleation of CdSe NCs can occur if the relative concentrations of the various reactants are not chosen correctly. The ability to independently control the relative feed rates of Cd, Zn, and cores into the reactor facilitates rapid optimization until both growth of a reasonably thick alloyed shell results and homogeneous nucleation is suppressed. This is illustrated in figure 6.14 in which increasing amounts of Cd have been added into the overcoating flow solution. At sufficiently high Cd levels, homogeneous nucleation of small CdSe NCs occurs as evidenced by the appearance of a second fluorescence peak to the blue of the main peak. From the figure, a concentration of approximately 25% appears to be the maximum amount of Cd allowable before onset of homogeneous nucleation, and this concentration was used in the alloyed overcoating results described below.

Absorbance and fluorescence spectra for the CdSe NC cores, a ZnSe overcoated sample, and a  $\text{Cd}_x\text{Zn}_{1-x}\text{Se}$  overcoated sample are shown in figure 6.15. For the latter 2 samples, concentrations and feed rates corresponded to a nominal shell thickness of three monolayers. The red shift observed for the sample with an alloyed shell is much larger than that of the sample



**Figure 6.13:** Photograph of reactor during synthesis of CdSe/ZnSe NCs. Total reaction time was  $\sim 4$  min. Gas flow rate =  $20\mu\text{L}/\text{min}$ , CdSe NC + TOPSe flow rate =  $12\mu\text{L}/\text{min}$ , Zn solution flow rate =  $8\mu\text{L}/\text{min}$ .  $T = 240^\circ\text{C}$ . Flow conditions correspond to nominally  $\sim 3$  monolayers of ZnSe.



**Figure 6.14:** Photoluminescence spectra of core/shell samples prepared with increasing amounts of Cd in the feeder channel streams. The total group II molar flow rate (Zn + Cd) was kept constant at  $8\mu\text{L}/\text{min}$ . The other conditions are identical to those in figure 6.13. Homogeneous nucleation of small CdSe NCs at high concentrations of Cd is evidenced by the appearance of a PL peak to the blue of the main peak (indicated with the arrow).

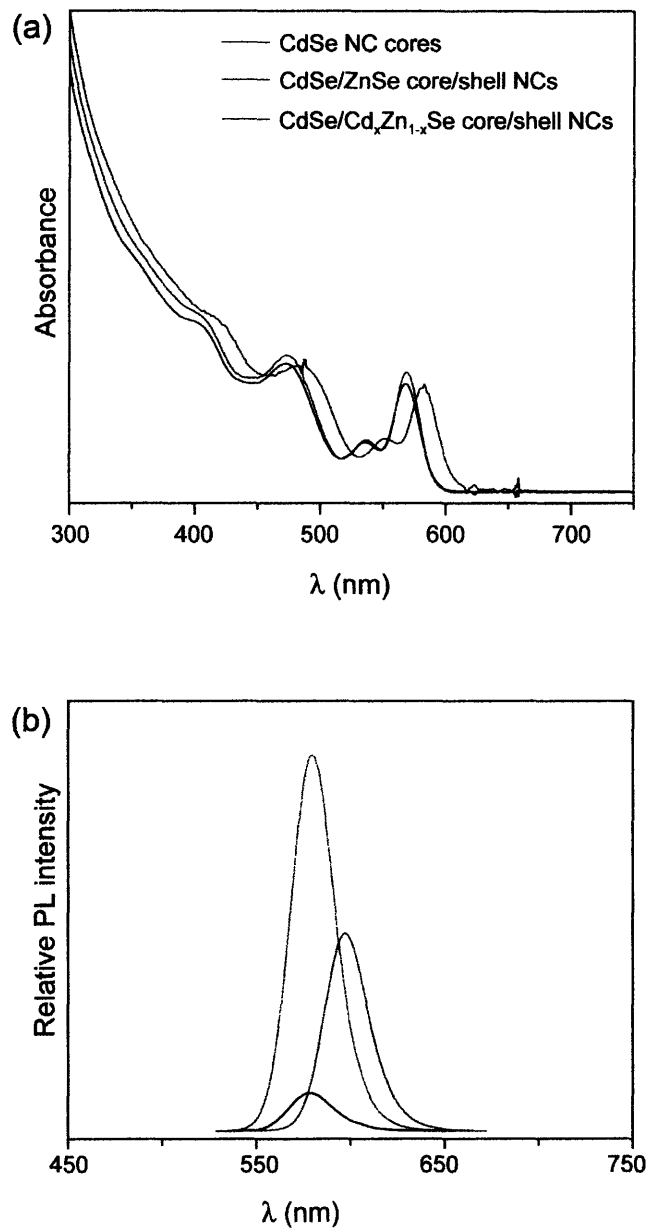


**Figure 6.15:** (a) Absorbance and (b) PL spectra of CdSe NC cores, ZnSe overcoated sample, and alloy overcoated sample in hexane. Each sample was precipitated from acetone 3 times. The resilience of the overcoated samples to processing is exhibited in the significantly higher PL compared to the NC core sample.

overcoated with pure ZnSe. This is largely due to the more pronounced leakage of the wavefunction into the shell material in the former sample. Moreover, the combination of higher reactivity of the Cd(oleate)<sub>2</sub> relative to the Zn(oleate)<sub>2</sub> and low epitaxial strain during shell growth results in a higher final shell thickness (confirmed by TEM below) and contributes to the larger red shift. In an effort to test the stability of the materials, each sample was subjected to precipitation from acetone three times before acquisition of the fluorescence spectra. The spectra (figure 6.15b) show that the two overcoated samples were able to maintain their brightness much better than the sample of NC cores after processing.

The samples represented in figure 6.15 were further characterized by transmission electron microscopy (TEM). The size distribution of each sample was then found by manually measuring the diameters of at least 300 NCs from the micrographs. The resulting size distributions and average diameters (figure 6.16) are consistent with the growth of either a ZnSe or Cd<sub>x</sub>Zn<sub>1-x</sub>Se shell upon the CdSe NC cores. The blue curve in the figure corresponds to the NC core solution which was run through the device at reaction conditions but with the feeder channel flows turned off. This was done to eliminate the possibility that any observed increase in size was due to Ostwald ripening rather than growth of a second material upon the NC surface.

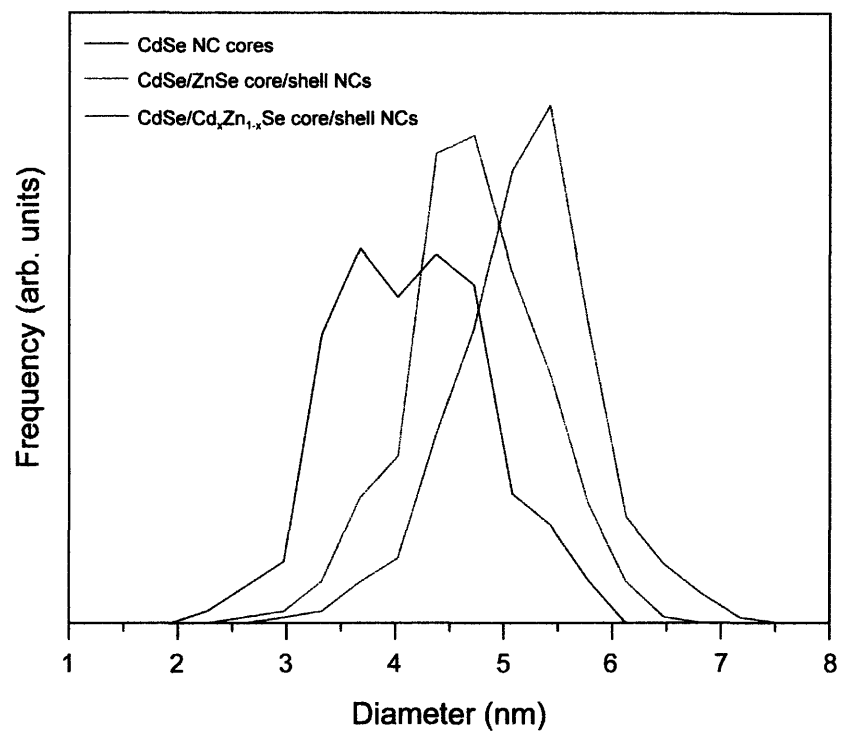


**Figure 6.16:** Size distributions based on TEM images of the three NC samples presented in figure 6.15. Each curve is based on measured diameters of more than 300 NCs.



### 6.3.4 Comments on Segmentation Quality

In general, the liquid slugs shown in figures 6.11 and 6.13 were longer and less uniform than the ones observed in the reactor presented in Chapter 5. Longer liquid slugs translates to less efficient mixing, and nonuniformity can contribute to broader size distributions. The poorer segmentation is largely a result of the lower temperatures used in the overcoating reactions which results in higher fluid viscosities and lower surface tensions. When highly reactive precursors ( $\text{Et}_2\text{Zn}$  and  $\text{TMS}_2\text{S}$ ) were used, the flow is further destabilized by boiling and gas evolution from the decomposition of these compounds. As shown in figure 6.7, very short and uniform slugs can be achieved in the reactor design with some solvents (eg. ethanol, hexane). Unfortunately, because of the temperature requirements of the synthesis, the current system is limited to a narrow class of high-boiling, viscous oils. One method of expanding the set of compatible solvents is to operate the microreactor at high pressures. This is discussed in further detail in the next chapter.

## 6.4 Conclusions

The attractive characteristics of gas-liquid segmented flow were exploited in a reactor design incorporating multiple feeder channels. Modeling and validation of the device geometry were performed in order to ensure uniform flow within each feeder channel during operation. The continuous addition of reactants enabled by this design make the device ideal for the synthesis of anisotropic NCs or growth of heterostructured NCs. As a demonstration, the growth of a higher bandgap material upon CdSe NC cores was performed using the device. Upon overcoating with such a material, significant improvement in both brightness and stability was observed.

## 6.5 References

1. Peng, X.; "Mechanisms for shape-control and shape-evolution of colloidal semiconductor nanocrystals." *Advanced Materials* **2003**, *15*, 459-463.
2. Yu, W. W.; Wang, Y. A.; Peng, X.; "Formation and stability of size-, shape-, and structure-controlled CdTe nanocrystals: ligand effects on monomers and nanocrystals." *Chemistry of Materials* **2003**, *15*, 4300-4308.
3. Peng, X. G.; Manna, L.; Yang, W. D.; Wickham, J.; Scher, E.; Kadavanich, A.; Alivisatos, A. P.; "Shape control of CdSe nanocrystals." *Nature* **2000**, *404*, 59-61.
4. Peng, Z. A.; Peng, X.; "Mechanisms of the shape evolution of CdSe nanocrystals." *Journal of the American Chemical Society* **2001**, *123*, 1389-1395.
5. Peng, Z. A.; Peng, X.; "Nearly monodisperse and shape-controlled CdSe nanocrystals via alternative routes: nucleation and growth." *Journal of the American Chemical Society* **2002**, *124*, 3343-3353.
6. Hines, M. A.; Guyot-Sionnest, P.; "Synthesis and characterization of strongly luminescing ZnS-Capped CdSe nanocrystals." *Journal of Physical Chemistry* **1996**, *100*, 468-471.
7. Dabbousi, B. O.; Rodriguez-Viejo, J.; Mikulec, F. V.; Heine, J. R.; Mattoussi, H.; Ober, R.; Jensen, K. F.; Bawendi, M. G.; "(CdSe)ZnS core-shell quantum dots: Synthesis and characterization of a size series of highly luminescent nanocrystallites." *Journal of Physical Chemistry B* **1997**, *101*, 9463-9475.
8. Cao, Y. W.; Banin, U.; "Growth and properties of semiconductor core/shell nanocrystals with InAs cores." *Journal of the American Chemical Society* **2000**, *122*, 9692-9702.
9. Reiss, P.; Bleuse, J.; Pron, A.; "Highly luminescent CdSe/ZnSe core/shell nanocrystals of low size dispersion." *Nano Letters* **2002**, *2*, 781-784.
10. Xie, R.; Kolb, U.; Li, J.; Basché, T.; Mews, A.; "Synthesis and characterization of highly luminescent CdSe-core CdS/Zn<sub>0.5</sub>Cd<sub>0.5</sub>S/ZnS multishell nanocrystals." *Journal of the American Chemical Society* **2005**, *127*, 7480-7488.
11. Aharoni, A.; Mokari, T.; Popov, I.; Banin, U.; "Synthesis of InAs/CdSe/ZnSe core/shell1/shell2 structures with bright and stable near-infrared fluorescence." *Journal of the American Chemical Society* **2006**, *128*, 257-264.
12. Kim, S.; Fisher, B.; Eisler, H.-J.; Bawendi, M.; "Type-II quantum dots: CdTe/CdSe(core/shell) and CdSe/ZnTe(core/shell) heterostructures." *Journal of the American Chemical Society* **2003**, *125*, 11466-11467.

13. Xie, R.; Zhong, X.; Basché, T.; "Synthesis, characterization and spectroscopy of type-II core/shell semiconductor nanocrystals with ZnTe cores." *Advanced Materials* **2005**, *17*, 2741-2745.
14. Peng, X. G.; Wickham, J.; Alivisatos, A. P.; "Kinetics of II-VI and III-V colloidal semiconductor nanocrystal growth: "Focusing" of size distributions." *Journal of the American Chemical Society* **1998**, *120*, 5343-5344.
15. Bird, B. B.; Stewart, W. E.; Lightfoot, E. N., *Transport Phenomena*; 2nd ed.; Wiley: New York, 2002.
16. Talapin, D. V.; Mekis, I.; Goltzinger, S.; Kornowski, A.; Benson, O.; Weller, H.; "CdSe/CdS/ZnS and CdSe/ZnSe/ZnS core-shell-shell nanocrystals." *Journal of Physical Chemistry B* **2004**, *108*, 18826-18831.



## **Chapter 7**

### **Summary and Future Opportunities**

#### **7.1 Summary**

Microfluidic reactors enable a number of improvements over conventional chemical processes including enhanced control over heat and mass transfer, lower reagent consumption during optimization, and sensor integration for in-situ reaction monitoring. Motivated by these advantages, several microreactors were designed for the synthesis of colloidal semiconductor NCs. Initially, a simple single-phase capillary reactor was developed. Mass transport limitations in the design led to the development of a gas-liquid segmented flow microreactor for synthesis of NC cores. The segmented flow approach was then used in a reactor design equipped with multiple feeder channels for the synthesis of complex NC architectures. Many of the reactor engineering and design challenges have been solved, and the microfluidic systems described in this thesis can now be expanded beyond established chemistries and proof-of-concept experiments. Some future research opportunities are outlined below.

#### **7.2 Microfluidic Synthesis of Nanocrystals Under High Pressure**

One of the principal obstacles preventing the rapid adoption of microreactors as universal platforms for NC synthesis is that there is a limited set of solvents, ligands, and precursors compatible with such a continuous flow system. In practice, the fluid delivery system upstream from the device and lines downstream from the exit are at ambient conditions. Therefore, the

reactant solutions must remain liquid over a very large temperature range ( $\sim 25^{\circ}\text{C}$  to  $\sim 300^{\circ}\text{C}$ ). This severely limits the number of chemistries which can be implemented in a microfluidic system. Current batch preparations of NCs often involve the use of reagents which are solid at room temperature. One of the major challenges in transferring these batch processes to the microscale has been finding appropriate reagent substitutes that are 1) liquid at ambient conditions but do not boil at the high reaction temperatures and 2) mutually soluble/miscible at room temperature. A simple example from the chemistries described in previous chapters provides an illustration. Given the fairly narrow class of high-boiling compounds compatible with normal pressure synthesis, it was challenging to find a suitable solvent for the metal salt precursors commonly used in NC preparations. For instance,  $\text{Cd}(\text{oleate})_2$  and  $\text{Zn}(\text{oleate})_2$  are readily soluble in a number of common (low-boiling) organic solvents but only sparingly soluble in high-boiling oils such as squalane or 1-octadecene. A significant amount of coordinating ligands (TOP or oleylamine) had to be added to dissolve these precursors. This situation is far from ideal since these ligands obviously have a strong influence on the NC nucleation and growth process, and one would like to have the flexibility of varying the type and concentration of ligands over a large range.

One way of expanding the set of NC chemistries possible with microreactor design described in the previous chapters is to perform the reactions at high pressure. At sufficiently high pressure, virtually any precursor, ligand, or common solvent can be made to remain liquid at the NC reaction temperatures. Because of the expanded range of available reagents, translating a batch NC synthesis to a high pressure microfluidic system should be straightforward, requiring only slight modification of the chemistry. Moreover, high pressure synthesis should make it possible to carry out syntheses of materials which cannot be performed

using current batch methods. From a fundamental standpoint, high pressure enables one to focus on more interesting chemical questions such as the details of the NC nucleation and growth mechanism rather than more banal concerns such as boiling in the channel or solubility issues.

In practice, almost all NC reactions are performed in the range of ~150 to 300°C. At these temperatures, an applied pressure in the range of ~10 to 60 atm is required for common organic reagents to remain liquid. This pressure range was based on figure 7.1 which shows the vapor pressure of several common solvents with temperature. The vapor pressures were estimated using a three parameter empirical expression (Antoine equation):

$$\log_{10} P = A - \frac{B}{T + C} \quad \text{Eq. 7.1}$$

The coefficients (*A*, *B*, and *C*) are tabulated for many compounds in a number of references.<sup>1,2</sup> The glass brazing technique described in Chapter 4 is sufficiently robust to maintain the fluidic seals at these pressures. Furthermore, the standard HPLC fittings used in the fluid lines and the anodic bond sealing the device can withstand very high pressures. A diagram of a high pressure setup for NC synthesis is shown in figure 7.2. The fluid delivery, reaction, and collection portions of the system are maintained at high pressure with a N<sub>2</sub> tank. Precursor solutions are loaded in steel syringes and delivered using a high-pressure pump (Harvard Apparatus). A switching valve connected to a reservoir containing several vials allows for the sampling of multiple flow conditions without breaking pressure.

To demonstrate the feasibility of performing NC chemistries with common organic solvents, CdSe NCs were synthesized using the setup in figure 7.2. The reactor design was similar to the one presented in Chapter 4 except in this case both the inlets and outlet were placed

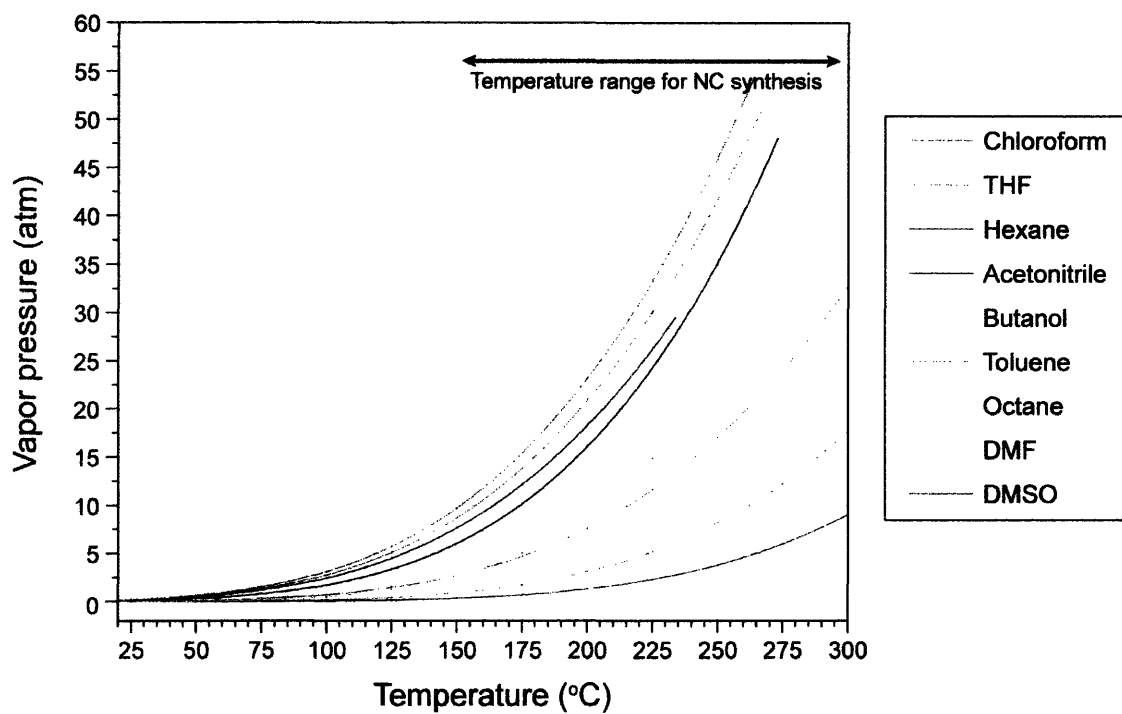


**Figure 7.1:** Variation of vapor pressure with temperature for a selection of common solvents. For some of the solvents, the Antoine equation is not accurate for the higher temperature ranges, and plots have been truncated accordingly.



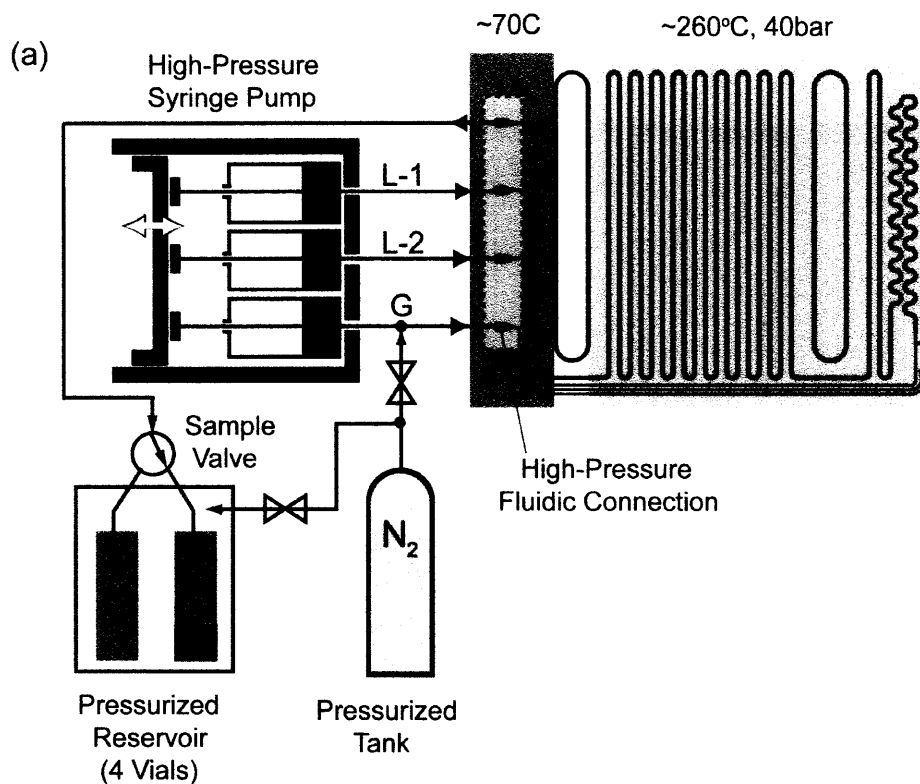


**Figure 7.2:** (a) Diagram of experimental setup for high pressure synthesis. A high-pressure syringe pump is used to deliver the fluids. Glass brazed connections described in Chapter 4 are used to interface to the device. A switching valve connected to a reservoir is used to take multiple samples at different conditions without breaking the pressure. (b) Photograph of the experimental setup.

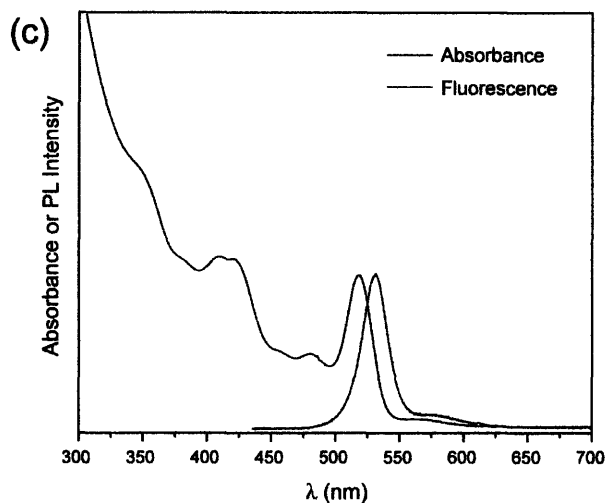
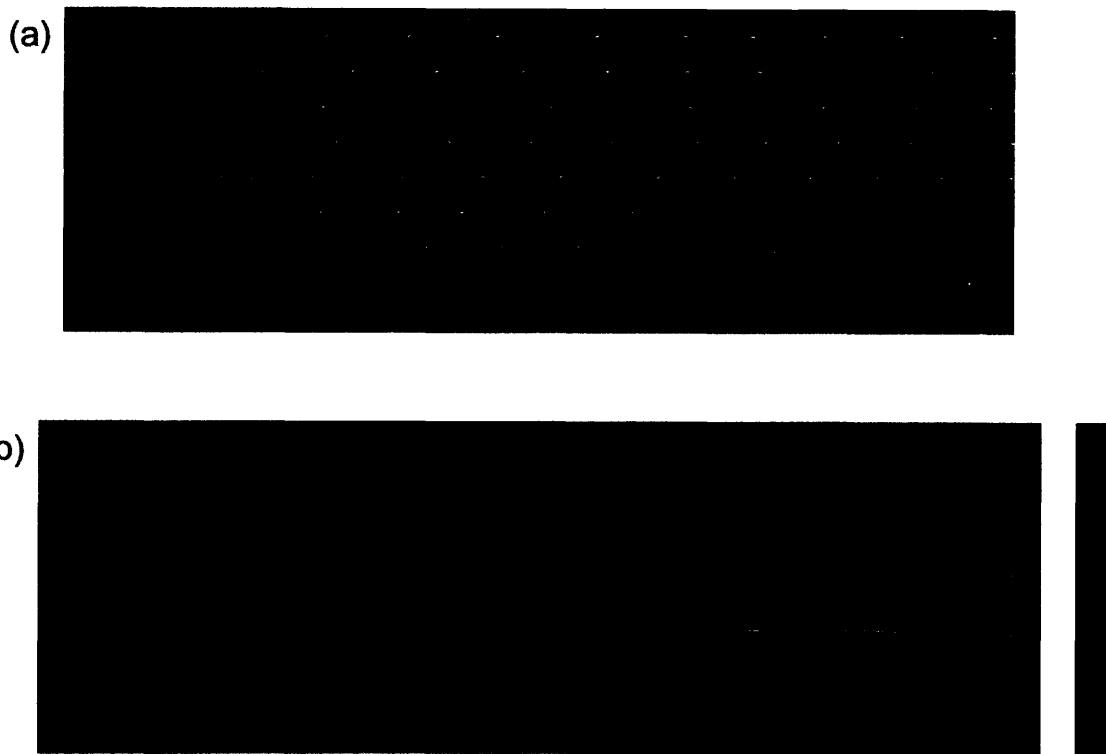


**Figure 7.3:** Synthesis of CdSe NCs in toluene at 260°C and 40 atm.  $L_{Cd} = 14\mu\text{L}/\text{min}$ ,  $L_{Se} = 14\mu\text{L}/\text{min}$ ,  $L_{gas} = 14\mu\text{L}/\text{min}$ . The residence time was  $\sim 4$  min. The inlet/outlet section was cooled by immersion in a water bath. (a) Photo of the heated section of the device during synthesis. (b) Time-exposure photograph of the cooled outlet region under UV excitation. (c) Absorbance (blue) and PL (red) spectra of the NCs in toluene.

in the cooled section of the device. The Cd(oleate)<sub>2</sub>/TOPSe chemistry described in previous chapters was followed except toluene was used in place of squalane (The normal boiling point of toluene is 110°C). The results for a synthesis performed in toluene at 260°C and 40 atm are shown in figure 7.3. An image of the heated region of the device during operation is shown in figure 7.3a, and the cooled outlet region under UV irradiation is shown in figure 7.3b. As shown in figure 7.3c, the NCs synthesized at high pressures are comparable in quality to those prepared in previous chapters (narrow emission and well resolved absorbance features).

### **7.3 Synthesis of New Materials and Mechanistic Studies**

A high-pressure system will not only make it possible to quickly adopt the numerous batch preparations of NCs to a microfluidic system, but such a system will also facilitate the development of new NC chemistries. There are certainly numerous NC materials which have yet to be synthesized, but two in particular, InSb and PbSe, come to mind as potential candidates for immediate implementation in microreactor. The former is of interest because, owing to the small electronic effective mass of InSb, the effective bandgap of InSb NCs can theoretically be tuned over a large spectral window ranging from the visible to the near infrared. However, bright and monodisperse samples of InSb NCs have yet to be reported using the batch process. A high pressure system coupled with a microfluidic reactor similar to the one presented in Chapters 4 and 5 could be used to develop and quickly optimize reaction conditions for the preparation of high quality InSb NC cores. The second material, PbSe NCs, has been successfully synthesized with low polydispersity and over a range of sizes corresponding to emission in the near infrared.<sup>3</sup> However, the instability of PbSe NCs necessitates overcoating the NC cores with a material of higher bandgap, and such a core/shell material has yet to be reported. A microfluidic system

described in Chapter 6 under high pressure could be employed to screen possible PbSe overcoating chemistries.

As mentioned in Chapter 1, the well-defined mass and heat transfer enabled by a microfluidic system makes it possible to extract kinetic information on NC nucleation and growth. One particular advantage of the reactors developed in Chapters 4 to 6 is that segmented flow provides a means of controlling the mass transfer rate during NC reaction. Varying the flow rates and slug length provides a means of varying the mass transfer component of the NC formation mechanism. As shown for the case of CdSe NCs, the growth kinetics can be strongly influenced by mass transport of monomers to the particle surface. Moreover, microscale segmented flow is still laminar, which facilitates the analysis of the transport properties and kinetic data.

#### **7.4 Multi-Stage Operation**

The reactor designs presented in the previous chapters broadly represent two types of NC reactions: 1) synthesis of NC cores and 2) growth upon existing cores of a second material or growth into an anisotropic morphology. An obvious future direction would be to operate several different reactor designs in series. Bandgap engineering could be performed by building up complex NC architectures in such a multi-stage setup. For instance, synthesis of NC cores would be performed in the first stage. The cores would then flow through a series of overcoating units where layers of different semiconductor materials are grown within each unit. One challenge will be to maintain uniform segmentation in each stage as the flow will be disrupted as a result of discontinuities in temperature and channel geometry between stages. It will probably be necessary to incorporate a gas-liquid separator<sup>4</sup> at the exit of each stage to reduce the flow to

single phase. Then the gas segmentation can be reintroduced into the flow at reaction conditions within the entrance region of each reactor unit.

A concept related to multi-stage operation is the integration of the many components and reactor units into a single system. Developing a more flexible and user friendly apparatus for fluid delivery, heating, and cooling would greatly facilitate the screening of reaction parameters. In particular, a compact system of delivering many different types of liquids (eg. multiple reservoirs driven by a static gas pressure rather than syringe pumps) would be a considerable improvement over the current system. This system would make it possible, *during a single run*, to screen through the complete set of relevant reaction parameters: temperature, time, individual concentrations, and different types of precursors and ligands. Coupling of optical fibers, either in situ or in-line, would also be especially useful for studying NC chemistries. For a large number of NC materials, linear optical (or near-IR) spectroscopy reveals a great deal of information about the reaction (eg. average size, size distribution, yield, etc.). The online monitoring can then be combined with a feedback algorithm which changes the relevant reaction parameters until the optimum product quality is obtained.

## 7.5 References

1. Reinhard, M.; Drefahl, A., *Handbook for Estimating Physicochemical Properties of Organic Compounds*; Wiley: New York, 1999.
2. Yaws, C. L.; Narasimhan, P. K.; Gabbula, C. *Yaws' Handbook of Antoine Coefficients for Vapor Pressure (Electronic Edition)*; Knovel: Norwich, NY, 2005. Available at <http://www.knovel.com/knovel2/Toc.jsp?BookID=1183&VerticalID=0>.
3. Murray, C. B.; Sun, S. H.; Gaschler, W.; Doyle, H.; Betley, T. A.; Kagan, C. R.; "Colloidal synthesis of nanocrystals and nanocrystal superlattices." *IBM Journal of Research and Development* **2001**, *45*, 47-56.

4. Günther, A.; Khan, S. A.; Thalmann, M.; Trachel, F.; Jensen, K. F.; "Transport and reaction in microscale segmented gas-liquid flow." *Lab on a Chip* **2004**, *4*, 278-286.

## Appendix A

### Deep Reactive Ion Etching Parameters

#### A.1 Introduction

The most important steps in the wafer fabrication process described in Chapter 4 involve deep reactive ion etching (DRIE) of the channel features. DRIE is suited for the microreactor process because the technique makes it possible to fabricate straight trench walls (anisotropic etching) and very high aspect ratios features in silicon. The plasma etch is performed using a time-multiplexed Bosch process (in contrast to cryogenic DRIE).<sup>1-3</sup> In this process, the substrate is subjected to alternating cycles of etching and sidewall passivation. Selective passivation prevents isotropic etching of the substrate and enables control of the feature profile. For the system used to prepare the microreactors (Surface Technology Systems Multiplexed ICP), the etching plasma was generated by flowing SF<sub>6</sub> into a chamber containing an inductively coupled plasma (ICP). Selective passivation of the sidewalls was accomplished by flowing C<sub>4</sub>F<sub>8</sub> into the chamber which forms a fluorocarbon polymer on the silicon surface. The wafer was also biased with respect to the plasma to impart a net flux of ions toward the substrate surface. Clearly, there is a large number of chamber parameters to consider including chamber pressure, electrode power, gas flow rates, and cycle times. The influence of such parameters on the trench profile, etch rate, and depth uniformity have been investigated in great detail and will not be specifically repeated here.<sup>4,5</sup> Rather, this section will focus on a practical approach to two common DRIE issues that arose during the reactor fabrication process.

## A.2 Formation of Silicon Grass

A common problem which can occur during DRIE is the formation of “silicon grass” or “black silicon” at the bottom of the etched feature. Silicon grass consists of a field of very narrow spikes which appear black to the eye (figure A.1) and are obviously undesirable. This problem arises due to micromasking of the etched area by native oxide, residual photoresist, or other contaminants during DRIE.<sup>6</sup> Therefore, great care was taken during preceding photolithography and wet oxide etch steps to ensure a clean etch surface. However, even with a pristine wafer, redeposition of material during the plasma etch or masking by chamber contaminants would often still result in formation of silicon grass. One method to minimize the formation of these spikes is to control the channel etch profile. Three types of profiles are possible: positive taper, where the bottom of the channel is narrower than the top; perfectly vertical sidewalls; and negative taper, where the bottom of the channel is wider than the top. Though a perfectly vertical trench profile may be ideal from an aesthetic standpoint, grass formation can still pose a problem under these conditions. The problem becomes worse with a more positively tapered profile. Negative taper, on the other hand, greatly reduces the formation of grass.<sup>6</sup> This makes intuitive sense since any small spikes which begin to form on the bottom of the channel will be rapidly undercut and removed when a negatively sloped etch is used. Therefore, it is recommended that the DRIE be performed with a slightly negative undercut, resulting in a smooth reactor channel bottom and preserving an approximately rectangular channel cross-section.



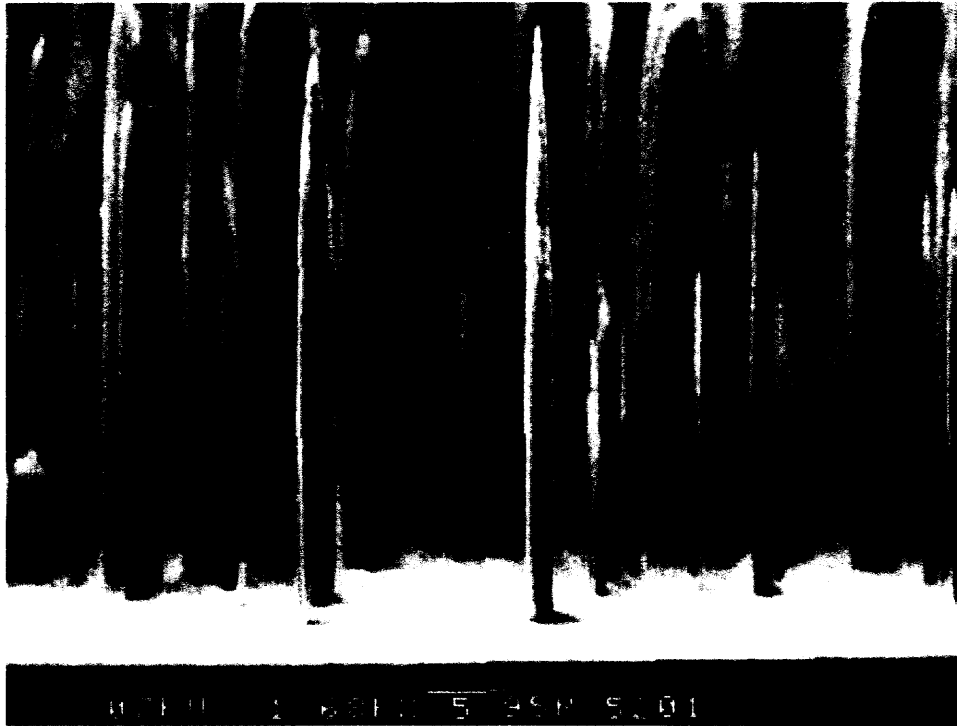


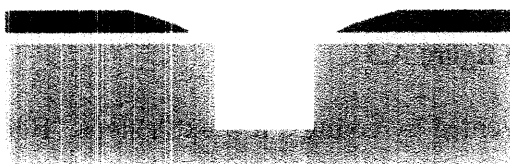
**Figure A.1:** Scanning electron micrograph of silicon grass. From reference 6.

In theory, a set of optimal parameters (gas flow rate, power, cycle time, etc.) could be found using a test wafer to achieve the desired trench profile. However, the etch profile and etch rate are also dependent on the feature size, mask layout, and total etch area. For instance, it was not uncommon to observe, for a single DRIE recipe, a very smooth feature bottom during etching of the back side inlet pattern but large amounts of black silicon during etching of the main channel layer (front side). Therefore, for each mask layer, a practical approach to optimizing chamber conditions for minimal grass formation can be adopted. This involves visual monitoring of the wafer throughout the process. Then, upon observation of any incipient black silicon, the gas flow rates and power should be varied to bias the etch toward a more negative undercut. In general, the change to a more desirable etch profile can be accomplished using some combination of lowering the SF<sub>6</sub> flow rate, increasing the SF<sub>6</sub>/C<sub>4</sub>F<sub>8</sub> ratio, or increasing electrode power.<sup>4</sup>

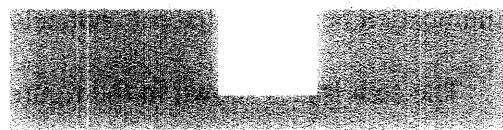
### **A.3 Removal of Photoresist**

DRIE conditions for channel etching are typically very selective for silicon, but some etching of the protective photoresist still occurs. Usually, receding of the photoresist layer is most pronounced near regions of exposed silicon (figure A.2), and inadequate adhesion of photoresist can exacerbate this overetching problem. An additional layer of patterned thermal oxide layer is present underneath the photoresist to provide extra protection from the plasma. For processes where only a single etch layer is required, this is usually sufficient to ensure preservation of good channel features near the surface of the wafer. However, the microreactors were fabricated using a nested mask process in which a naked oxide layer is used as the etch

Profile after first deep etch (400 $\mu\text{m}$ )



Damaged oxide is now exposed during the second etch



Photoresist

Oxide

Silicon

**Figure A.2:** Etching of photoresist and oxide around patterned features during DRIE of main channel pattern. The nested oxide mask, which serves as the etch stop for the second DRIE step, is damaged. Drawing is not to scale. Actual thickness are: photoresist = 10 $\mu\text{m}$ , oxide = 0.5 to 1.0 $\mu\text{m}$ , silicon = 650 $\mu\text{m}$ .

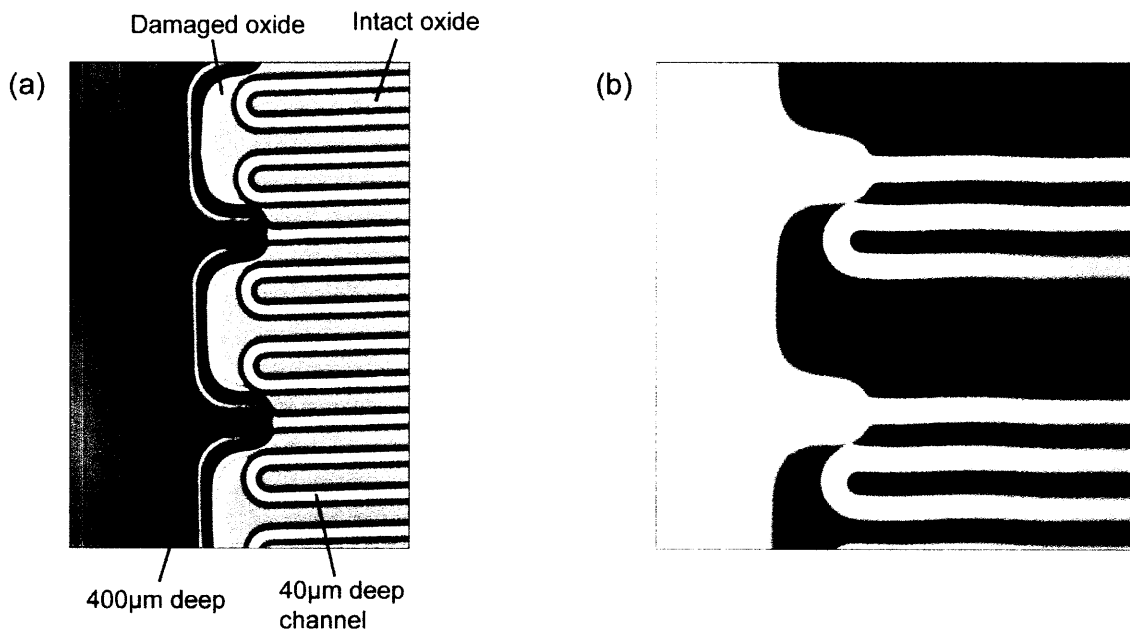


**Figure A.3:** (a) Optical micrograph showing how damage to the oxide mask results in cross-talk between closely spaced channel features. (b) Confocal image of a fluorescent dye solution (white) in the channel manifold.

stop. Degradation of the photoresist and oxide during the first DRIE step resulted in insufficient protection of the wafer during the etching of the side channel patterns. For closely spaced features such as the pressure-drop manifolds described in Chapter 6, this can lead to communication between adjacent channels as shown in figure A.3.

The etch issues shown in the figure can be prevented by taking a few extra steps. Before performing DRIE, it is important to inspect each photoresist-coated wafer under a microscope to check for good adhesion to the substrate especially near patterned features. If necessary, adhesion can be improved by performing an extra wafer clean with piranha prior to spin coating the photoresist. Also, a thick oxide layer ( $\sim 1\mu\text{m}$ ) should be grown on the wafer to afford extra protection from degradation of the areas around the pattern. The thicker layer (compared to the  $0.5\mu\text{m}$  grown during back side patterning) should provide sufficient protection during the two level etch process with a negligible loss in mask fidelity.

#### A.4 References

1. Douglas, M. A. "Trench etch process for a single-wafer RIE dry etch reactor." *US Patent 4,784,720*; 1988.
2. Douglas, M. A. "Trench etch process for a single-wafer RIE dry etch reactor." *US Patent 4,855,017*; 1989.
3. Laermer, F.; Schilp, A. "Method of anisotropically etching silicon." *US Patent 5,501,893*; 1996.
4. Ayón, A. A.; Braff, R.; Lin, C. C.; Sawin, H. H.; Schmidt, M. A.; "Characterization of a time multiplexed inductively coupled plasma etcher." *Journal of the Electrochemical Society* **1999**, *146*, 339-349.
5. Blauw, M. A.; Zijlstra, T.; van der Drift, E.; "Balancing the etching and passivation in time-multiplexed deep dry etching of silicon." *Journal of Vacuum Science and Technology B* **2001**, *19*, 2930-2934.

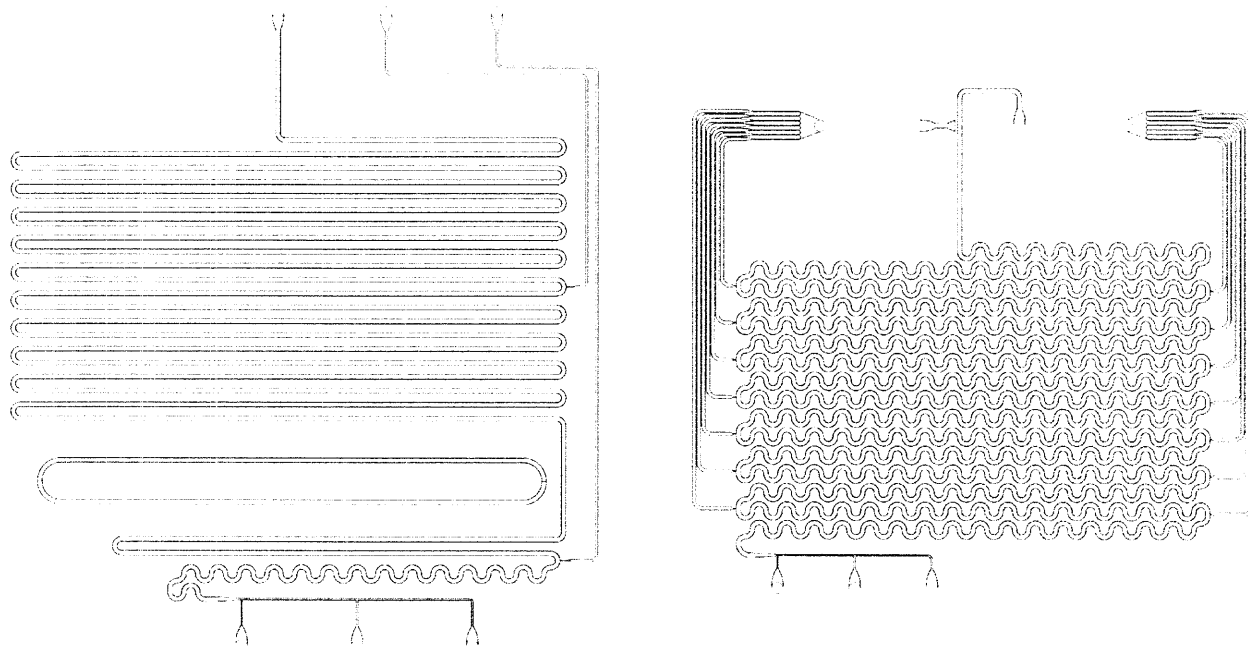
6. Jansen, H.; de Boer, M.; Legtenberg, R.; Elwenspoek, M.; "The black silicon method: a universal method for determining the parameter setting of a fluorine-based reactive ion etcher in deep silicon trench etching with profile control." *Journal of Micromechanics and Microengineering* **1995**, 5, 115-120.

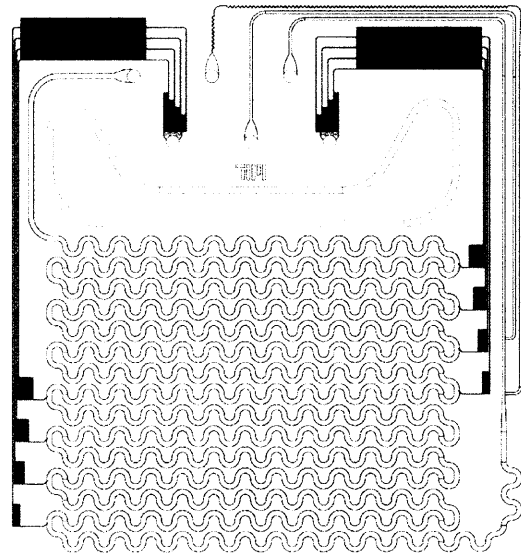
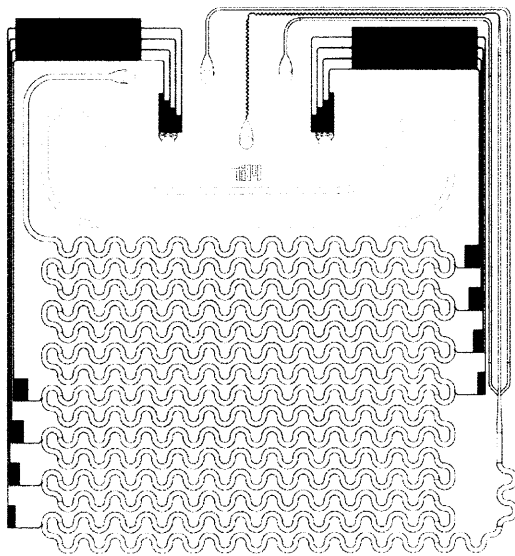
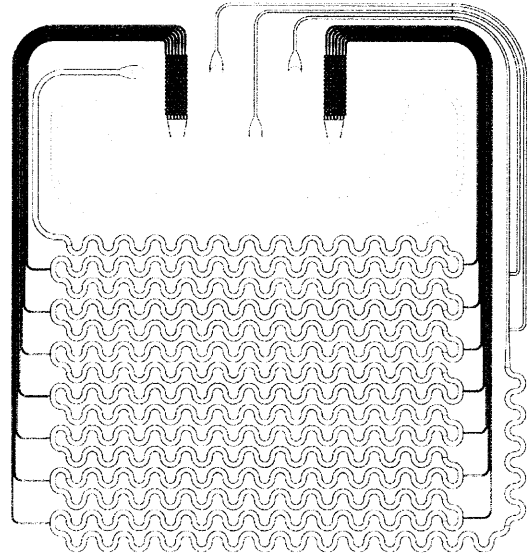
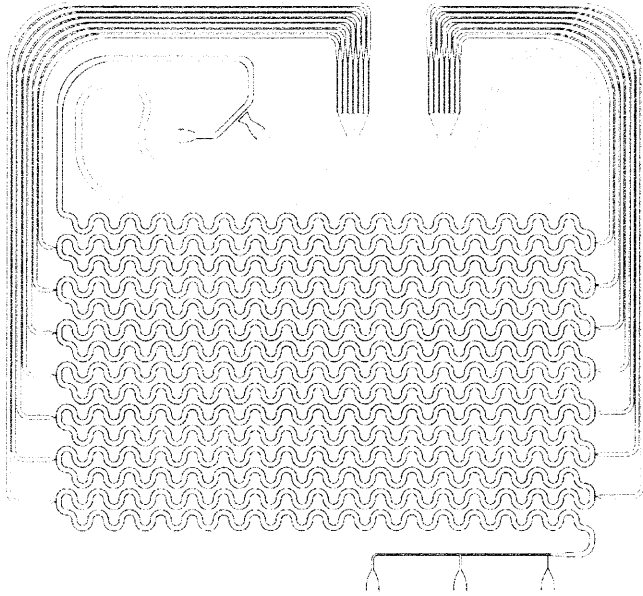


## Appendix B

### Other Reactor Designs

Several microreactors were fabricated but not presented in previous chapters. A listing of these designs is presented in this appendix. The following color key applies: black = 400 $\mu$ m deep etch, blue = 40-50 $\mu$ m deep etch, red = through etch. In all of the designs, the main reaction channel was approximately 1 meter long and 400 $\mu$ m wide.







# Brian K.H. Yen

77 Massachusetts Ave.  
MIT Chemistry, 18-080  
Cambridge, MA 02139

Phone: 617.253.8594  
Fax: 617.452.2708  
briany@mit.edu

---

## EDUCATION

### **Massachusetts Institute of Technology Cambridge, MA**

Ph.D. in Physical Chemistry Sept. 2006  
(expected)  
"Microfluidic Reactors for the Synthesis of Semiconductor Nanocrystals"  
*Advisors:* Mounji Bawendi and Klavs Jensen  
NDSEG Fellow 2001-2004

### **University of North Carolina at Chapel Hill Chapel Hill, NC**

B.S. in Chemistry with Highest Distinction and Highest Honors May 1999  
*Advisor:* Royce Murray  
GPA: 3.93/4.00

## EXPERIENCE

### **Massachusetts Institute of Technology Department of Chemistry Cambridge, MA**

Research Assistant under Mounji Bawendi and Klavs Jensen Sept. 2001-present  
Designed, fabricated and applied silicon microreactors to the synthesis of colloidal semiconductor nanostructures. Developed reactor designs which enable enhanced control over mixing and heat and mass transfer, factors which are critical to the synthesis of high-quality nanocrystals.

### **Xanthon Inc.**

#### **Research Triangle Park, NC**

Electrochemical Instrumentation Division May 2000-July 2001  
Assisted in development of an electrochemical detection system for nucleic acids at a biotechnology company. Studied the mediated electrochemical oxidation of nucleic acid targets attached to tin-doped indium oxide electrodes.

### **Glaxo Wellcome Inc. (now GlaxoSmithKline)**

#### **Research Triangle Park, NC**

Analytical Sciences Department Oct. 1999-May 2000  
Identified and quantified pharmaceutical impurities using mass spectrometry for various development departments. Products included antidepressant and AIDS drugs.

### **University of North Carolina at Chapel Hill Department of Chemistry Chapel Hill, NC**

Undergraduate research under Royce Murray June 1997-May 1999  
Studied electrochemical and optical properties of alkanethiolate-protected gold nanoparticles.

### **MIT Center for Materials Science and Engineering / Materials Processing Center Cambridge, MA**

Summer research under Klavs Jensen Summer 1998  
Designed and fabricated liquid-phase microreactors from a variety of polymers using soft lithography.

### **University of North Carolina at Chapel Hill Department of Chemistry Chapel Hill, NC**

Teaching Assistant for introductory chemistry laboratory course Aug. 1997-May 1998

## AWARDS AND HONORS

MIT Presidential Graduate Fellowship (2001-2002)  
National Defense Science and Engineering Graduate Fellowship (2001-2004)  
Venable Medal, awarded to the two most outstanding seniors chemistry majors (UNC-CH, 1999)  
Undergraduate Award in Physical Chemistry (UNC-CH, 1999)  
Undergraduate Award in Analytical Chemistry (ACS, 1998)  
Barry M. Goldwater Scholarship (1998)  
Phi Beta Kappa (inducted 1997)

## REFEREED PUBLICATIONS

Steckel JS, **Yen BKH**, Oertel DC, Bawendi MG, "On the Mechanism of Lead Chalcogenide Nanocrystal Formation." *Journal of the American Chemical Society* **2006**, accepted for publication.

Chan YT, Snee PT, Caruge J-M, **Yen BKH**, Nair GP, Nocera DG, Bawendi MG, "A Solvent Stable Nanocrystal-Silica Composite Laser." *Journal of the American Chemical Society* **2006**, 128, 3146-3147.

**Yen BKH**, Günther A, Schmidt MA, Jensen KF, Bawendi MG, "A Microfabricated Gas-Liquid Segmented Flow Reactor for High-Temperature Synthesis: The Case of CdSe Quantum Dots." *Angewandte Chemie International Edition* **2005**, 44, 5447 (Issue Cover).

**Yen BKH**, Stott NE, Jensen KF, Bawendi MG, "A Continuous-Flow Microcapillary Reactor for the Preparation of a Size Series of CdSe Nanocrystals." *Advanced Materials* **2003**, 15, 1858.

Popovich ND, **Yen BKH**, Wong SS, "Effect of Tin-Doped Indium Oxide Electrode Preparation Methods on Mediated Electrochemical Detection of Nucleic Acids." *Langmuir* **2003**, 19, 1324.

Popovich ND, Wong SS, **Yen BKH**, Yeom HY, Paine DC, "Influence of Microstructure on the Electrochemical Performance of Tin-Doped Indium Oxide Film Electrodes." *Analytical Chemistry* **2002**, 74, 3127.

Hostetler MJ, Zhang CJ, **Yen BKH**, Andereg J, Gross SM, Evans ND, Porter M, Murray RW, "Stable, Monolayer-Protected Metal Alloy Clusters." *Journal of the American Chemical Society* **1998**, 120, 9396.

## PATENT APPLICATIONS

Stott NE, Jensen KF, Bawendi MG, **Yen BKH**, "Method of Preparing Nanocrystals", *US 2005/0112849*, filed August 2004.

**Yen, BKH**, Günther A, Jensen KF, Bawendi MG, Schmidt MA, "Flow Method and Reactor for Manufacturing Nanocrystals." filed September 2005.

## PRESENTATIONS

**Yen BKH**, Günther A, Schmidt MA, Jensen KF, Bawendi MG, "A Microfabricated Segmented Flow Reactor for Synthesis of Quantum Dots," *Materials Research Society Conference*, Fall 2005.

**Yen BKH**, Günther A, Schmidt MA, Jensen KF, Bawendi MG, "A Microfabricated Segmented-Flow Reactor for the Synthesis of CdSe Quantum Dots," *International Conference on Microreaction Technology (AIChE Meeting)*, Spring 2005.

**Yen BKH**, Stott NE, Jensen KF, Bawendi MG, "A Simple Capillary Reactor for the Synthesis of a Size Series of CdSe Quantum Dots," *Materials Research Society Conference*, Spring 2004.

**Yen BKH**, Popovich ND, Wong SS, Andersen KP, Napier ME, Eckhardt AE, "An Electrochemical Sensor for the Detection of Unmodified Nucleic Acids," *Electrochemical Society Conference*, Spring 2001.

## **POSTERS**

**Yen BKH**, Günther A, Thalmann M, Bawendi MG, Jensen KF, "A Microfabricated Segmented-Flow Reactor for the Synthesis of CdSe Quantum Dots." *μTAS*, Fall 2004.

**Yen BKH**, Günther A, Schmidt MA, Jensen KF, Bawendi MG, "A Microfabricated Gas-Liquid Segmented Flow Reactor for Quantum Dot Synthesis." *Gordon Research Conference*, Summer 2005.

## **PROFESSIONAL MEMBERSHIPS**

American Chemical Society

Materials Research Society



## Acknowledgements

*“When I grow up, I want to write like Warren Buffett.”*

– Robert C. Higgins<sup>1</sup>

I share Professor Higgins’ sentiment. Unfortunately, I am already grown up, and I still cannot write like Warren Buffett. I can only hope that the few souls who did peruse these pages are ultimately able to extract some marginal utility from them. Many students find that this section of the thesis is the most difficult part to write. I am no exception, probably because I realize that it is usually the only section that those aforementioned souls end up reading.

For the student, the conclusion of a PhD program is a period of reflection, introspection, and self-assessment. The words of the Oracle are particularly apt: “Over the years, a number of very smart people have learned the hard way that a long string of impressive numbers multiplied by a single zero always equals zero.”<sup>2</sup> Graduate research follows a related principle: a long string of zeroes multiplied by a single impressive number (result). However, I do not think that the overall PhD experience is always equal to zero, and I am truly grateful to the people who have helped me make it this far.

As a scientist, the importance of a good advisor cannot be overstated. I was fortunate to have two exceptional mentors early in my career. As an undergraduate at UNC, my advisor Royce Murray led by example and served as an inspiration for me. He not only provided encouragement and scientific vision, but he also expressed a genuine concern for the well-being of his students. I began working for my second mentor, Klavs Jensen, during a summer as an undergraduate. Since I didn’t destroy any important equipment, I was able to continue this relationship throughout my graduate studies here at MIT. Klavs always made me strive to meet a higher standard, while at the same time I never felt any undue pressure from him. Perhaps that is the one quality that defines a good advisor: getting students to want to work for themselves rather than for their boss. Like most professors, Klavs certainly provided the “big picture” insights for projects, but his advice was also grounded in the practical considerations of the experiment. That means a lot in research.

Of course, one of the people most instrumental in this thesis is Mounji Bawendi, my advisor in Chemistry. I can honestly say that, for me, he was the best choice for an advisor in Physical Chemistry at MIT. I am grateful for his patience and the autonomy that he gave me during my time in the group. The freedom to pursue whatever direction that I wanted was a valuable experience in terms of my development as an independent researcher.

I also thank my collaborator in the Jensen group, Axel Günther. The work in this thesis greatly benefited from Axel’s approach to the many design and engineering issues. Having a real engineer (rather than a chemist trying to be an engineer) involved in this project was invaluable. Such a long and fruitful collaboration is rare in academic research. I wish him the best; I’m sure he will go on to do great things.

I also must acknowledge the contribution of Professor Martin Schmidt to this thesis. Though we only met a few times, his advice during the early planning stage of each new device design undoubtedly saved me months of potential redesign and fabrication. In terms of productivity – i.e. return per unit of invested meeting time – Marty may be ranked number one out of all of the professors involved in this thesis.

Many thanks to members of the Bawendi and Jensen groups for creating a genuinely positive and supportive work environment. They are too numerous to mention individually, but I must highlight the four students who joined the Bawendi group with me. This band of brothers made my time in the basement tolerable. Yinthai, I will miss your humor and self-deprecating personality. John Zimmer, I thank you for helping me maintain my perspective and for keeping it real. Dave Oertel, you sir are a gentleman of high principles. I have tried to do a yeoman's job with this thesis, and I hope I do not disappoint you. Jonny Steckel, your unassailable optimism kept all of us going through the darkest hours.

Off the court, there are several people who deserve special mention. I thank Joe Loparo for his true friendship and unfailing support over the past five plus years. We went through this together every step of the way and for that I am grateful. Congratulations to Joe and Erin as they write a new chapter of their lives together. I must recognize Hao Zhu who, unlike me, is a real doctor. I've known Hao since high school, and by circumstance, we both ended up in Cambridge at the same time. I was very lucky to have this friendship and human interaction outside of MIT. In addition, the Yen and Pribisko families were constant sources of strength and support for me. Their encouragement and understanding sustained me throughout my time at MIT.

Finally, I would not have been able to endure this long trial without the love and support of my special lady and life partner, Melanie. She faced the pain of our separation with unconditional patience and understanding. Being apart over these five plus years may not qualify as an odyssey, but I think the words of a modern-day Odysseus are still appropriate: She's the best thing to ever happen to a bum like me.<sup>3</sup> It's true.

Brian Yen  
September 18, 2006  
Cambridge, MA

---

<sup>1</sup> R. C. Higgins, *Analysis for Financial Management*, 7th ed., McGraw-Hill: New York, 2004.

<sup>2</sup> W. E. Buffett, *Berkshire Hathaway, Inc. 2005 Annual Report*. Available at [www.berkshirehathaway.com](http://www.berkshirehathaway.com).

<sup>3</sup> John McClane in *Die Hard*, Dir. J. McTiernan, 20<sup>th</sup> Century Fox, 1988.